Unipolar Diffusion Charging of Spherical and Agglomerated Nanoparticles and its Application toward Surface-area Measurement

A Dissertation
SUBMITTED TO THE FACULTY OF
UNIVERSITY OF MINNESOTA
BY

Nanying Cao

IN PARTIAL FULFILLMENT OF THE REQUIREMENTS
FOR THE DEGREE OF
DOCTOR OF PHILOSOPHY

Dr. David Y.H. Pui

December 2017

Acknowledgements

I would like to express my sincere gratitude to my advisor Prof. David Y.H. Pui for his continuous guidance, mentoring, and inspiration throughout my graduate study. I heartily thank my committee members: Prof. David B. Kittelson, Prof. Thomas H. Kuehn and Prof Filippo Coletti for reviewing my dissertation and offering valuable comments and suggestions.

I am also grateful to my international collaborators: Prof. Heinz Fissan and Christof Asbach at the Institute of Environmental and Energy (IUTA e.V.) in Germany; Prof. Sotiris E. Pratsinis and Jing Wang at ETH Zürich in Switzerland; Dr. Max L. Eggersdorfer in Harvard University.

My sincere thanks also go to my current and former colleagues in the Particle Technology Laboratory: Prof. Shawn Chen, Dr. Qisheng Ou, Dr. Tsz Yan Ling, Dr. Zhili Zuo, Dr. Shigeru Kimoto, Dr. Lin Li, Dr. Seong Chan Kim, Dr. Young H. Chung, Drew Thompson, Qingfeng Cao, Handol Lee, Seungkoo Kang, Chenxing Pei, Luying Liu, Dongbin Kwak, Kai Xiao, Gustaf Lindquist, Swathi Satish, Dr. Mamoru Yamada and Dr. Ningning Zhang. Their company, discussion, and assistance were invaluable.

This work was supported by National Science Foundation (NSF) Grant #1236107, "GOALI: Unipolar Diffusion Charging of Spherical and Agglomerated Nanoparticles and its Application toward Surface-area Measurement". I also thank the support of members of the Center for Filtration Research: 3M Corporation, A.O. Smith Company, Applied Materials, Inc., BASF Corporation, Boeing Company, Corning Co., China Yancheng

Environmental Protection Science and Technology City, Cummins Filtration Inc., Donaldson Company, Inc., Entegris, Inc., Ford Motor Company, Guangxi Wat Yuan Filtration System Co., Ltd., MSP Corporation; Samsung Electronics Co., Ltd., Xinxiang Shengda Filtration Technology Co., Ltd., TSI Inc., W. L. Gore & Associates, Inc., Shigematsu Works Co., Ltd., and the affiliate member National Institute for Occupational Safety and Health (NIOSH).

Finally, I am indebted to my parents and family (wife and son) for their constant love, trust, and support.

The fire melting my ice

The light brightening my corner

To you, my dear wife,

Ella

Abstract

This thesis consists of two parts: unipolar diffusion charging of nanoparticles and its application on the method development of surface-area measurements.

The electrical capacitance of aerosol particles indicates their potential diffusion charging level, which is important for their classification by electrical mobility, precipitation (removal or collection) in electrical fields, and morphology characterization. A minimum potential energy method was used to calculate the electrical capacitance for agglomerates composed of equally sized spherical primary particles (PPs). By discretizing the particle surface using finite spherical elements, as net charge only resides on the surface of an isolated conductor, this method was extended to calculate the capacitance of arbitrarily shaped particles. Based on the capacitance, the charge of these particles was obtained by diffusion charging theory. In addition, the dynamics of capacitance and mean charge of agglomerate during sintering or coalescence (at constant particle volume) to aggregates and finally to compact structures was computed and found in agreement with sparse experimental data. Particle morphology strongly affects the capacitance and mean charge of fractal-like particles. For example, both decreased by 60% upon full coalescence or sintering of an agglomerate consisting initially of 128 PPs.

Although geometric surface area (GSA) of nanoparticles has received much attention in many fields (drug delivery, catalysts, inhalation exposure, toxicity, etc.), no appropriate instruments and methods for online measurements of GSA are readily available. Therefore, this study intends to develop a Geometric Surface Area Monitor

(GSAM) to measure the GSA of spherical as well as model agglomerate/aggregate nanoparticles in nearly real-time. The GSAM has two versions: 1. The GSAM (I) consists of several existing techniques in series, including inertial impaction, unipolar charging, electrostatic precipitation, and electrical current measurement. The GSAM (I) was first evaluated and calibrated by measuring the GSA of monodisperse nanoparticles. Spherical, aggregate, and agglomerate nanoparticles were tested in the calibration. It was found that the measured electrical current was proportional to the surface area concentration. The calibration curves obtained from the measurements of monodisperse particles was then applied for polydisperse spherical particles and compared the measured GSA with that determined by the well-known scanning mobility particle sizer (SMPS) where the GSAM (I) had less than 10% of deviation compared with SMPS. 2. In the GSAM (II), the commercialized nanoparticle surface area monitor was used and slightly modified. The instrument responses under two different conditions were combined in a weighted sum (WS) fashion to correlate with the aerosol GSA concentration. We present the GSA concentration results and comparisons with well-known SMPS data in both laboratory testing and field measurement. For the laboratory testing, the two methods have a good agreement with a Pearson correlation coefficient of 0.9961; for the field measurements including the indoor and outdoor samplings, both methods agree well with each other. In addition, the new WS method is more stable in the clean indoor air and suitable for outdoor environmental sampling with a slight overestimation (125% of SMPS).

These three studies below comprise parts of the main body of this dissertation and have been published.

Chapter 2: Cao, L. N. Y., Wang, J., Fissan, H., Pratsinis, S. E., Eggersdorfer, M. L., & Pui, D. Y. H. (2015). The capacitance and charge of agglomerated nanoparticles during sintering. *Journal of Aerosol Science*, 83(0), 1-11. doi: http://dx.doi.org/10.1016/j.jaerosci.2015.01.002

Chapter 3: Cao, L. N. Y., Chen, S.-C., Fissan, H., Asbach, C., & Pui, D. Y. H. (2017). Development of a geometric surface area monitor (GSAM) for aerosol nanoparticles. *Journal of Aerosol Science*, 114, 118-129. doi: https://doi.org/10.1016/j.jaerosci.2017.09.013

Chapter 4: Cao, L. N. Y., & Pui, D. Y. H. (2018). A novel weighted sum method to measure particle geometric surface area in real-time. *Journal of Aerosol Science*, 117, 11-23. doi:https://doi.org/10.1016/j.jaerosci.2017.12.007

Table of Contents

List of Tables

List of Figures

Chapter 1: Introduction

1.1 Background

1.1.1 Unipolar diffusion charging of arbitrarily shaped particles

Electrical diffusion charging of aerosol particles plays an important role in the research of gas borne particles including aerosol instrumentation (White, 1951; Pui et al., 1988), materials production from aerosols (Vemury & Pratsinis, 1995; Hogan & Biswas, 2008), air pollution control (Gentry, 1972), determination of the size distribution of fine particles by measuring their electrical mobility (Kirsch and Zagni'tko, 1981; Reischl et al., 1996), and atmospheric aerosol physics (Fuchs, 1963). In the diffusion charging process, either bipolar or unipolar ion environments were provided to charge the particles in order to accomplish various charging tasks. Unipolar diffusion charging has become more attractive than bipolar diffusion charging as unipolar diffusion charging does not reach an equilibrium charge distribution, thereby offers higher charging efficiency.

Most diffusion charging theories (White 1951; Fuchs, 1963; Liu & Pui, 1977) that have been widely and successfully used assume spherical particles. However, in addition to spherical particles, agglomerates and aggregates are also ubiquitous in atmospheric aerosol physics, air pollution control, and material production. In fact, chain aggregates occupy a large portion of the ultrafine atmospheric aerosol in urban and industrial areas. Furthermore, several previous studies (Rogak and Flagan, 1992; Chang, 1981) showed the effect of particle morphology on unipolar diffusion charging processes in both

theoretical and experimental ways (Oh et al. 2004; Shin et al. 2010; Wang et al. 2010). Thus, the unipolar charging properties of particles in arbitrary shapes deserve a more sophisticated study.

1.1.2 Particle surface-area measurement

The surface area of particles is of great interest in many fields, such as exposure to and toxicity of airborne particles, drug delivery, and catalysts manufacturing and application. For instance, Oberdörster (2000) found the adverse health effects caused by the particles correlated highly with the total particle geometric surface area (GSA). Surface area also plays an important role in the field of drug delivery. Redhead et al. (2001) tested the drug delivery of nanodrugs (150 nm particles loaded with Rose Bengal) and suggested that the low drag loading and an initial burst of drug release were all attributed to the high surface area of particles compared to the volume. It is therefore strongly desirable to measure particle surface area, for example, during a manufacturing process to monitor the exposure or product quality, or during toxicological tests to accurately predict the dose in the form of surface area for different systems.

Several approaches are available to directly measure the surface area of particles. The Brunauer–Emmett–Teller (BET) (Brunauer, Emmett, & Teller, 1938) method estimates the capability of a pile of powders (not airborne particles) to adsorb gas molecules (e.g., nitrogen) and is considered as a reference method. However, its detection limit of the surface area is as high as 0.02 m^2 (Lebouf et al., 2011), which corresponds to

6.37E+11 nonporous spherical nanoparticles in 100 nm. In other words, the method requires at least a continuous sampling for 71 h of the 100 nm particles with the concentration of 1E+5 particles/cm^3 (a high but still reasonable indoor or outdoor concentration) at the flow rate of 1.5 lpm. Another offline technique is transmission or scanning electron microscopy that can estimate surface area from two-dimensional projections of particle images. However, it is a very laborious and time-consuming method and hence typically only a limited number of particle images can be analyzed. Consequently, it may not be valid to calculate the total surface area from small amounts of image samples.

The main issue of the above methods is that they are offline and time consuming. A real-time and ideally mobile measurement is more desirable for aerosol particles since giving temporal and spatial distributions are important and of great interest (e.g., for mobile emissions from travelling vehicles). Right now, a quasi-real-time surface area measurement is available by the scanning mobility particle sizer (SMPS) by converting the particle mobility diameter to equivalent surface area assuming spherical particles with a time resolution of typically between 50 and 300 seconds. However, strict regulations apply to the use of the radioactive Po-210 and Kr-85 that are required to neutralize the aerosol.

A widely-applied approach that combines diffusion charging with subsequent measurement of the particle induced electrical current can quickly approximate particle surface area. This method can obtain results with a time resolution of one second (or even below) and with low detection limit, e.g., 200 particles/cm^3 for monodisperse 50 nm

particles for Electrical Aerosol Detector (EAD, model 3070A, TSI Inc, Shoreview, MN, TSI data sheet, 2004). However, the instrument response is not proportional to the geometric surface area (GSA) concentration, but a metric also known as Fuchs or active surface area that is kinetically limited. In the free molecular and continuum regime, the active surface area is theoretically proportional to a certain power of the particle diameter, i.e. $d^{2.0}$ and $d^{1.0}$, respectively (Pandis et al., 1991). In between the two regimes (i.e., transition regime including most nanoparticles) the active surface area is still a power law of d with the power varying between 1.0 and 2.0. Instruments based on this principle include LQ1-DC (Matter Aerosol, Wohlen, Switzerland), Nanoparticle Surface Area Monitor (NSAM, model 3550, TSI Inc, Shoreview, MN, Fissan et al., 007, Shin et al., 2007), DiSCmini (Testo AG, Lenzkirch, Germany, Fierz et al., 2011), Partector (Naneos Particle Solutions, Windisch, Switzerland, Fierz et al., 2013), NanoTracer (Oxility BV, Best, Netherlands, Marra et al., 2010) and PPS-M Particle Sensor (Pegasor Oy, Tampere, Finland, Järvinen et al., 2015)

Until now, no appropriate methods are available to measure the GSA of particles. The GSA is stated previously to correlate well with particle adverse health effect and drug loading. In addition, Schmid & Stoeger (2016) stated that, for non-porous nearly spherical particles, the GSA can be used as "biologically most relevant dose metric" for nanoparticle pulmonary toxicity. After all, the GSA is the very original surface area that involves minimum assumptions. Thus, it can derive other surface areas easily with assumptions according to the situations, e.g., active surface area when considering the ion

attachment ability or lung deposited surface area (LDSA) when considering the particle deposition in the lung of a reference worker.

1.2 Research objective

The objectives of this study were to 1) develop a method to model the self-capacitance and mean charge of arbitrarily shaped particles and 2) develop a novel method to measure the aerosol geometric surface area in real-time.

Particle self-capacitance indicates the ability of a body to store electrical charges. For the self-capacitance modelling, we extended the approach of Brown & Hemingway (1995) from loose agglomerate to arbitrarily shaped particles. For the particle morphology modelling, agglomerates undergoing viscous flow sintering through multiparticle coalescence were simulated and evolution of aggregate capacitance was calculated. Finally, we simulate the evolution of aggregate charge during the sintering, using Chang's (1981) theory for particle charge based on capacitance.

The geometric surface area monitor for aerosol should be cost-effective real-time. A geometric surface area monitor (GSAM version I) was developed and composed of several existing techniques in series, including inertial impaction, unipolar charging, electrostatic precipitation, and electrical current measurement. In the GSAM (version II), the commercialized nanoparticle surface area monitor was used and slightly modified. The instrument responses under two different conditions were combined in a weighted sum (WS) fashion to correlate with the aerosol GSA concentration. The second version had a wider measuring range and easier setup and eliminate the pressure issue in the first version in addition.

1.3 Dissertation outline

This dissertation is organized in the following manner. A brief review of the topic of this dissertation is presented in this chapter. The next three chapters comprise the main body of the dissertation, each based on a separate manuscript that has been published. Chapter 2 describes the novel method to simulate the capacitance and charge of agglomerated nanoparticles during sintering. Chapter 3 discusses the development of a geometric surface area monitor (GSAM version I) for aerosol nanoparticles by combining the inertial impaction, unipolar charging, electrostatic precipitation, and electrical current measurement. Its application is demonstrated by measuring the geometric surface area (GSA) concentration of polydisperse aerosols and comparing data with the standard method. Chapter 4 describes the novel weighted sum method to measure particle geometric surface area in real time (GSAM version II). Its application is demonstrated by measuring the GSA concentration of the aerosols in both indoor and outdoor environments. Finally, the conclusion and future works are given in Chapter 5.

Chapter 2: The capacitance and charge of agglomerated nanoparticles during sintering

2.1 Introduction

Particle capacitance indicates the ability of a body to store electrical charges. More specifically for aerosol charging, we are interested in self-capacitance of a particle, which is the electrical charge that must be added to an isolated particle to raise its potential by one unit (Greason, 1992), as opposed to the mutual capacitance between two adjacent conductors, such as a capacitor composed of two plates. Chang (1981) proposed expressions for the mean charge of arbitrarily shaped particles as a function of their self-capacitance in unipolar diffusion charging processes. His results were developed based on the work of Laframboise and Chang (1977), who extended the continuum regime diffusion equation to particles of arbitrary shapes. Rogak and Flagan (1992) and Filippov (1994) pointed out that the electric capacitance is affected by particle morphology using an analogy between electrostatics and diffusion.

In addition, the particle capacitance can be used to calculate diffusion charging of particles. Chang (1981) showed, for a given charger, the mean charge per particle is proportional to the particle capacitance in the continuum regime of charging. Shin et al. (2010) showed by simulations that the capacitance of chain-like agglomerates (physically-bonded PPs) is larger than that of spheres with the same mobility diameter

and the difference increased with increasing PP number per agglomerate. This is in agreement with his experiments showing that the mean charge per particle of silver agglomerates was about 24% larger than that for fully coalesced silver spheres with the same mobility diameter in the mobility size range of 30-200 *nm* when the measurement error for both agglomerates and spheres was within 2%. In addition, Oh et al. (2004) used an indirect photoelectric charger and showed that TiO_2 agglomerates in the mobility size range of 50 *nm* to 200 *nm* with a low mass fractal dimension, D_{fm}, had about 30% more charges than spherical particles. Jung and Kittelson (2005) showed that diesel agglomerates acquired more charges than nearly spherical NaCl particles by 15 - 17%. Wang et al. (2010) observed that the number of charges acquired by compact aggregates (chemically- or sinter-bonded PPs) was in-between those of agglomerates and spheres.

Nonetheless, it is difficult to directly measure the capacitance of airborne particles. Therefore, data for capacitance of aerosols are mainly obtained from analytical solutions (Serway & Jewett, 2009) or numerical studies (Zhou et al., 1994). Brown & Hemingway (1995) used a variational method to calculate the charge distribution for the minimum electrostatic energy, thus obtaining the capacitance. Their method is applicable to agglomerates of spherical PPs in point contact with arbitrary agglomerate geometry and PP size. However, this method is limited to conducting particles with the entire agglomerate being at the same electrical potential. Nevertheless, Brown & Hemingway (1995) also pointed out that it is not necessary for the particle to be a good conductor, only that the charge relaxation time should be shorter than the typical time of observation

or life time of aerosols. They argued that this assumption is reasonable for many aerosols, except for those with extremely high resistivity over $10^{11}\ \Omega \cdot m$, as for example insulating polymer particles. Brown & Hemingway's (1995) method has been used to calculate the capacitance of particles in various configurations, including single sphere, doublet, triplet, straight and branched chain (Shin et al., 2010). However, only few 3D numerical simulations have been done for the spatial charge distribution and capacitance of agglomerates with many PPs. Also, little is known about the capacitance of necked aggregates that are often formed at high temperatures by sintering during gas-phase synthesis of materials (Pratsinis, 1998).

Here, 3D agglomerates with up to 512 PPs are investigated. The evolution of capacitance and mean charge for such agglomerates undergoing sintering or coalescence is simulated by generalizing the method of Brown & Hemingway (1995), covering particle morphologies from fractal-like agglomerates to aggregates and finally to compact spheres. The method was modified to relax the restriction on spherical PPs and calculate particles of arbitrary shapes. Unlike agglomerates with spherical PPs in point contact, in aggregates PPs are not well defined. Here a given particle with arbitrary shape was discretized into fine spherical elements to facilitate the calculation of the minimum electrostatic energy. The assumption that the particle is a reasonable conductor is still needed, and any net charge on an isolated conductor resides on its surface according to Gauss' theorem (Serway & Jewett, 2009). This means that discretization is only needed on the particle surface. Under those assumptions, the method could be applied to any type

of particles. Validation was carried out by comparison with analytical (Serway & Jewett, 2009) and numerical solutions and experiments (Brown & Hemingway, 1995). By applying the method to agglomerates undergoing viscous flow sintering through multiparticle coalescence simulations (Eggersdorfer et al., 2011), we are able to calculate the evolution of aggregate capacitance. So, by applying Chang's (1981) theory for particle charge based on capacitance, we simulate the evolution of aggregate charge during sintering.

2.2 Methodology

2.2.1 Agglomerate and Aggregate Generation

In this study, the capacitance of diffusion-limited cluster-cluster agglomerates (DLCAs) consisting of monodisperse spherical PPs during sintering is investigated. These simulations are validated with experiments of agglomerates produced at room temperature (Shin et al., 2010). Here such DLCAs are generated numerically from initially monodisperse PPs by a hierarchical cluster-cluster algorithm (Botet et al., 1984). The agglomerate generation starts with 2^n individual PPs. Two PPs are randomly chosen from the ensemble and undergo a random walk until they collide and stick to form a dimer. The process is repeated with all pairs until 2^{n-1} dimers are assembled. Then the dimers are combined to 2^{n-2} clusters of four particles and so on until only one single agglomerate consisting of 2^n PPs is obtained. For each PP number (4, 8, 16, 32, 64, 128,

256, and 512), 50 DLCAs are generated. The mobility diameter for DLCA is determined by the rotationally projected area in momentum transfer free molecular regime (Sorensen, 2011).

Clusters or agglomerates restructure by sintering (Akhtar et al., 1994) from the initial agglomerate with a relatively open structure (e.g. DLCA) to a compact aggregate with necked PPs, and finally to a single spherical particle. During sintering or coalescence, the fractal dimension of the aggregate increases gradually from 1.79 (DLCA) to 3.0 (sphere) (Eggersdorfer et al., 2011). Here the change in capacitance and average particle charge during viscous flow sintering of fractal-like particles is investigated exemplarily with an agglomerate of 128 PPs by multi-particle sintering simulations that quantitatively describe the morphology evolution from ramified agglomerates to aggregates and compact particles (Eggersdorfer et al., 2011).

2.2.2 Minimization of Electrostatic Energy

The particle shape with the minimum surface to volume ratio and minimal surface energy is a sphere. The capacitance, C_p, of a sphere is (Serway & Jewett, 2009):

$$C_p = 4\pi\varepsilon_0 a\,, \tag{1}$$

where ε_0 is the permittivity of vacuum and a is the sphere radius. However when the number of spheres (PPs) increases in an agglomerate, the capacitance calculation is more complicated. There is no simple expression even for three spheres in a straight line, not to

mention real-world agglomerates for which the number of PPs could be dozens to thousands (Wentzel et al., 2003; Shin et al., 2009a) and the resulting structure quite complex. Brown & Hemingway (1995) calculated the capacitance of agglomerates and the spatial charge distribution accounting for agglomerate structure based on two assumptions: (1) spherical PPs are well defined and (2) they are at least slightly conductive. The first assumption is fulfilled for most agglomerates; however, it is the major limitation of their method for its application to randomly shaped structures like aggregates. Five equations determine the capacitance:

$$\sum_{i=1}^{N} Q_i = Q\,, \tag{2}$$

$$\Phi_s = \sum_{i=1}^{N} \frac{Q_i^2}{8\pi\varepsilon_0 a_i}\,, \tag{3}$$

$$\Phi_i = \frac{1}{2}\sum_{i=1}^{N}\sum_{\substack{j=1 \\ i\neq j}}^{N} \frac{Q_i Q_j}{4\pi\varepsilon_0 \left| r_i - r_j \right|}\,, \tag{4}$$

$$\frac{\partial}{\partial Q_i}\left[\Phi_i + \Phi_s + k\left(\sum_{i=1}^{N} Q_i - Q\right)\right] = 0 \quad for \quad all \quad i\,, \tag{5}$$

$$C_p = \frac{Q^2}{2\left(\Phi_i + \Phi_s\right)}\,, \tag{6}$$

where Q_i is the charge on the *ith* PP, Q is the total charge on the cluster, Φ_s is the self-energy of the PPs, a_i is the radius for the *ith* PP, Φ_i is the pairwise interaction electrostatic

energy between every two PPs, r_i is the location of the *ith* PP, and k is the Lagrangian multiplier (please see Appendix A.1 for the numerical techniques of solving the above equations).

Here, Eq. 5 is solved to minimize the total electrostatic energy ($\Phi_i+\Phi_s$) by optimizing the distributions of electrical charges on each PP. Charges are balanced in Eq. 2. With the results of spatial charge distribution on every single PP in Eq. 5, energy terms can be obtained by solving Eqs. 3 and 4. Finally, the capacitance is calculated by its definition in Eq. 6. The capacitance of the particle can be calculated with arbitrary non-zero values of Q, even though Q may not necessarily correspond to an actual charge value. This is because capacitance is an intrinsic property of the particle, which can be validated in Eqs. 2-6.

The capacitance of agglomerates even with huge amounts of PPs can be successfully modeled with the radius and coordinates of each PP. Correlations of capacitance for 2D agglomerates (PPs are in the same plane) such as straight chain and cross-like ones were developed by Shin et al. (2010). The relationship between the normalized agglomerate capacitance, C_p^*, by that of a single PP, and N could be fitted into power laws for $12<N\leq300$:

$$C_p^* = 0.58N^{0.77} \text{ for a chain agglomerate,} \quad (7)$$

$$C_p^* = 0.47N^{0.79} \text{ for a branched chain agglomerate with aspect ratio } \beta=1.6, \quad (8)$$

where β equals the length over the width of the particle.

However, this method is not applicable to particles without well-defined spherical PPs, such as compact aggregates.

2.2.3 Discretization

Since there are no distinct spherical PPs in an aggregate, the method of Brown & Hemingway (1995) is modified by discretizing the aggregate with fine spherical elements. Based on the fact that the net charge only resides on the surface of an isolated conductor, particles are represented by finite elements only on their surfaces in the discretization step. Their actual geometries are discretized and represented by a hollow cluster consisting of thousands of identical spheres (elements) point-contacted to each other on the surface (please see Appendix A.2 for discretization using modified spherical coordinates).

Figs. 2-1a and 2-1b show examples of discretization for a spherical particle and a straight chain agglomerate with 11 PPs, respectively. The refinement was varied from 44 to 30,904 uniform surface elements to estimate the error of discretization. The smaller elements are used, the more elements are needed.

After discretization, Eqs. 2-6 are used to calculate the capacitance. Gaps always exist between spheres when we try to construct a smooth body out of spherical elements without overlapping. However, as long as a sufficient number of elements are used, the effect of the gaps is negligible. The discretization method is validated by comparison with previous experimental results. The simulation errors from the discretization for both

a spherical particle in Fig. 2-1a and a straight chain agglomerate in Fig. 2-1b are compared with experimental data (Brown & Hemingway, 1995) in Fig. 2-2. The relative error is defined as the relative difference between the calculated results, S, and experimental data, E: $Error = \frac{S-E}{E}$.

In Fig. 2-2, the error is significant when the reconstruction of geometry is too coarse compared with the actual one, namely, when the number of used spherical elements, n, is too small, e.g. $n<44$ for the sphere case. Meanwhile, the simulation is limited by computer resources. As a result, the acceptable n we used for discretization of a spherical particle and straight chain agglomerate with 11 PPs were between 318-30,904 and 1,948-29,382, respectively. The lower limit was intended to provide satisfactory discretization and the upper limit was affected by the time and capacity of computing. This algorithm converged faster as the fineness of discretization increases and the errors were stable at around 0.3% and 2% for the sphere and chain agglomerate, respectively. Thus, as long as sufficient spherical elements are used, the discretizations for both the sphere and straight chain particles are valid and give satisfactory results for the capacitance.

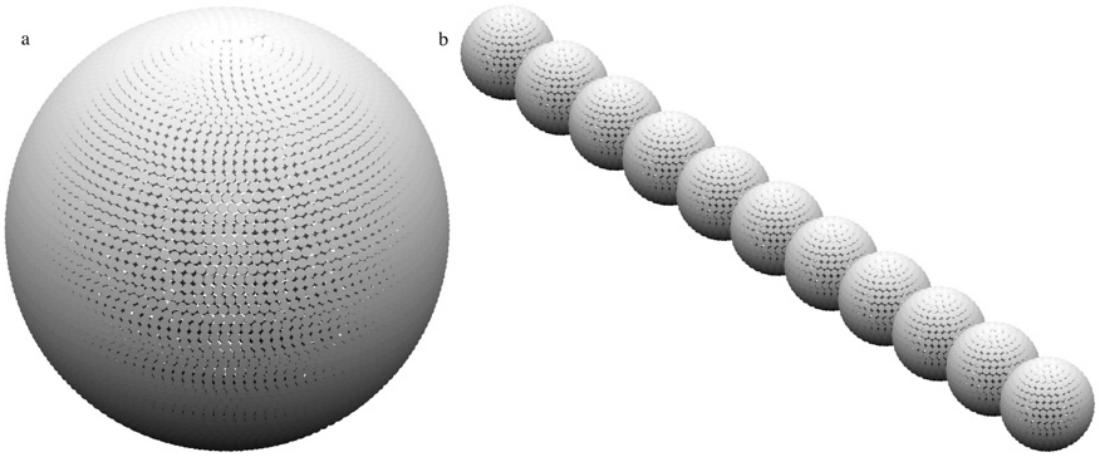

Fig. 2-1. Discretization of (a) spherical particle with 5,516 elements**,** and (b) straight chain agglomerate with 11 PPs with total 5,512 elements.

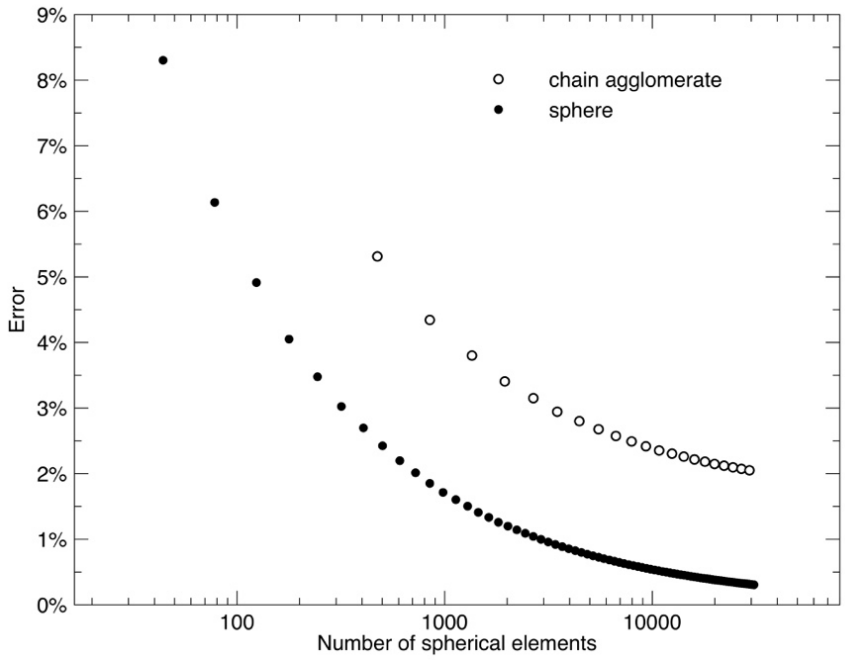

Fig. 2-2. The discretization error as a function of number of spherical elements for the capacitance of a straight chain agglomerate with 11 PPs (open symbols) and a sphere (filled symbols).

2.2.4 Theory of diffusion charging for arbitrarily shaped particles

To calculate the particle charge from its capacitance in diffusion charging, Chang (1981) developed a theory to obtain the mean charge per particle for arbitrarily shaped clusters by diffusion charging for continuum (Kn_{ion}<<1) or free molecule (Kn_{ion}>>1) regimes, where Kn_{ion} is the ionic Knudsen number (=λ_i/R_p), λ_i is the mean free path of the ion, and R_p is the particle radius. The theory is expressed

in continuum regime of charging by,

$$\sum_{m=1}^{\infty}\left\{\frac{\varphi_p^m}{m\cdot m!}\right\}=\frac{e^2N_iDt}{kT\varepsilon_0}, \tag{9}$$

$$\varphi_p=\frac{e^2N_p}{C_pkT}, \tag{10}$$

or

$$\begin{aligned} N_p &\cong \frac{C_pN_iDt}{\varepsilon_0} \quad (\varphi_p<0.1) \\ &\cong \frac{2C_pkT}{e^2}\left[\left(\frac{e^2N_iDt}{kT\varepsilon_0}+1\right)^{0.5}-1\right] \quad (\varphi_p<1), \end{aligned} \tag{11}$$

and in free molecular regime of charging by,

$$N_p=\frac{C_pkT}{e^2}\ln\left(1+\frac{e^2N_i\bar{v}S_pt}{4kTC_p}\right), \tag{12}$$

where N_p is the mean charge per particle, N_i is the ion concentration in charger, t is charging time, D is the ion diffusion coefficient, k is the Boltzmann's constant, ϕ_p is the nondimensional surface potential, $\bar{v}$ is the average ion thermal velocity, and S_p is the geometric surface area of particles.

To compare with Shin's (2010) unipolar diffusion charging data, we use their parameters: $Nt=2.5\times10^{7}$ s/cm^3; 1.15 $cm^2/V\ s$ for the ion mobility; 290 *amu* for the ion mass. Here, the calculated ϕ_p is 5.4 by solving Eq. 9, therefore Eq. 10 is used for continuum regime of charging.

2.3 Results and Discussion

2.3.1 The spatial charge distribution & capacitance of agglomerates

Figs. 2-3a and 2-3b show the spatial charge distribution for a dimensionless 3D random fractal-like agglomerate with D_f= 1.79 and 128 monodisperse PPs and a compact agglomerate due to ballistic particle cluster agglomeration (Witten & Sander, 1981) with D_f= 2.8 and 128 monodisperse PPs, respectively. Highly charged PPs are located mainly in the periphery of agglomerate branches while PPs in the interior are barely charged, in order to spread out the charges and minimize the interaction energy (Eq. 5). Such a spatial charge distribution could be responsible for the formation of huge but short-lived agglomerates during flame synthesis of TiO_2 in the presence of external electric fields (Fig. 4 in Kammler et al., 2003). Such agglomerates lose their charge upon collection (e.g.

filtration) forming however unique particle deposition patterns (Vemury & Pratsinis, 1995) especially on metallic substrates (e.g. particulate films by direct flame deposition).

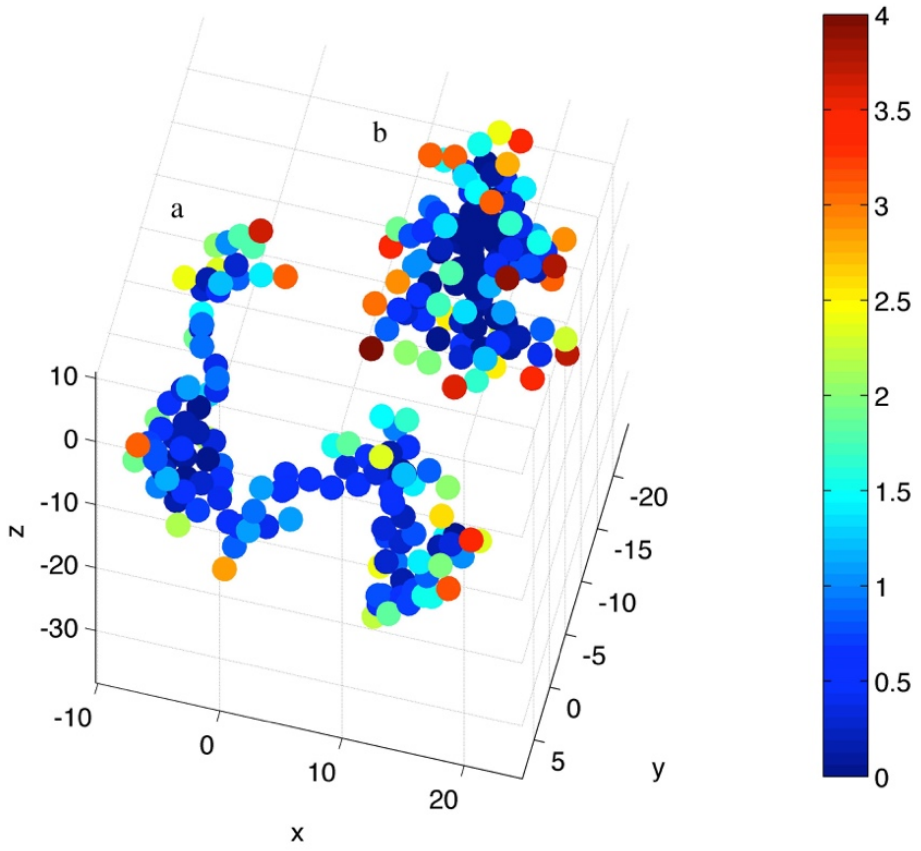

Fig. 2-3. The spatial charge distribution on (a) a fractal-like and (b) a compact agglomerate. The color scale indicates the ratio of the simulated charge to the average charge per PP, i.e. $Q_i/(Q/N)$. The axes are normalized by the radius of a PP.

In this study, totally 400 DLCAs were simulated. Unlike a straight chain, each DLCA has a unique geometrical configuration of PPs and therefore an average over 50 clusters is used here for each PP number. For agglomerates of 128 PPs, the mean

simulated normalized capacitance is 10.89 with a standard deviation of 0.69. The relationship between normalized capacitance (C_p^*) and number of PPs (N) for DLCAs is fitted into a power law for $4 \leq N \leq 512$:

$$C_p^* = 0.86 N^{0.52}. \tag{13}$$

In addition, compact agglomerates composed of PPs are also simulated (Fig. 2-3b) and the relationship could be also fitted into a power law for the range of $16 \leq N \leq 512$:

$$C_p^* = 1.13 N^{0.41}. \tag{14}$$

The model agrees well with the simulations of Thajudeen et al. (2012) and Gopalakrishnan et al. (2013) as shown in Fig. 2-4. The results of these 3D agglomerates can be compared with those of 2D clusters in Eqs. 7 and 8. Figure 4 shows the comparison of normalized capacitance as a function of PP number among chain agglomerates, branched chain agglomerates, DLCAs, and compact agglomerates. It is apparent that the capacitance is larger when the particle structure is more open. On open-structured particles charges can spread out more thus such structures have a lower electrical potential energy than compact ones. With consideration of the relation between capacitance and particle charge (Chang, 1981), the results here are also in general agreement with Oh et al. (2004), Shin et al. (2010) and Wang et al. (2010) who showed that open-structured agglomerates can obtain more charges than spherical particles.

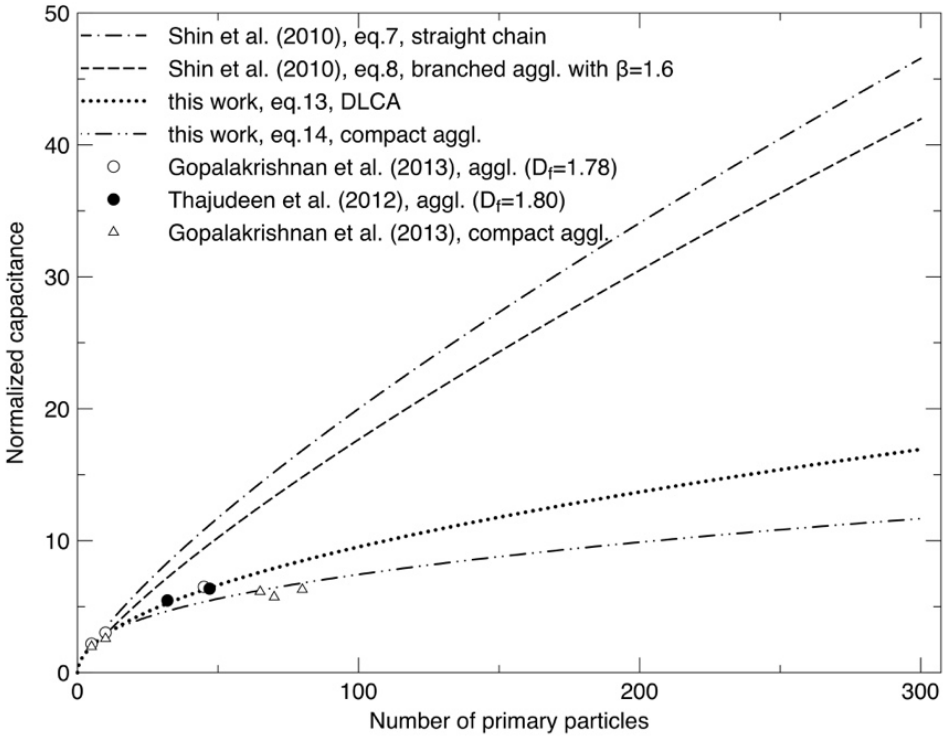

Fig. 2-4. Normalized capacitance as a function of the number of constituent PPs for chain (dot-broken line), branched chain agglomerate (broken line), DLCA (dotted line and circles), and compact agglomerate shown in Fig. 2-3b (double dot broken line and triangles).

2.3.2 Mean charge per particle as a function of the mobility diameter

With the capacitance we obtained, the mean charge per agglomerate and aggregate can be obtained by Chang's (1981) theory. By solving Eq. 9 and substituting the result and Eq. 1 into Eq. 10, we obtain:

$$N_p = \frac{\varphi_p kT}{e^2} C_p = \frac{\varphi_p kT}{e^2} 2\pi\varepsilon_0 d_p C_p^*, \quad (15)$$

where $\phi_p=5.4$ for the charger with $N_it=2.5\times10^{7}$ s/cm^3. In Fig. 2-5, the mean charge per particle is plotted as a function of mobility diameter and comparisons between experiments and models are also presented. Open and filled symbols represent the data by Shin et al. (2010) for agglomerates with a fractal dimension below 2.0 (PP d_p=19.5±6.1 *nm*) and fully sintered spheres, respectively; dotted and double-dot broken lines show the simulations for DLCAs (consisting of PP with d_p=19.5 *nm*) and equivalent spheres in the continuum regime of charging, respectively. The mobility regime is based on the air mean free path, whereas the charging regime is based on the ion mean free path. The calculated range is not entirely in the free molecular regime for mobility (section 2.1), and not entirely in the continuum regime for charging, but we use them as reasonable approximations and, for both spherical particles and DLCAs, the model (Chang, 1981) agrees well with the experiments by Shin et al. (2010). It is noted that both charging efficiency of the unipolar charger and transmission efficiency of the ion trap (removing excess ions out of the charger) decrease with decreasing particle size (Forsyth et al., 1998; Li et al., 2009; Shin et al., 2009b) and are not considered in the model. Since they both reduce particle charge, especially for particles below 100 *nm*, the experimental data are slightly lower than the model. To the best of the knowledge, this is the first time that this charging model is applied to DLCAs and validated with experiments. Overall, Chang's continuum expression (Eqs. 9 and 10) for both spherical and loose agglomerates (error≤±12% when d_m≤100 *nm*; error≤±2% when d_m>100 *nm*) fit the experimental

results (Kn_{ion}=*0.13-0.51)* very well. In this size range, agglomerates have 17% more charges per particle on average than spheres of equivalent mobility size. In contrast, if the values of capacitance or mean charge for particles composed of the same number of PPs are compared, the discrepancies among chain and branched chain agglomerates, DLCAs and compact particles can be much larger (Fig. 2-4). This indicates that the particles of the same volume but different morphologies can have significantly different charging properties. Thus, if coupled with a method to classify particles according to their mass, measuring the charge would be more sensitive to distinguish the structures, and furthermore structure-related parameters such as the particle surface area compared with methods in which the particles are classified according to their mobility diameters.

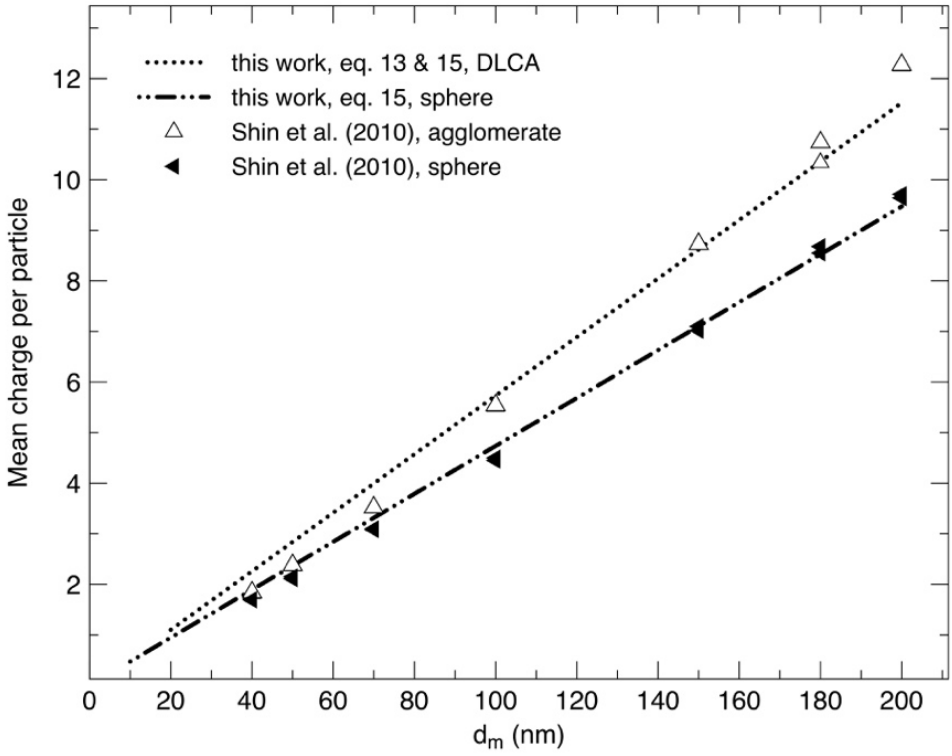

Fig. 2-5. Comparison of mean charge per silver agglomerate (dotted line) and spherical (double-dot broken line) particles as a function of the mobility diameter between the present model and experiments (open and filled triangles) of Shin et al. (2010).

2.3.3 Capacitance and mean charge evolution during agglomerate sintering or coalescence

Figure 6 shows the capacitance evolution of an exemplary agglomerate consisting initially of 128 PPs during viscous flow sintering that is typical of amorphous materials such as polymers and silica. The time t is normalized by the characteristic sintering time $\tau_0=\eta a_0/\Upsilon$, with η and Υ being the particle viscosity and surface energy, respectively, and a_0 the initial PP radius. At the beginning of the sintering process (t/τ_0=0), the agglomerate consists of monodisperse PPs of $a_0=10\ nm$ in point contact having D_f = 1.79 (Eggersdorfer et al., 2011). The PPs approach each other and fuse to minimize the resulting aggregate surface area and grow in radius to conserve their mass (t/τ_0=1-16) until the aggregate fully coalesces to a compact sphere (t/τ_0=45) as shown below Figure 6. The aggregate restructures during sintering increasing D_f from initially 1.79 to finally 3.0 while the radius of gyration decreases to that of the fully coalesced sphere (Eggersdorfer et al., 2011).

The number of spherical elements was controlled within around 30,000, which amounted to around 234 elements per PP for the discretization of agglomerates with 128 PPs. In comparison, around 240 spherical elements per PP already gave reasonable

results for a multiparticle straight chain with a 3% error (Fig. 2-2). At the very beginning of sintering (t/τ_0=0), the particle was composed of distinct PPs in point contact and Brown & Hemingway's (1995) method was used directly.

We start with 50 random agglomerates and evolve each one of them at every single time step. Their normalized capacitance was averaged at every time step. The variation of the normalized capacitance among 50 agglomerates was within ±14% without significant changes through the sintering process. The aggregate capacitance during sintering was normalized by the capacitance of a PP in the initial agglomerate.

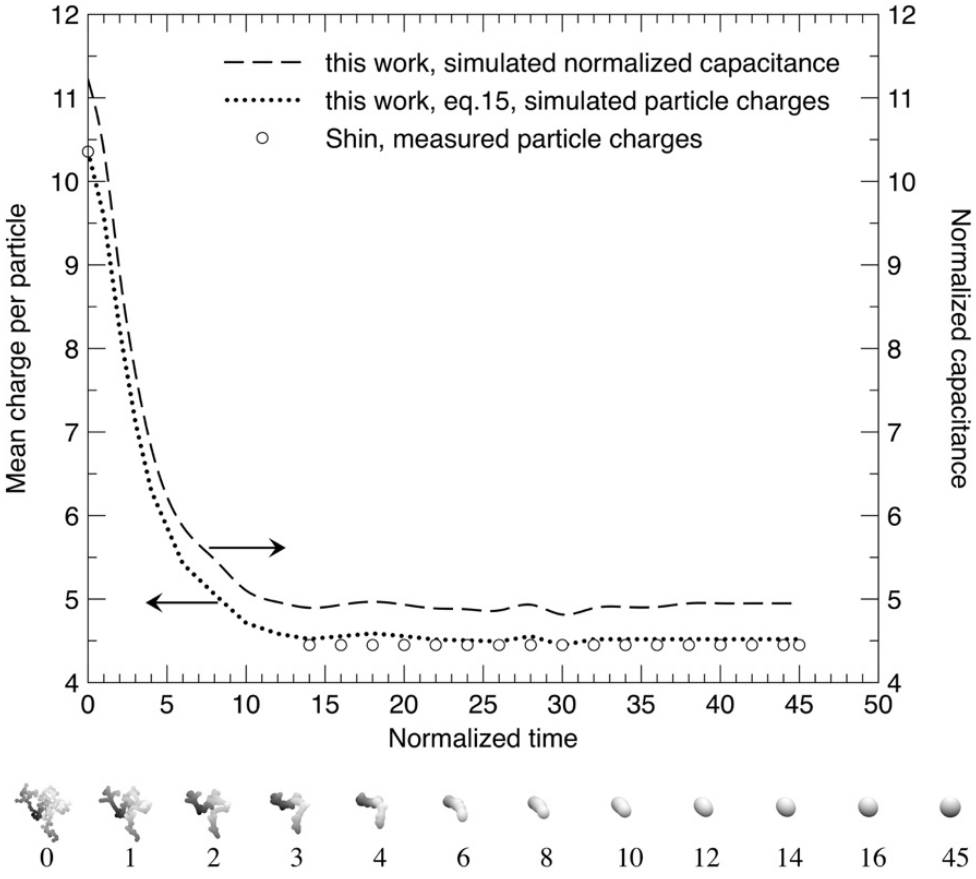

Fig.2-6. Evolution of structure (the color contrast is only for visualization), normalized capacitance, and mean charge per particle for an initial DLCA with 128 PPs undergoing viscous flow sintering. The measured particle charges are from Shin et al. (2010) for sintered nearly-spherical silver particles (corresponding to the data points at $t/\tau_0 > 14$ and $d_m = 100$ nm) and open-structured silver agglomerates (corresponding to the data point at $t/\tau_0 = 0$ and $d_m = 180$ nm).

The capacitance decreased dramatically during neck formation between primary particles that was accompanied by a significant reduction in surface area and mobility diameter ($t/\tau_0<10$) (Eggersdorfer et al., 2011). After the threshold of $t/\tau_0=14$, the capacitance kept stable since the structure changed marginally (Fig. 2-6). The DLCA at $t/\tau_0=0$ had more than twice of the normalized capacitance of the spherical particle at the end of the sintering. These results indicate that agglomerate particle capacitance decreases when its structure becomes more compact consistent with the results presented in Fig. 2-4 that agglomerate particle capacitance decreases with increasing fractal dimension from 1.0 to 3.0 for the same number of PPs.

At different sintering stages, the particles may be extracted and measured, for example, to monitor the morphology. Hypothetically, these particles may be led through a unipolar charger and the mean charge per particle is indicative of their morphology. We assume that a charger with $N_i t=2.5\times10^7\ s/cm^3$ is used (corresponding to the TSI Nanoparticle Surface Area Monitor NSAM), and calculate the resultant mean charge per particle during sintering (Fig. 2-6).

Since particle charge is proportional to normalized capacitance as can be seen from Eq. 15, the evolution of particle charge shares the same trend with that of normalized capacitance. The mean charge of the agglomerate consisting of 128 PPs of about 20 *nm* in diameter (Fig. 2-6, dotted line) decreases from about 10.4 at $t/\tau_0 = 0$ to 4.5 when $t/\tau_0 > 14$. This is in good agreement with the measured mean charge per particle (Fig. 2-6, symbols) from Shin et al. (2010) for sintered nearly-spherical silver particles (corresponding to the data points at $t/\tau_0 > 14$ and $d_m = 100$ *nm*) and open-structured silver agglomerates (corresponding to the data point at $t/\tau_0 = 0$ and $d_m = 180$ *nm*). The correspondence between the sintering time and the particle mobility diameter was from the calculation of d_m at each time step during sintering. Electron microscopic images showed that the open-structured particles in Shin et al. (2010) already had some neck formation. However, these were the charging results for the most open-structured silver particles available, as they were formed in the agglomeration chamber at the room temperature. Therefore, we use them for comparison with simulated results of DLCAs in Figs. 2-5 and 2-6. In any event, the DLCAs do not exactly mimic the silver particle structure and the comparison should be taken as intended for particles with similar structures.

2.4 Conclusions

A discretization method to model the capacitance of arbitrarily shaped particles such as 3D random agglomerates and aggregates was presented. For the simulated

agglomerates with distinct primary particles, Brown & Hemingway's (1995) method was used. For such particle structures, charges were mainly distributed in the periphery or edges of agglomerate branches while PPs in the interior were barely charged. The above method was extended to arbitrarily shaped particles, including compact aggregates and coalesced spheres. Such particles were discretized and represented by finite point-contact spherical elements merely on the particle surface and the elements were treated as primary particles to enable application of Brown & Hemingway's method. The accuracy of the calculation was improved with increasing number of elements.

From the obtained capacitance, the mean charge per agglomerate or aggregate in the continuum regime of charging was modeled using the theory by Chang (1981). The comparison between models and experiments showed that these continuum expressions for both agglomerates and spheres agreed well with experimental results. According to the models, standard (DLCA) agglomerates with D_f= 1.8 had around 17% more charges than an equivalent sphere on average in the mobility diameter range of 20 *nm* to 200 *nm*.

With the discretization method, the evolution of the capacitance and mean charge for agglomerates undergoing sintering was investigated for the first time. During sintering, the capacitance changed dramatically as the initial agglomerate swiftly coalesced into a spheroid and kept steady thereafter as the particle structure only changed marginally. The capacitance and charge of an exemplary agglomerate consisting initially of 128 PPs decreased by more than 50% from the beginning to the end of its sintering or full coalescence.

Therefore, the results here can be used for on-line monitoring of aerosol synthesis and characterization of nanoparticles. If the particles are extracted from the reactor and led through a classifier (a differential mobility analyzer or an aerosol particle mass analyzer) then into a condensation particle counter and in parallel into a unipolar charger followed by a filter connected to an electrometer (Wang et al. 2010), then the signals (the ratio of measured current to aerosol number concentration) can be indicative of the particle morphology (Figs. 2-4, 2-5, and 2-6), facilitating the control and operation of such aerosol processes and the determination of the other geometric properties (e.g. geometric surface area) of particles.

Appendix A:

A.1. Numerical techniques for using the minimum energy method

Eq. 5 consists of *N* linear simultaneous equations. For instance, when *i=1,* Eq. 5 becomes

$$\sum_{j=2}^{N} \frac{Q_j}{4\pi\varepsilon_0 \left| r_1 - r_j \right|} + \frac{Q_1}{4\pi\varepsilon_0 a_1} + k = 0 \,. \tag{16}$$

Based on this, we develop an easy-to-code matrix method to solve the Eqs. 2-6 for all values of *i*:

$$
\begin{aligned}
&X \cdot A = B \cdot Q \\
&\textit{where} \\
&X[i,j] = \frac{1}{4\pi\varepsilon_0 a_i},\ \textit{if}\ \ i = j \\
&X[i,j] = \frac{1}{4\pi\varepsilon_0 \left| r_i - r_j \right|},\ \textit{if}\ \ i \neq j \\
&X[N+1,N+1] = 0 \\
&X[N+1,j] = 1 \\
&X[i,N+1] = 1 \\
&B[i] = 0 \\
&B[N+1] = 1 \\
&i \in [1,2...N] \\
&j \in [1,2...N]
\end{aligned}
\quad , \qquad (17)
$$

$\boldsymbol{X}$ is a $(N+1)\times(N+1)$ matrix, $\boldsymbol{A}$ and $\boldsymbol{B}$ are all column vectors of $N+1$, and Q is a constant (Eq. 2). By solving the above equations for vector $\boldsymbol{A}$, we will have $\boldsymbol{A[1]}$ to $\boldsymbol{A[N]}$ as the individual charge (Q_i in Eq. 2) on every PP and $\boldsymbol{A[N+1]}$ as the Lagrangian multiplier (k in Eq. 5). With individual Q_i, the capacitance could be easily calculated.

A.2. Modified spherical coordinates for discretizing arbitrarily shaped particles

To discretize arbitrary geometries, we take the advantage of spherical coordinates. For instance, the coordinates of the center of an element (x,y,z) for the discretization of a spherical particle (Figure 1a) is expressed as:

$$
\begin{aligned}
&x = R\cos\theta\sin\varphi \\
&y = R\sin\theta\sin\varphi \\
&z = R\cos\varphi \\
&where \\
&\varphi \in [0, d\varphi, 2d\varphi ... md\varphi .. \pi] \\
&\theta \in [0, d\theta, 2d\theta .. nd\theta ... 2\pi]' \\
&d\varphi = d_e \\
&d\theta = d\varphi / \sin\varphi \\
&m \in [0,1,2 .. \pi / d\varphi] \\
&n \in [0,1,2 ... 2\pi / d\theta]
\end{aligned}
\tag{18}
$$

R is the radial distance between the center of a PP (the spherical particle is treated as a PP in this case) and spherical elements, θ is the azimuthal angle from 0 to 2π, φ is the polar angle from 0 to π, and d_e is the diameter of elements. It is noted that the modification of $d\theta$ that depends on $sin\varphi$ is the key to ensure equal size elements point-contact without necking.

For an arbitrarily shaped particle even without distinct PPs, we can still present it as PPs necking together (Eggersdorfer et al., 2011). Then we can locate centers of every PP and discretize them all by Eq. 18 like the above spherical particle case. After this, the raw discretization is finished, however there are still many unnecessary spherical elements. They are the ones generated by one PP falling into other PP's domain, which causes calculation failure of Eq. 5. Thus, we have to check the distance between centers of spherical elements and between centers of every element and PP in order to eliminate unqualified ones.

Chapter 3: Development of a geometric surface area monitor (GSAM) for aerosol nanoparticles

3.1 Introduction

By manipulating the response function of diffusion chargers using an electrostatic precipitator (ESP), different moments of the particle diameter can be measured, such as the number concentration $d^{0.0}$ (Ranjan & Dhaniyala, 2009) and the GSA $d^{2.0}$ (Wei, 2007; Wei et al., 2007). However, the above measurements were only proven for spherical particles and in a narrow size range of 30-90 nm and 20-100 nm, respectively. Using a similar concept in the previously mentioned research, in which the voltage of the ion trap in NSAM was adjusted for the device response function to match the lung deposition curves for measured particles (Fissan et al., 2007), this study further proposes to add an impaction treatment for particles before entering a combination of a charger and an electrostatic precipitator (ESP). That is, a home-made impactor with 100 nm cutoff diameter was applied/or not applied to either (1) allow only particles smaller than 100 nm to enter the charging zone and ESP or (2) send all particles into the charging zone without impaction separation. Additionally, two different voltages (150 or 1000 V) of the ESP were alternatively applied to remove certain fractions of particles according to their electrical mobility so that, for monodisperse aerosol at each mobility diameter, the measured electrical current correlates well with the particle GSA. As a result, the

electrical current of polydisperse aerosol can represent the total GSA very well. That is, with or without passing the particles through the impactor and controlling the voltage of ESP with low (150 V) or high (1000 V) voltage, the measured current of the penetrated particles can be used to determine the GSA for sub-100 nm or particles larger than 100 nm, respectively. This measurement can be conducted in a few seconds so it can be regarded as real-time surface area measurement for particles.

3.2 Methodology and Theory

3.2.1 Theory for measuring geometric surface area

The response function of an electrical sensor for a certain particle diameter is usually defined as sensitivity (Fissan et al., 2007):

$$S(d) = \frac{I}{N} \tag{1}$$

where d is the diameter of the particle, I is the electrical current measured by the electrometer, and N is the particle number concentration at the inlet of the instrument. A typical electrical sensor using unipolar charging (e.g., NSAM) consists of a unipolar charger which charges the aerosols with ions and imposed a certain charge level to particles, an ion trap that removes excess free ions, and a Faraday cup (which may include an absolute filter) connected to an electrometer that measures the electrical current. Unipolar charging will be thoroughly introduced in section 2.2.1. To determine geometric surface area (GSA) concentration (in $\mu m^2/cm^3$), the sensitivity should be

proportional to the geometric surface area of a single particle. For instance, the instrument sensitivity at a specific diameter for a spherical particle has a relationship with the diameter:

$$S(d) \propto \pi d^2. \tag{2}$$

With this, the total GSA concentration is represented by the integration of sensitivities for all sampled particles within the sampled air with a specific volume, which is the total electrical current measured by the instrument.

However, the instrument response in Eq. 2 is difficult to achieve. Wei (2007) combined the methods of unipolar diffusion charging, excess ion removal, electrostatic precipitation, and electrical current measurement in a row to correlate the measured current with the total GSA concentration of particles in the range of 20-100 nm. First, the aerosol was charged in the charger into certain charging statuses based on their sizes. Then, excess ions were removed by an ion trap. After removing excess ions, the charged particles were passed through the ESP, where an electrical field was created, and a fraction of particles were forced to deposit according to their electrical mobility (Eq. 3) and the applied voltage to the ESP. The electrical mobility of charged particles is defined as (Hinds, 1999):

$$Z_p = \frac{neC_c}{3\pi\eta d} \tag{3}$$

where n is number of elementary charges on the particle, e is elementary charge, C_c is Cunningham slip correction factor and $C_c=1+Kn[\alpha+\beta\ exp(-\gamma/Kn)]$, α=1.142, β=0.558, γ=0.999 (Allen & Raabe, 1985), Kn is Knudsen number, and η is gas viscosity. Finally,

the electrical current induced by the particles deposited on the ESP was measured. By adjusting the voltage applied to the ESP, the response of the system was altered and eventually matched the GSA measurement.

Here, using a similar concept as Wei's (2007), we developed a stagnation-point-flow ESP, and placed it into NSAM between the charger and the absolute filter (Fig. 3-1). The charging status of unipolar diffusion charger follows a power law pattern (section 2.2.1); the penetrations of unipolarly charged particles through the ESP can be also fitted into power laws (within certain size range) and the powers depends on the voltage of the ESP (more detail in Appendix A). Therefore, when combining these two mechanisms together, the powers can be added together that allows us to conveniently manipulate the data. By applying different voltages to the ESP, the size distribution of the aerosol reaching the Faraday cup (instead of depositing on the ESP as Wei, 2007) can be manipulated for the size dependence of the measured current to match Eq. 2, at least for certain size ranges, e.g., 16-100 nm and 100-300 nm (two connected but not overlapping regimes).

a)

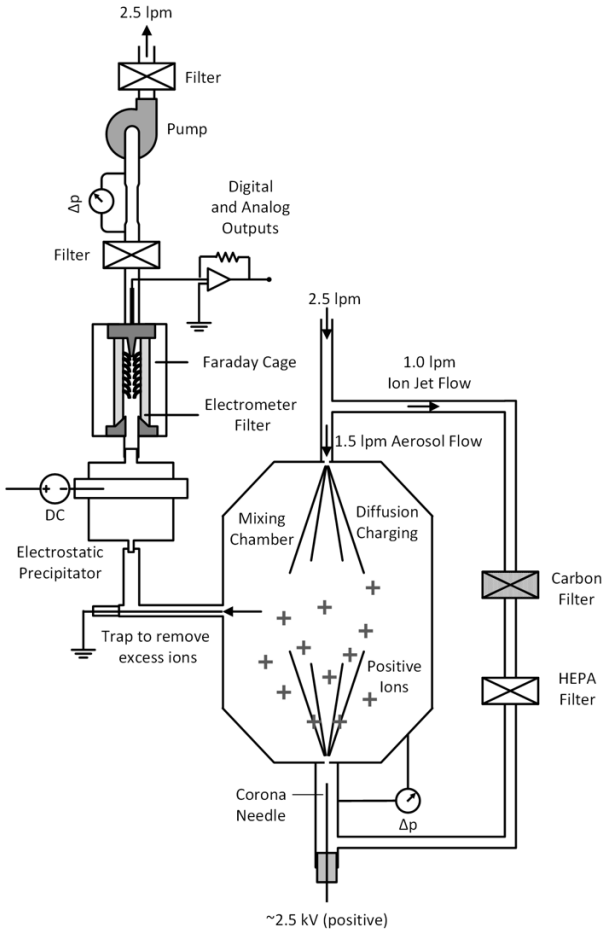
2.5 lpm
Filter
Pump
Δp
Digital
and Analog
Outputs
Filter
2.5 lpm
Faraday Cage
1.0 lpm
Ion Jet Flow
Electrometer
Filter
1.5 lpm Aerosol Flow
DC
Mixing
Chamber
Diffusion
Charging
Electrostatic
Precipitator
Carbon
Filter
Trap to remove
excess ions
Positive
Ions
HEPA
Filter
Corona
Needle
Δp
~2.5 kV (positive)

b)

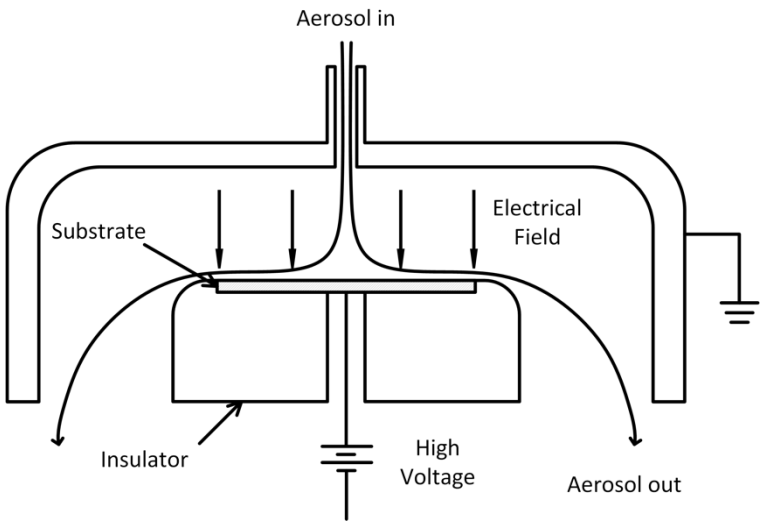
Aerosol in
Substrate
Electrical
Field
Insulator
High
Voltage
Aerosol out

Fig. 3-1. (a) The setup of Geometric Surface Area Monitor (GSAM). The ion trap was turned off. (b) Schematic cross-section of the working zone of the custom-built ESP.

The sensitivity of the instrument can also be correlated with the GSA for particles in all morphologies, although different calibration curves are needed depending on the structure of the investigated particles. Other than spherical particles, loose agglomerates with equally sized primary particles (PPs) are another type of particles considered in this study. The GSA of agglomerates equals $N_{pp}\pi d_{pp}^2$ with the assumption of equally sized PPs without necking, where N_{pp} is the number of PPs in one agglomerate and d_{pp} is the diameter of the PP.

Specifically, diffusion limited cluster-cluster agglomerates (DLCA) generated in an agglomeration chamber were studied as one typical type of agglomerates. Therefore, the following method of calculating the GSA of DLCA was used in the study. Sorensen (2011) provided useful relationships among d_m (mobility diameter), d_{pp}, and N_{pp} for DLCA in the continuum regime,

$$d_m = d_{pp}N_{pp}^{0.46}, N_{pp} < 100,$$

$$d_m = 0.65d_{pp}N_{pp}^{0.56}, N_{pp} > 100 \quad . \tag{4}$$

The mobility diameter of a given particle in an electric field equals the diameter of a spherical particle having the same mobility as the given particle. For a spherical particle, d_m equals d. Although the target particle range is in the slip regime, we chose the equations for the continuum regime as the closest ones. The choice agrees well with Shin

et al. (2010) and Cao et al.'s (2015) simulations. By rearranging Eq. 4, the GSA for one agglomerate can be expressed as a function of d_{pp} and d_m,

$$\pi N_{pp} d_{pp}^2 = \pi d_{pp}^{-0.17} d_m^{2.17}, N_{pp} < 100,$$

$$\pi N_{pp} d_{pp}^2 = 2.16\pi d_{pp}^{0.21} d_m^{1.79}, N_{pp} > 100. \quad (5)$$

Eq. 5 can be used for any DLCA-like agglomerate. However, in this study, only the calibration curves for DLCA-like silver agglomerates generated from furnace was obtained and, thus, d_{pp} of these particles is limited in some range where the reported monodisperse d_{pp} is between 13 and 20 nm (Shin et al., 2009a). Here, we consider three cases: agglomerate composed of monodisperse PPs with diameters of 13.8 (Shin et al., 2009a), 16.2 (Kim et al., 2009), and 19.5 (Shin et al., 2010) nm, respectively, and the average of the results for all three sizes formed the calibration curve.

3.2.2 Experimental setup

3.2.2.1 Diffusion Charging

Particles were electrically charged by the unipolar diffusion charger, where a corona discharge generates either positive or negative ions and gives particles a stable charge distribution based on particle self-capacitance (Fuchs, 1963; Chang, 1981). Fuchs' (1963) and Chang's (1981) diffusion charging theories both contain $N_i t$ number (the product of the ion number concentration N_i and the charging time t in the charger), which

is difficult to measure directly. Other than theoretical models, empirical regression models can also characterize the charging process. Asbach et al. (2011), Kaminski et al. (2012), and Jung and Kittelson (2005) showed similar power laws for the mean charge per particle (total number of charges carried by all the particles divided by total number of the particles) as a function of the mobility diameter for the same charger in NSAM.

We evaluated NSAM using the setup in Fig. 3-2. In the NSAM, ion trap was set to 20 V (only removing excess ions) and the inlet cyclone is not used. The aerosol and ion jet flow is 1.5 and 1 lpm, respectively. We generated nearly spherical particles including KCl, SiO_2, gold, and polystyrene latex (PSL) with Atomizer Aerosol Generator (TSI 3079) and silver aggregates and agglomerates from the tandem furnace system (Ku and Maynard, 2005). The pure nitrogen (purity level 99.999%) was passed through the furnace at a flow rate of 1.5 lpm. 1200°C is used for the first furnace for both the generation of aggregates and agglomerates. 200°C and room temperature was used for the second furnace to generate one type of silver aggregates (open structure but heavily sintered) and DLCA-like agglomerates, respectively. The fractal dimension of above aggregates and DLCA-like agglomerates is 1.5 and 1.78 from model calculation (Fig. 3-6a in Eggersdorfer et al., 2012), respectively. The monodisperse particles classified by the DMA and later neutralized by the Po-210 neutralizer were analyzed by the Condensation Particle Counter (CPC) for the particle number concentration, or alternatively charged by the unipolar charger in NSAM and analyzed by the electrometer for the total electrical current deposited on the filter.

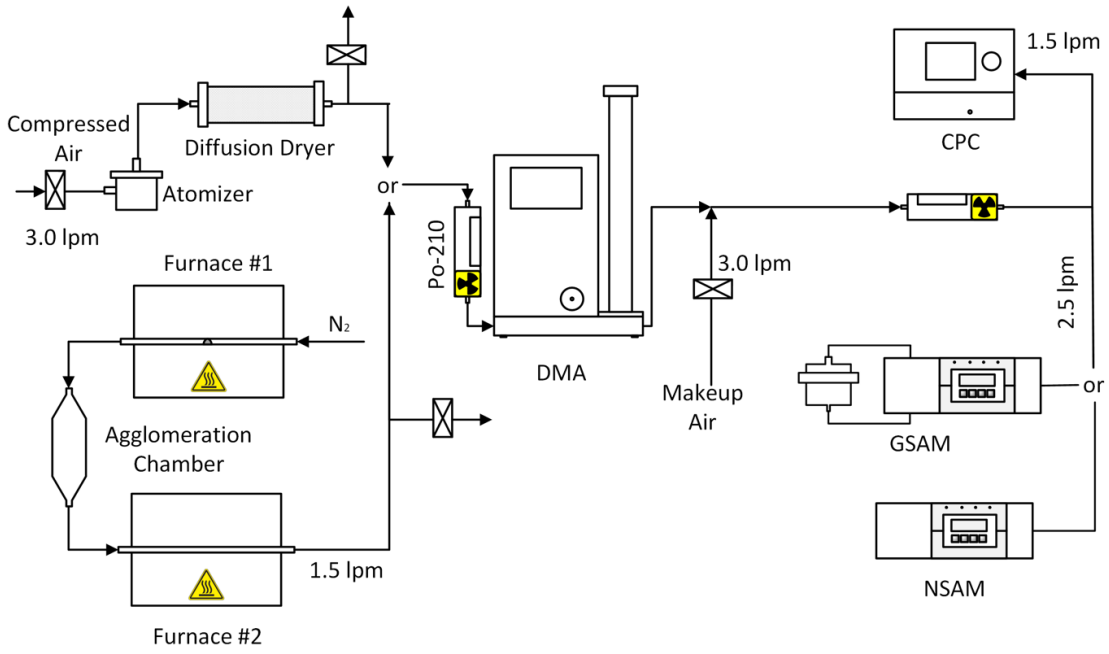

Fig. 3-2. The apparatus for the measurement of mean charge per particle of NSAM and the calibration of GSAM for spherical KCl, and silver aggregates and agglomerates

3.2.2.2 Calibration and validation measurements of GSAM

Fig. 3-2 also shows the apparatus for the calibration of GSAM. Similar as the method used to measure the mean charge of NSAM in section 2.2.1, the monodisperse particle number concentration and the electrical current were alternatively measured. For the latter measurement, the particles were charged by the unipolar charger, precipitated partially based on their electrical mobility by the ESP, and analyzed by the electrometer for the total current deposited on the filter.

After the calibration was done, polydisperse spherical aerosols either mainly in the size range 16-100 nm or 100-300 nm were analyzed using GSAM and SMPS in parallel, and the GSAs measured by both methods were compared.

3.3 Results and discussion

3.3.1 Mean charge per particle

Table 3-1 summarizes the relationship between the mean charge per particle (proportional to the sensitivity) and mobility diameter from different researchers.

Table. 3-1. Summaries of mean charge per particle (assuming spherically shaped) measured by different researchers for the same unipolar charger. Note that Kaminski et al. (2012) slightly changed the charger.

Relationship between mean charge (N_p) and mobility diameter (nm)	Size range (nm)	Reference
$N_p = 0.0211\ d_m^{1.133}$	10-1000	TSI data sheet (2004)
$N_p = 0.0181\ d_m^{1.13}$	30-150	Jung and Kittelson, 2005
$N_p = 0.0244\ d_m^{1.061}$	20-200	Li et al., 2009a

$N_p = 0.0285\ d_m^{1.099}$	30-200	Shin et al., 2010
$N_p = 0.0176\ d_m^{1.133}$	20-246	Asbach et al., 2011
$N_p = 0.0167\ d_m^{1.120}$	19-399	Kaminski et al., 2012
$N_p = 0.0192\ d_m^{1.138}$	16-340	Fig. 3-3 in this study

The relationships are similar, however slightly different. The charge difference could be the overall effect of several factors. They could be the difference of $N_i t$ numbers for each individual chargers caused by manufacturing and aging, the slight baseline difference of the electrometer or the slight contamination of the corona needle. The pre-existing charges on the particles before going into the charger also affect the mean charge (Qi et al. 2009). Another possible origin for the observed (small) difference may also stem from the use of different tube materials for the transport of the aerosols prior to charging (Asbach et al., 2016). In addition to the uncertainty from the chargers, variation in detection efficiency of different CPCs used for the measurement may also play a role. All those uncertainties will eventually affect the measured current and consequently calibration of the GSAM. Therefore, the charging performance should be carefully examined for each individual charger before conducting modelling and experiments.

It is noted that Table 3-1 only shows the mean charge per particle for (nearly) spherical particles. Non-spherical particles can carry more charges than spherical particles of the same mobility diameter in the same charging process (Fig. 3-3) that

agrees with simulations (Shin et al., 2010; Cao et al., 2015) and experiments (Oh et al., 2004; Jung and Kittelson, 2005).

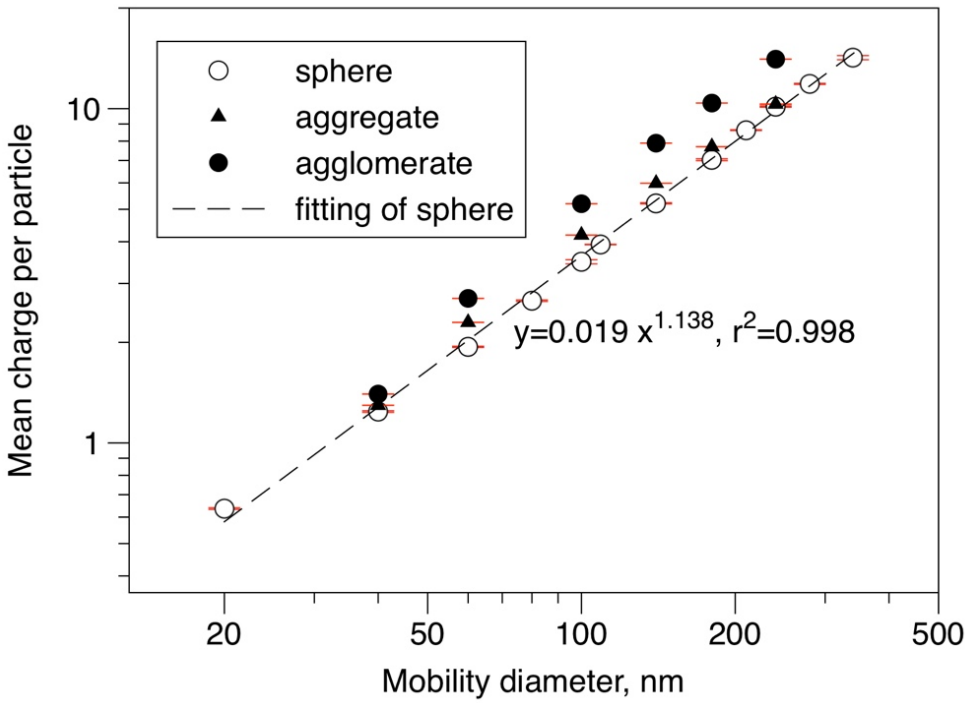

Fig. 3-3. Mean charge per particle measured using NSAM. Spherical KCl, and silver aggregates and DLCA-like agglomerates were tested. Only the data for spherical particles were fitted to a power law relationship.

3.3.2 The calibration curves of GSAM for both monodisperse spherical and agglomerate particles

Fig. 3-4 shows the sensitivity measurements of monodisperse particles with different shapes in two size regimes. We applied 150 V and 1000 V to the ESP for the small and large particle regime, respectively. In each individual regime, the sensitivity correlates strongly with the GSA of spherical KCl particles. However, this strong correlation exists only for a short range, such as 16-100 nm and 100-300 nm, with a high coefficient of determination (r^2) larger than 0.97. Small standard deviations are shown in the figures. In Fig. 3-4b, the sensitivities for particles smaller than 100 nm were much lower than the fitting curve, therefore when measuring the portion of particles larger than 100 nm, those smaller than 100 nm would not significantly affect the total current.

In fact, the sensitivity under 16 and 60 nm for the small and large particle regime was immeasurable due to the particle removal of the ESP (Fig. 3-4b). The electrical mobility at the low end of diameter is much higher than that for the high end. Therefore, when electrostatic precipitation was applied, the removal of charged particles was much more efficient at the low end (high electrical mobility). Not to mention that the sensitivity was already extremely low at the low end in NSAM (Fig. 3-3). Therefore, below some point (e.g. 16 and 60 nm in each regime), the sensitivity in GSAM reduced to zero.

a)

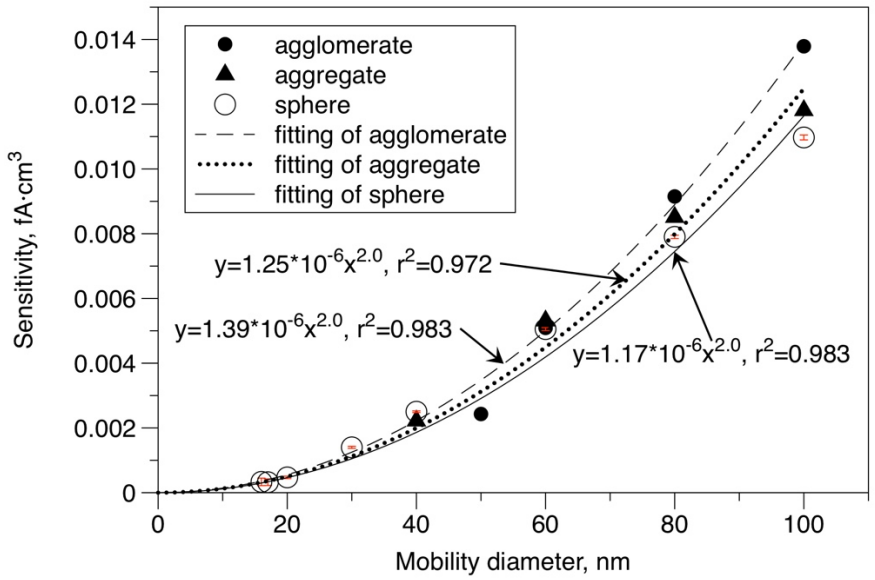

b)

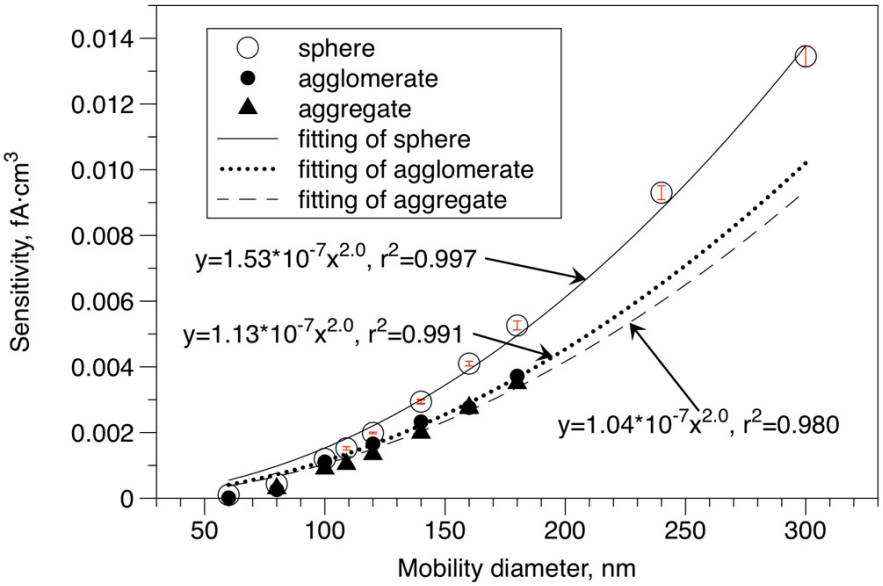

Fig. 3-4. The sensitivity measurement of particles with different shapes in two size regimes: (a) 16-100 nm and (b) 100-300 nm. The fittings in b) are only based on the results of particles larger than 100 nm.

DLCA-like agglomerates and heavily sintered aggregates were also tested. For the same mobility diameter, compared to spherical particles, agglomerates have higher sensitivities during measurements with the lower ESP voltage but lower sensitivities with the higher ESP voltage. This is due to the combined effects of the lower penetration in the ESP (Appendix A) and higher mean charge per particle (Fig. 3-3). Generally, the charging effect dominates in the regime of 16-100 nm, whereas the penetration effect dominates in the regime of 100-300 nm. Also, because of the combined effects, the sensitivities for aggregates and agglomerates are close to each other.

The calibration curves in Fig. 3-4 could work well for all DLCA with different N_{pp} and d_{pp}. Cao et al. (2015) proved that the number of charges that DLCA get from a given unipolar charger was simply as a function of the mobility diameter when $16< N_{pp} <512$, $10\ nm<d_{pp}<90\ nm$, and $36\ nm<d_m<1600\ nm$. In other words, the curves in Fig. 3-4 were independent from N_{pp} and d_{pp} and fit every DLCA. However, d_{pp} may affect the following GSA calculation. Since the GSA for non-spherical particles is not simply πd_m^2, the GSA should be calculated based on the shapes (Eq. 5). Fig. 3-5 shows the sensitivity versus GSA and relationships were fitted using 13.8, 16.2, and 19.5 nm as d_{pp}. 50 nm was also used as d_{pp}, however, only in Fig. 3-5b to check generalization of the calibration curve. The reason of not using 50 nm in Fig. 3-5a is that, with 50 nm as d_{pp}, the corresponding N_{pp} is from 1 to 4.5, which is too small to form DLCA. The results show marginal effect from d_{pp}.

Unfortunately, GSA for sintered aggregates is difficult to determine and wasn't calculated; however, since aggregates have slightly higher GSA than spheres (Fig. 7 in Eggersdorfer et al., 2012; Fig. 6a in Eggersdorfer et al., 2011) but much lower values than agglomerates at the same mobility diameter, the results for aggregates in Fig. 3-5 should be somewhere between that of spheres and agglomerates due to the estimation based on Fig. 3-4.

a)

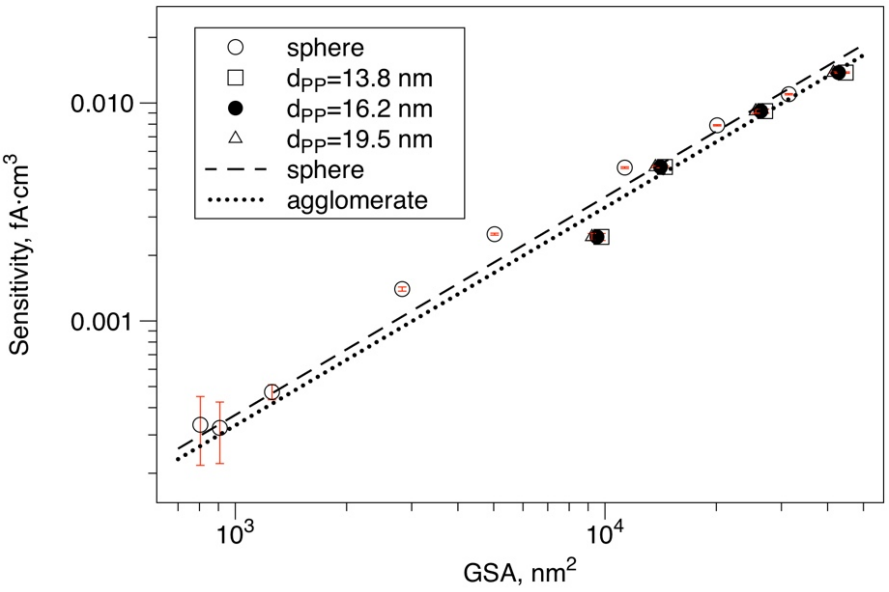

b)

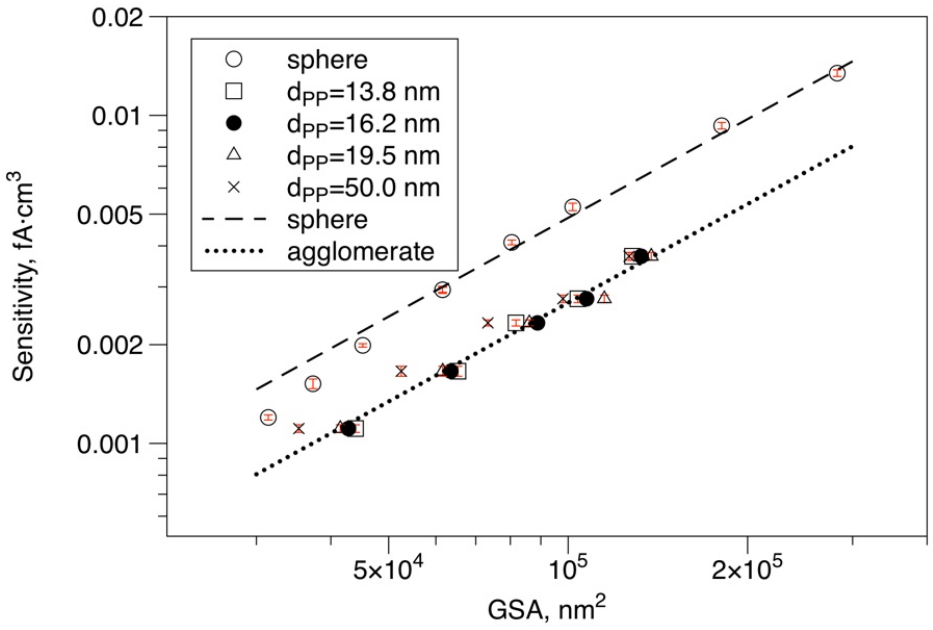

Fig. 3-5. The total current versus GSA concentration for both sphere and agglomerate in the size regime of (a)16-100 nm and (b) 100-300 nm.

To reveal the relationships between total GSA concentration in $\mu m^2/cm^3$ and the current (I) in *fA,* equations were derived from the curves fitted in Fig. 3-5 and The GSA concentration was equal to:

for small sphere (16-100 nm)

$$2.70\ I \tag{6a}$$

for large sphere (100-300 nm)

$$20.53\ I \tag{6b}$$

for small agglomerates (16-100 nm)

$$3.02\ I \tag{6c}$$

for large agglomerates (100-300 nm)

$$37.28\,I \tag{6d}$$

where the constants are in the units of $\mu m^2/(cm^3 \bullet fA)$. The detection limit can be as low as 3 $\mu m^2/cm^3$ since the detection limit of the electrometer is 1 *fA*. With these equations, the GSA concentration for aerosol in the size range of 16-100 nm or 100-300 nm will be easily measured in real-time.

3.3.3 Geometrical surface area (GSA) concentration measurement for polydisperse spherical particles

To measure the GSA of particles in given shape (spheres or DLCA-like), the operation procedures are as follows:

(a) For aerosol exactly in the range of 16-100 nm, apply 150V for the ESP, measure the current, and convert the current into GSA concentration using Eq. 6a for spherical particles and Eq. 6c for agglomerates.

(b) For aerosol exactly in the range of 100-300 nm, apply 1kV for the ESP, measure the current and convert the current into GSA concentration using Eq. 6b for spherical particles and Eq. 6d for agglomerates.

After the calibration using monodisperse particles, we used the system to test the polydisperse spherical particles. Fig. 3-6 shows both the number and surface area concentrations vs. size for three different aerosols generated from the atomizer. Both

aerosols in Figs. 3-6a and 3-6b are targeted as in the small particle regime and to test Eq. 3-6a. In Fig. 3-6c, suspensions of PSL and SiO_2 were mixed in one bottle and atomized together. The resulted aerosol has a multimodal pattern and is targeted as in the large particle regime and to test Eq. 6b. Note that multimodal aerosols are difficult cases and great challenge for aerosol monitors, especially for those assuming unimodal aerosol.

a)

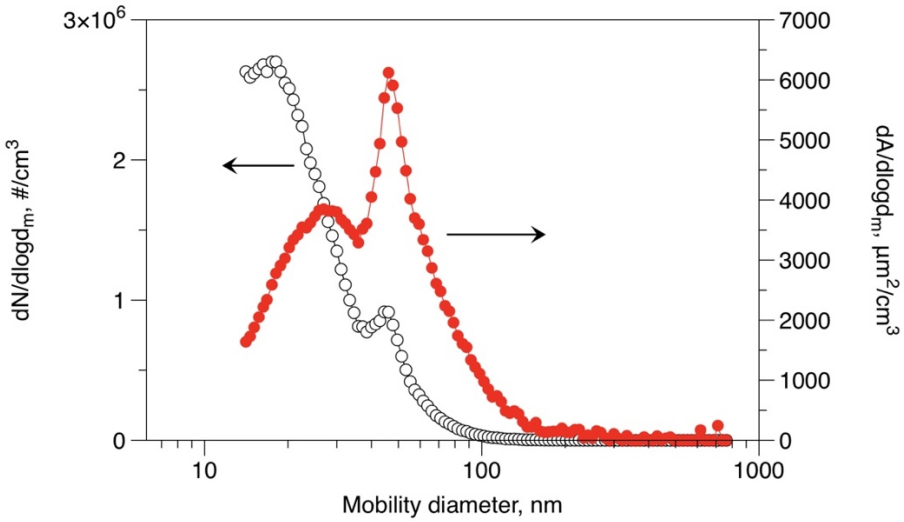

b)

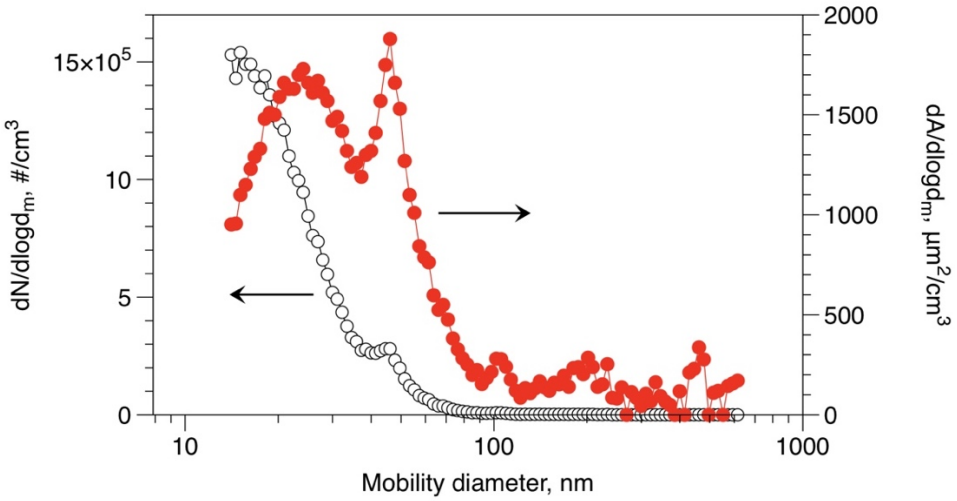

c)

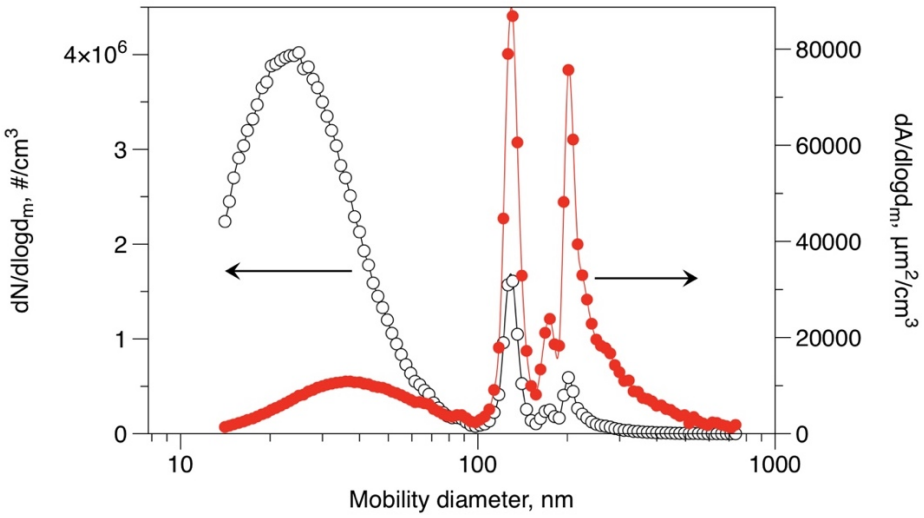

Fig. 3-6. The aerosol distributions of number and surface area concentrations for (a) 40 nm gold colloid, (b) 40 nm gold colloid diluted from Fig. 3-6a, and (c) 125 nm PSL and 200 nm SiO_2 solution out of the atomizer.

Table 3-2 shows the GSA concentration for the three polydisperse aerosols measured by both the SMPS and GSAM. 150V was applied on the ESP for both the cases in Fig. 3-6a and 3-6b and 1000V was applied for the case in Fig. 3-6c. The SMPS and GSAM were in parallel to measure the aerosol generated from atomizer and neutralized by the neutralizer. When analyzing the GSA concentration data from SMPS, data for particles larger than 16.3 nm (detection limit of GSAM for the small particle regime) were used for both cases in Fig. 3-6a and 3-6b for comparison; data for particles larger than 101.8 nm was used for the case in Fig. 3-6c since GSAM (for the large particle regime) can mainly measure the portion of aerosol larger than 100 nm. Also, the GSA concentrations from SMPS for the whole scanning size range (14.1-736.5 nm) are also shown in the figure. GSAM had a 1 and 9% overestimation and 9% underestimation compared with SMPS for cases in Fig. 3-6a, 3-6c and 3-6b, respectively. For the case in Fig. 3-6c, less than 2% overestimation comes from the electrical current (calculated from Fig. 3-4) for particles larger than 60 nm and smaller than 100 nm. Although the fact that the tested aerosols are out of range to some extent causes error, the major reason for the discrepancies for all the cases is still the difference between the regression models and experimental data in Fig. 3-4. Note that the measurements from GSAM for cases in Figs. 3-6a and 3-6b is accurate even when the range of GSA concentration data from SMPS is from 16.3-736.5 nm instead of 16.3-100 nm (working range for the small particle regime).

Table. 3-2. The comparison between GSA concentration measured by SMPS and that calculated from measured current by Eq. 6a and 6b.

Aerosol distribution	Size range (nm) for GSA in SMPS	GSA concentration from SMPS ($\mu m^2/cm^3$)	GSA concentration by Eq. 6 ($\mu m^2/cm^3$)	Voltage applied on the ESP
Fig. 3-6a	16.3-736.5 nm (14.1-736.5 nm)	2.83E+3 (2.94E+3)	2.86E+3	150V
Fig. 3-6b	16.3-736.5 nm (14.1-736.5 nm)	1.03E+3 (1.09E+3)	9.33E+2	150V
Fig. 3-6c	101.8-736.5 nm (14.1-736.5 nm)	1.56E+4 (2.13E+4)	1.70E+4	1000V

The instrument is suitable to measure GSA of aerosols with size distributions which are either below or above 100 nm. Unfortunately, aerosols in practice are not always in those specific regimes while Eq. 6 only works in these regimes. In that case, aerosols need to be divided into different regimes and measured separately. For the regime of 16-100 nm, we propose to use an inertial impactor right before the

measurement. The impactor allowed particles smaller than certain diameter to pass through. Under certain condition, the cutoff size can match the upper limit of the measurement for small particle regime. For large particle regime, the lower size limit was already set due to the strong removal of particles smaller than 100 nm of the ESP with high voltage. The upper limit is still needed to be set and a cyclone can be considered. Thus, the combination of two separated measurements in two regimes may provide a solution to cover the full size range.

The inertial impactor we used was developed by Tsai et al. (2012). This impactor had a cut-off aerodynamic diameter at 100 nm at a flow rate of 2 lpm. We analyzed the penetration of KCl particles through the impactor at a different flow rate of 1.5 lpm and Fig. 3-7 shows the results in both mobility and aerodynamic diameter. The cut-off aerodynamic diameter shifted from 100 nm at 2 lpm to 150 nm at 1.5 lpm. At 1.5 lpm, the impactor efficiently removed particles larger than around 100 nm (mobility diameter). With appropriate correction, the impactor could help the system to measure GSA for particles in the small particle regime. However, the penetration curves will vary for aerosols with different densities and shapes. Also, although the pressure drop created by the impactor is only 13.1 kPa at 2 lpm (Tsai et al., 2012), the aerosol to ion flow ratio in the charger will still be affected once the impactor was installed prior to the charger and the charging status of the aerosol may be different from the calibration. Thus, further research is needed to resolve the mentioned open questions.

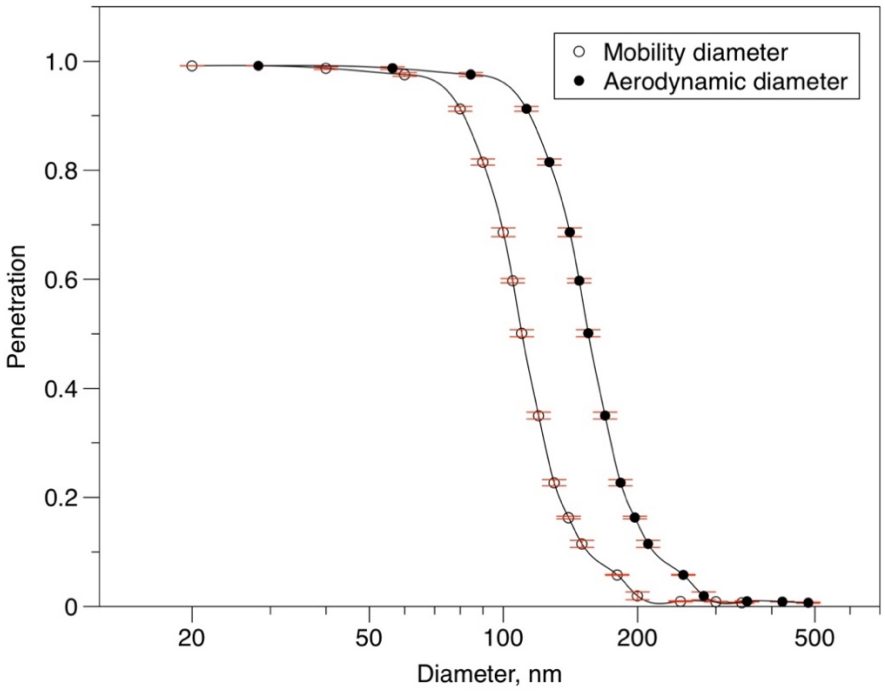

Fig. 3-7. The penetration (in both mobility and aerodynamic diameters) of KCl particles through the impactor.

3.3.4 The advantages and disadvantages of the GSAM

So far, GSAM is the only instrument, capable of online measuring the geometric surface area of spherical and model agglomerate particles. The measurement of the mean charge per particle from diffusion charging has little dependence on particle material. Li et al. (2009b) and Shin et al. (2009b) showed slight effect of dielectric constant on the measurement of mean charge. On the other hand, number concentration of the aerosol

barely affects the charging status if the concentration and the associated current allow reliable electrometer measurement.

The drawback of GSAM is that GSAM is currently limited to spheres and DLCA-like agglomerates (two extreme possible cases) and the types of particles must be known before measurements. As a result, inaccuracy may occur using Eq. 6 for the measurements for particles in shapes that are not discussed in this study (e.g., straight chain agglomerate, ballistic-limited cluster-cluster agglomerate, or randomly shaped aggregates) and even the mixture of different particle types (e.g., the mixture of spherical and DLCA particles or non-spherical particles with different structures).

There are other shortcomings to be discussed. GSAM has higher detection limit for both particle size and concentration than the original NSAM due to the deducted signal carried by the charged particles that were removed by the ESP, e.g., the current signal cannot be detected when particle size is smaller than 16 nm when doing the small size range measurement. Fortunately, on the other hand, the lower sensitivity when particles are smaller than 100 nm in Fig. 3-4b helps to create a regime for large particles. The upper size limit of 300 nm is another shortcoming of this method. Particles larger than 300 nm may affect the measurement, especially when large amount of those particles exist. In that case, a pre-separator (Asbach et al., 2011), such as a cyclone, should be considered and used prior to GSAM.

3.4 Conclusion

Although many powerful aerosol instruments for particle measurements are available, an appropriate GSA concentration monitor is still lacking. This study developed a system (GSAM) that can quickly deliver the GSA concentration of particles in a wide particle size range, i.e., 16-300 nm. the approach combines the inertial impaction, unipolar charging, electrostatic precipitation, and current measurement in which all the devices were well calibrated. Based on different assumptions of the particle size range, GSAM applies to both spherical and DLCA-like agglomerate particles with different calibration curves.

Appendix A:

A.1. The penetration of the ESP

Fig. 3-8 shows examples of the penetration curves of the ESP under 150, 500, and 1000 V using the setup in Fig. 3-2. The penetration here was defined as the ratio of measured electrical current when the voltage is turned on to that when voltage is turned off. In the test, we used unipolarly charged particles including spheres, aggregates, and agglomerates that were from 25 to 280 nm. In Fig. 3-8, the penetration results follow a similar trend that the slope decreases as the sizes increase.

a)

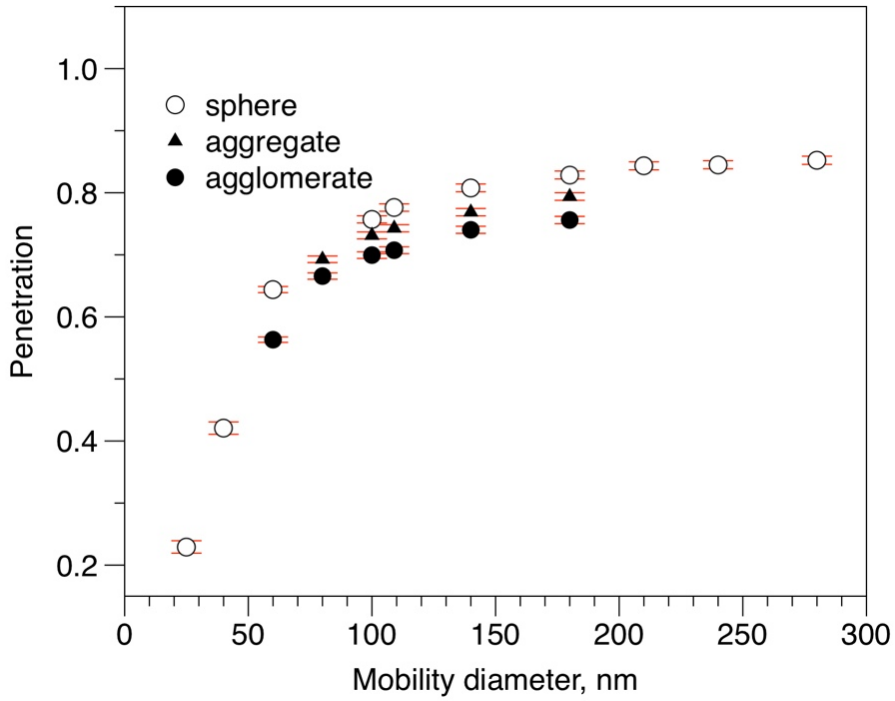
sphere
aggregate
agglomerate
Penetration
Mobility diameter, nm
1.0
0.8
0.6
0.4
0.2
0
50
100
150
200
250
300

b)

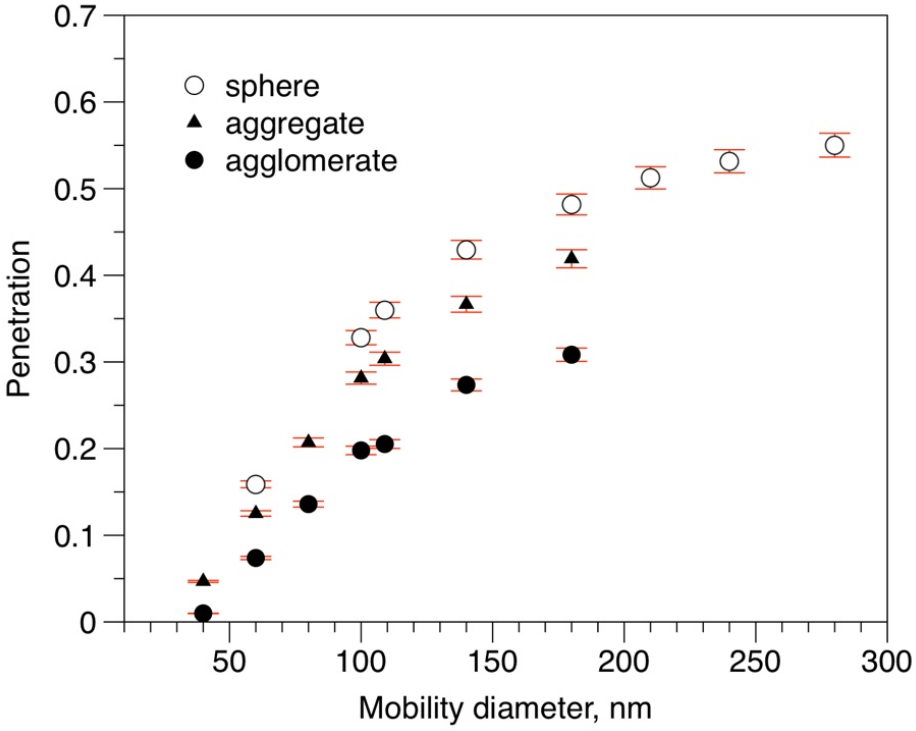
sphere
aggregate
agglomerate
Penetration
Mobility diameter, nm
0.7
0.6
0.5
0.4
0.3
0.2
0.1
0
50
100
150
200
250
300

c)

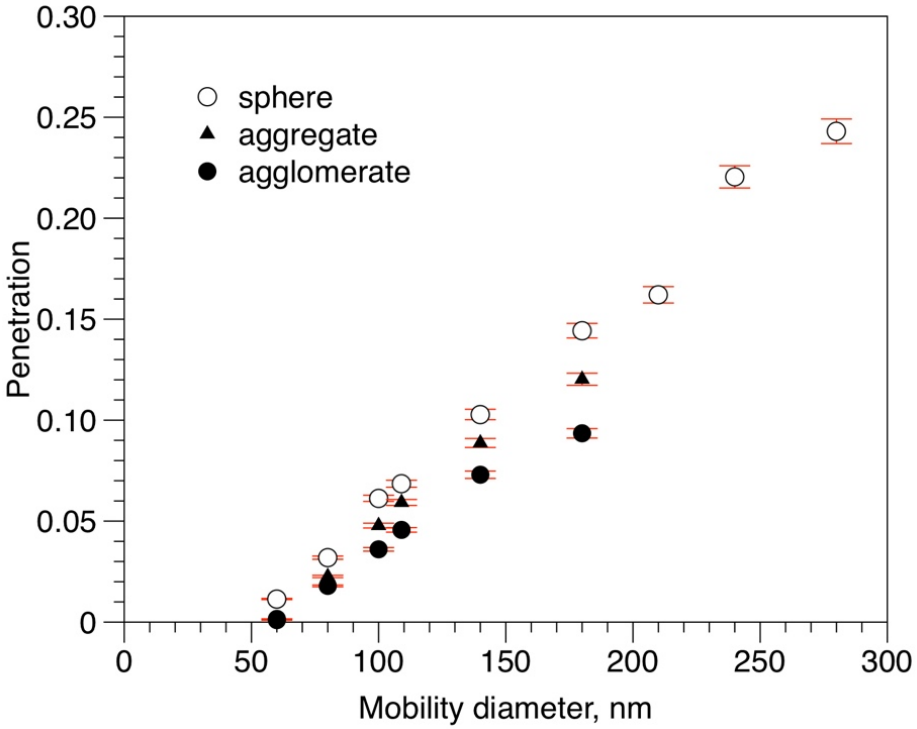

Fig. 3-8. Penetration of unipolarly charged particles through the ESP with the voltage of (a) 150, (b) 500, and (c) 1000 V.

Chapter 4: A novel weighted sum method to measure particle geometric surface area in real-time

4.1 Introduction

Due to its good indication of the nanoparticles reactivity (Hood, 2004), catalytic capacity, and adverse health effect (Oberdörster, 2000), the geometric surface area (GSA) of nanoparticles is of great interest in many fields (Redhead et al., 2001; Oberdörster et al., 2005; Schmid & Stoeger, 2016). The GSA of the particles that is the envelope surface area drastically increases with a decreasing particle size at an equivalent mass; in fact, the GSA increases by a factor of 10, when the particle diameter decreases by a factor of 10. Furthermore, Preining (1998) stated that the fraction of atoms at the surface of a particle increases from 12% to 100% as the particle diameter decreases from 20 to 1 nm. Thus, nanoparticles that have a much larger GSA-to-volume ratio than larger particles can easily interact with other substances and, therefore, the GSA is a worthwhile metric to track the nanoparticles in many circumstances. However, it is difficult to measure the GSA of aerosol nanoparticles because it rarely correlates with any detection approach.

A few techniques can measure the GSA or properties close to the GSA in different measuring time and expense scales. One way is to sample the particles on site and analyze them offline in the laboratory afterward. For instance, the BET analysis (Brunauer, S., Emmett, P. H., & Teller, E., 1938) estimates the capability of a solid surface absorbing gas that refers to the specific surface area; electron-microscopy based

methods (TEM or SEM) provides the two-dimensional projection of sampled particles. Another way is the well-known quasi-real-time scanning mobility particle sizer spectrometer (SMPS, Wang & Flagan, 1990). The size-resolved SMPS scans the aerosol number-size distribution with a time resolution of typically between 50 and 300 s and provides the total particle surface area (assuming spherical particles) based on the integrated distribution. The third method is real-time monitors based on unipolar diffusion charging. For example, the nanoparticle surface area monitor (NSAM, model 3550, TSI Inc, Shoreview, MN, Fissan et al., 2007), DiSCmini (Testo AG, Lenzkirch, Germany, Fierz et al., 2011), NanoTracer (Oxility BV, Best, Netherlands, Marra et al., 2010), and Partector (Naneos Particle Solutions, Windisch, Switzerland, Fierz et al., 2013) claim to monitor the particle lung deposited surface area (LDSA) concentration for a reference worker. By coupling NSAM with a stagnation-point-flow electrostatic precipitator and inertial impactor, Cao et al. (2017) developed a geometric surface area monitor with limited working ranges (20–100 nm and 100–300 nm). Until now, none of them gave the satisfactory real-time measurement of GSA.

Here, a novel weighted sum (WS) method was developed to measure the particle GSA concentration. The WS method used NSAM as the main instrument and, in order to correlate with and thus represent the integral particle GSA concentration, we combined the responses of NSAM under a selected pair of conditions in a weighted sum fashion. The selection of condition was guided by both experiments and simulations and followed by the response measurements at these selected conditions and the WS combination that was determined by the curve fitting. The whole WS method was then validated by

comparing with SMPS in both laboratory testing and environmental sampling. The uniqueness of the WS method is: (1) for the first time the GSA concentration can be delivered in real-time over the desired size range; (2) the method makes no assumptions of the distribution of the aerosol, such as the geometric standard deviation and a unimodal lognormal distribution; (3) since the method only involves a slight modification of the commercialized NSAM, manufacturers can easily redesign the instrument and researchers can conveniently conduct follow-up studies of GSA measurements with their own instruments. In section 4.2, we introduce the major mechanisms and explain the rationale of the WS method; in section 4.3, we describe the apparatus for both the calibration and validation measurements; in section 4.4, the calibration using monodisperse spherical aerosol and the WS combination are discussed and the results of validation measurements using synthetic and natural aerosols are reported.

4.2 Theoretical background

To measure the total geometric surface area (GSA) of polydisperse nanoparticles, the instrument needs a linear response to the aerosol GSA and an instrument sensitivity as a function of GSA per particle (Fissan et al., 2007). The instrument sensitivity (S) corresponds to the instrument signal caused by one particle (Fissan et al., 2012). For instance, the needed sensitivity is proportional to the exponent of 2.0 of the particle diameter (d) for spherical particles:

$$S(d) \propto \pi d^{2.0}. \quad (1)$$

As a result, the signal of the instrument can be linearly transferred into the total aerosol GSA (detailed derivation in section 2.3) even without assuming the geometric standard deviation and a unimodal lognormal distribution of the aerosol. However, so far, very few mechanisms can appropriately correlate the sensitivity with the GSA. Fortunately, we have created and obtained the $d^{2.0}$-dependent sensitivity by applying unipolar diffusion charging, electrostatic precipitation, and electrical current measurement in sequence, and combining the resulted current signals in a weighted sum (WS) fashion. The exact expression for *S(d)* was determined using monodisperse aerosols during calibration and later applied for laboratory-generated and environmental polydisperse aerosols.

4.2.1. Unipolar diffusion charging

Due to their size-dependent sensitivities (Chang, 1981; Jung and Kittelson, 2005), electrical sensors employing unipolar diffusion charging have the potential to measure the GSA in real-time. One of the sensor, nanoparticle surface area monitor (NSAM, TSI 3550, Fig. 4-1), was used here as the basis instrument for the method development. In NSAM, the aerosol is first charged by positive ions in the mixing chamber, then the extra ions are removed by the trap (20 V is the default voltage to remove excess ions) due to electrostatic precipitation, and finally, the total current carried by the aerosol leaving the trap is measured by the electrometer and amplifier. The sensitivity of the electrical sensor

is defined as the ratio of measured electrical current to the total number concentration of the sampled aerosol (Fissan et al., 2007) at a certain particle diameter (d) under certain trap voltage (V):

$$S(d,V) = \frac{I(V)}{N} \tag{2}$$

where I is the current measured by the electrometer under the trap voltage V, and N is the total number concentration measured by CPC at the inlet of NSAM. When the trap is set to 20 V for the same charger, researchers showed a similar power-law relationship in both experimental measurements (Jung and Kittelson, 2005; Asbach et al., 2011) and the numerical simulation (Cao et al., 2015):

$$S(d) \propto \pi d^{1.13}. \tag{3}$$

However, the 1.13 power of d in Eq. (3) does not satisfy the GSA concentration measurement and should somehow increase to 2.0.

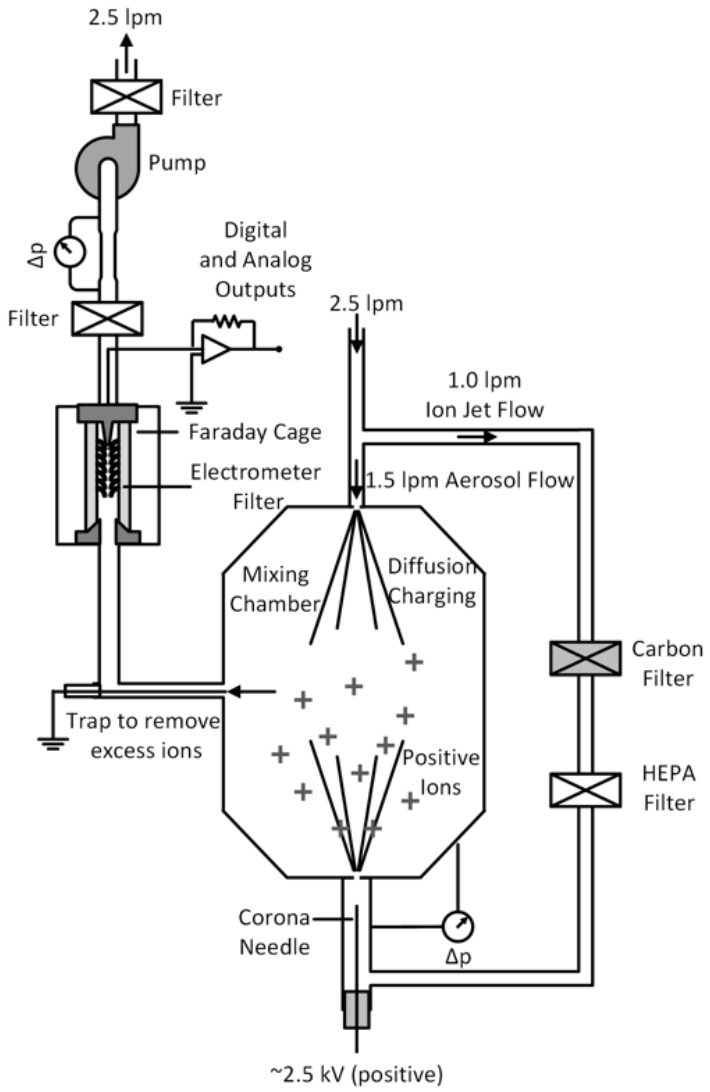

Fig. 4-1. The schematic diagram of the nanoparticle surface area monitor (NSAM).

4.2.2. Unipolar diffusion charging coupled with electrostatic precipitation

By means of electrostatic precipitation, the power in Eq. 3 can be manipulated close to 2.0 (Wei 2007; Li et al., 2009; Cao et al., 2017). In Li et al. (2009), when the trap

voltage (same model as this study) reached as high as 2500 V, the sensitivity was proportional to $d^{2.2}$ in the range of 40-160 nm. Wei (2007) also achieved Eq. 1 in the size range of 10-100 nm using a different unipolar charger followed by a custom-built electrostatic precipitator.

However, electrostatic precipitation has its limitations with respect to the signal manipulation: it removes lots of charged particles, which reduces the signal of the instrument and therefore lowers the signal and even size limit. Since the removing of electrostatic precipitation increases as the electrical mobility increases, particles with large electrical mobility (small particles in the case) are heavily removed. Therefore, a portion of the aerosol distribution is entirely lost during the measurement. For instance, in Li et al. (2009), electrical current for particles smaller than 30 nm was rarely measured when the trap voltage was set to 2500 V. In addition, under certain circumstances, particles at above range can be of most interest, for example, in the release process of engineered nanoparticles (Hagendorfer et al., 2010). Therefore, the dilemma here is that electrostatic precipitation can positively manipulate the sensitivity but lower the detection limit of both size range and signal.

4.2.3. Weighted sum sensitivities

To inherit the advantage and overcome the drawback of the coupling between the unipolar charging and electrostatic precipitation, we propose the weighted sum (WS)

method to further manipulate the instrument response. The WS method linearly combines the sensitivities at different voltages for the electrostatic precipitator in the case of the trap of NSAM:

$$S_{WS}(d, V_1, V_2, c) = S(d, V_1) + cS(d, V_2) \quad (4)$$

where $S(d, V_1)$ is the sensitivity at a low voltage, $S(d, V_2)$ is the one at a high voltage of the trap, and c is the constant weighting factor that can be determined by the instrument calibration. Due to Eq. 4, the linear combination only happens between sensitivities at two different voltages at each particle size.

In Eq. 4, when the low voltage is applied, only extra ions from the charger are removed; when the high voltage is applied, a higher power of the diameter-dependence of the sensitivity can be achieved. In other words, $S(d, V_1)$ mainly serves as a baseline that covers a wide measuring size range and $S(d, V_2)$ primarily serves as a tool to increase the power of the diameter-dependence of the sensitivity. However, since $S(d, V_2)$ is some magnitudes lower than $S(d, V_1)$, a larger-than-1 weighting factor c that can be determined by curve fitting is applied in the linear combination. Finally, with a certain combination of V_1, V_2, and c, the GSA-concentration-proportional response can be achieved:

$$kS_{WS}(d, V_1, V_2, c) = \pi d^2 \quad (5)$$

where k is a constant that can be easily determined when S_{WS} is known.

Since the combination of the measured currents for polydisperse aerosol can be expressed as:

$$I_{WS} = I(V_1) + cI(V_2)$$

$$= \int_{d=0}^{+\infty} S(d, V_1) dN(d) + \int_{d=0}^{+\infty} cS(d, V_2) dN(d)$$

$$= \int_{d=0}^{+\infty} [S(d, V_1) + cS(d, V_2)] dN(d)$$

$$= \int_{d=0}^{+\infty} S_{WS}(d,\ V_1, V_2, c)\mathrm{d}N(d)$$

$$= \frac{1}{k} \int_{d=0}^{+\infty} \pi d^2 dN(d)$$

(6)

where *N(d)* is the number concentration for each particle diameter and $\int_{d=0}^{+\infty} \pi d^2 dN(d)$ is the GSA concentration,

then

$$GSA\ concentration = kI_{WS}. \quad (7)$$

Therefore, the measured current from the polydisperse aerosol can be conveniently transferred into the total GSA concentration. Note that V_1, V_2, and c in Eq. 4 are the essential parameters that will be discussed and determined in section 4.4.1 and 4.4.2.

4.3. Experimental setup

The investigations involve the characterization of the trap, the measurement of sensitivity (for calibration) and validation of the weighted sum (WS) method. The characterization of the trap will facilitate the chosen of two trap voltages (section 2.3). Based on the characteristic penetration curve obtained in the characterization, the sensitivity for given particle diameter and trap voltage can be modeled (section 4.1)

where the candidate voltages can be determined. After determining the voltages, the calibration based on the chosen voltages will be conducted using monodisperse aerosol. Finally, the WS method will be validated by challenging it with polydisperse aerosols.

4.3.1. Penetration measurement of the trap using singly charged particles

To determine the voltages in Eq. 4, the trap was thoroughly investigated and a characteristic penetration curve was obtained. The aerosol penetrations through the trap with different voltages were measured using the setup shown in Fig. 2. KCl solutions 0.01% and 1% (by mass) were nebulized by the atomizer aerosol generator (TSI 3079), and classified by the differential mobility analyzer (DMA, TSI 3081; 9.0 lpm as the sheath flow and 1.5 lpm as the aerosol flow) into singly charged monodisperse particles whose diameter was from 20.5 to 300 nm or technically particles with uniform electrical mobility (Knutson & Whitby, 1975). Then these particles were supplied to the charger and then trap in NSAM (boxed area in Fig. 2) where the charger is off at all times (no voltage supplied to the corona needle). The reason we turned off the charger is that, with the charger off, particles passing the trap with the uniform electrical mobility will have uniform penetration through electrostatic precipitation (section 4.1), while, with the charger on, the unipolar diffusion charging will bring the uniform electrical mobility of particles to a wider distribution (Kaminski et al., 2012) which causes uncertainty of the penetration. For every particle size, the trap voltage gradually increased from 20 to 2400 V that was always supplied by a high voltage power supply (series 230, Bertan associates Inc.) in the entire study. The number concentration of the remaining particles was then

measured by CPC. The penetration was defined as the ratio of the measured particle number concentrations with the trap voltage on and off, respectively (Qi et al. 2009) and accordingly this penetration focuses on the particle removal of the trap due to electrostatic precipitation and excludes other mechanical loss. It is noted that although the characteristic penetration curve was established with charger off, the curve will also work with charger on that will be explained in section 4.1.

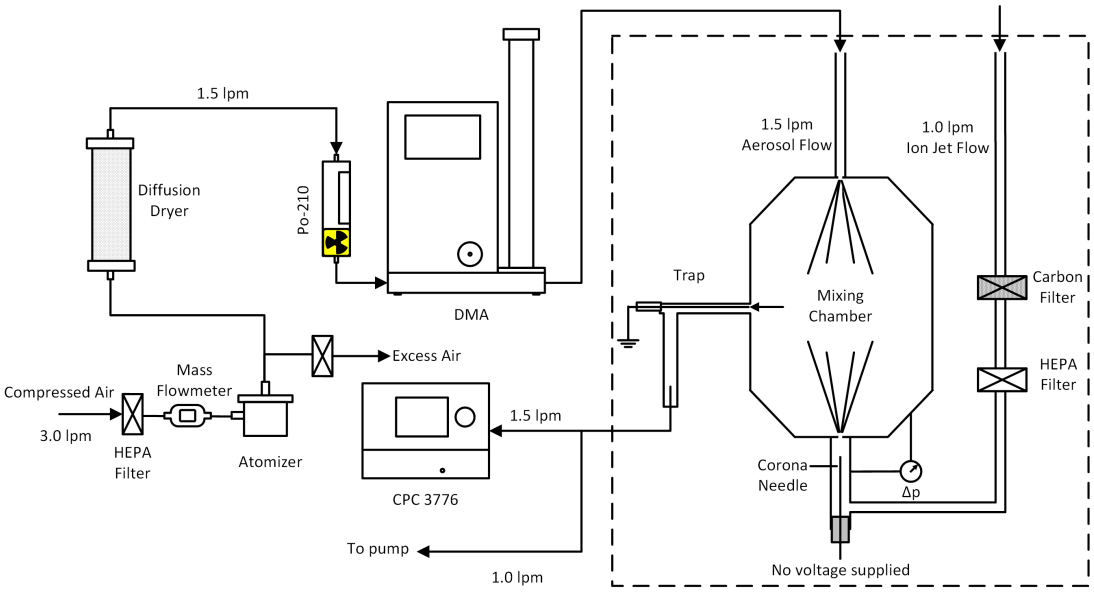

Fig. 4-2. The schematic diagram of the penetration measurement.

4.3.2. Sensitivity measurement

The sensitivity measurements were conducted using the setup in Fig. 3. KCl particles generated using the same method as in section 3.1 and classified by the tandem DMA (6.0 lpm as the sheath flow and 1.0 lpm as the aerosol flow) technique, which

minimizes the production of multiply charged particles (Yook et al., 2008). The number concentration of the monodisperse particles was then measured by CPC; alternatively, the electrical current of the particles was simultaneously measured by NSAM at a given trap voltage. As described in Eq. 2, the ratio of the responses from NSAM to CPC is thus the sensitivity with different voltages. When the size selection changed in DMA, sensitivity for every selected size for a given voltage was obtained.

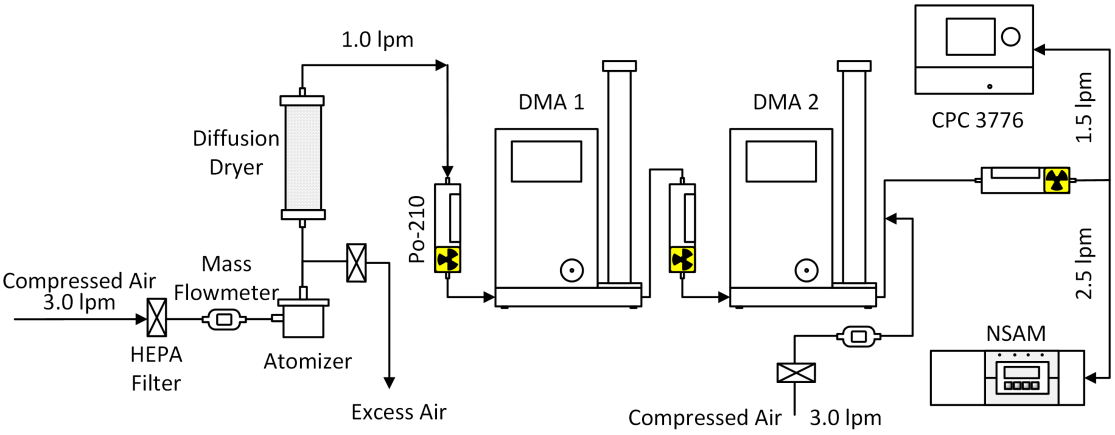

Fig. 4-3. The schematic diagram of the sensitivity measurement.

4.3.3. Laboratory validation measurement

Since SMPS (TSI 3082) is size-resolved, quasi-real-time, and based on the mobility diameter which equals to the diameter of spherical particles, it is so far one of the most appropriate reference methods to validate the WS method in real-time GSA measurement of the synthetic nearly spherical particles. The comparison measurements

of the GSA concentrations of the produced polydisperse aerosols were conducted using the setup in Fig. 4. We used 0.3 lpm as the aerosol flow rate and 3 lpm as the sheath flow rate of DMA. Nearly spherical polydisperse aerosols were generated from the atomizer aerosol generator (TSI 3079) using solutions including 0.01% and 1% KCl, 0.01% and 0.03% Di-Ethyl-Hexyl-Sebacat (DEHS), and commercialized gold colloid (Ted Pella, Inc.) labeled as 50 nm. After the particle generation, SMPS and WS were paralleled to analyze the aerosols. It is noted that the neutralizer of SMPS is also connected to WS to neutralize the highly charged particles from the atomizer into the Boltzmann charge equilibrium. However, the neutralization is unnecessary for the field measurement in section 3.4 since particles in the atmosphere are assumed in the Boltzmann charge equilibrium.

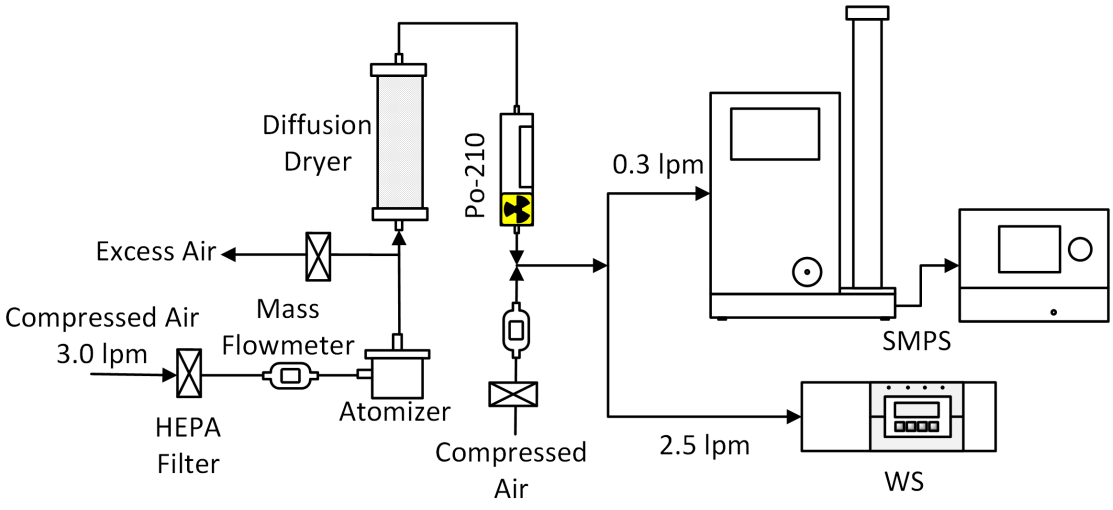

Fig. 4-4. The schematic diagram of the validation measurement for laboratory testing.

During the testing, every scan of SMPS lasted 120 s; as for electrical current measurement of WS, the trap voltage was switched automatically (controlled by the program LabVIEW 15) between the low and high voltages in a block-wise style. It took 3 s for the current to be stable when switching from the low to high voltage and 2 s for the instrument to obtain the current for each voltage. Therefore, to obtain a valid data point of the GSA concentration, the WS method only requires 5 s, which is much faster than SMPS. Meanwhile, we also measured the lung-deposited surface area (LDSA) and discuss its relationship with the GSA, since LDSA is a controversial surface area especially in the discussion of the adverse health effect of nanoparticles. Several sets of measurements were conducted applying 100 and 200 V for the trap to measure LDSA of several aerosols (most particles are below 300 nm) at the tracheobronchial (TB) and alveolar (A) regions of the human lung, which is claimed by the manufacturer of NSAM (Fissan et al., 2007).

4.3.4. Field measurement

Continuous field samplings were conducted using WS and SMPS in parallel. Different from the laboratory test, every scan of SMPS lasted 60 s which is half of the time in the laboratory test since the aerosol concentration in the field can be more transient than in the laboratory. The first test (~5 h) was to challenge the clean indoor air in the laboratory controlled by HVAC system (heating, ventilation, and air conditioning). The second measurement was an outdoor sampling, which lasted 5 continuous days from

Friday (May 12, 2017) to Tuesday (May 16, 2017) including weekdays and weekends. The sampling inlet was located slightly higher than human respiration level (about 2 m above the ground). Less than 20 m away from the sampling site, a building construction project was ongoing across the road. The construction mainly involved vehicles transporting materials, roofing, and operation of construction equipment.

4.4 Results and discussion

In this section, first the trap penetration under various conditions was evaluated and a characteristic penetration curve was fitted upon it. Based on the curve, sensitivities with different trap voltages were calculated. After combining pairs of the calculated sensitivities and selecting the best combination, two candidate voltages were chosen. Secondly, the sensitivities with the two candidate voltages were measured and combined in a weighted sum (WS) style. Finally, the WS method was validated by comparing the aerosol GSA concentration simultaneously measured by WS and scanning mobility particle sizer spectrometer (SMPS) in both laboratory testing and field measurement.

4.4.1. Characterization of the trap and sensitivity estimation

The particle (singly charged) penetration rate through the trap is shown in Fig. 4-5 where 5 different voltages of the trap and 10 different particle sizes were analyzed. For each particle size, the penetration decreased with the increasing voltages, because the fact that increasing voltages corresponds with increasing electrostatic force on the particles

led to a heavier particle removal, namely, less penetration. However, for large particles (e.g. 300 nm), which have the lowest electrical mobility (Z_p) in the characterization measurements, electrostatic precipitation had a marginal effect on the particle penetration so that increasing voltage only slightly decreased the penetration. The electrical mobility of charged particles is defined as (Hinds, 1999):

$$Z_p = \frac{neC_c}{3\pi\eta d} \tag{8}$$

where n is number of elementary charges on the particle, e is elementary charge, C_c is Cunningham slip correction factor and $C_c=1 + Kn[\alpha + \beta\, exp(-\gamma/Kn)]$, α=1.142, β=0.558, γ=0.999 (Allen & Raabe, 1985), Kn is Knudsen number, and η is gas viscosity.

Furthermore, Forsyth et al. (1998) and Li et al. (2009) proved that the penetration rate of a specific electrostatic precipitator under a fixed flow rate was a function of the product (Z_p*V) of the particle electrical mobility (Z_p) and the applied voltage (V) of the electrostatic precipitator. In other words, particles with the similar electrical mobility had a comparable penetration. This conclusion agrees well with Fig. 4-5a where particles of 25 nm with 1000 V and 40 nm with 2400V holding an almost identical Z_p*V (3.69 and 3.58 cm^2/s) had a similar penetration, 0.208 and 0.212, respectively.

Therefore, we presented the penetration as a function of Z_p*V in Fig. 4-5b. The results for all voltages and sizes converged into one trend, which is consistent with Qi et al. (2009)'s. Li et al. (2009) used the same model of the trap as this study and fitted the

data to two different relationships for two Z_p*V regimes: a linear curve was best fitted for Z_p*V smaller than 1 cm^2/s and an exponential curve was best fitted for Z_p*V larger than 1 cm^2/s. In the same way, we fitted the results to the above two functions.

a

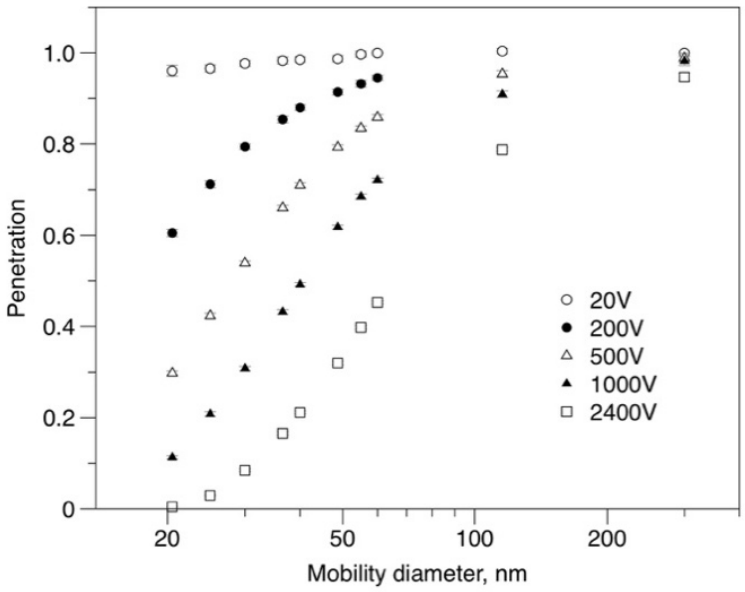

b

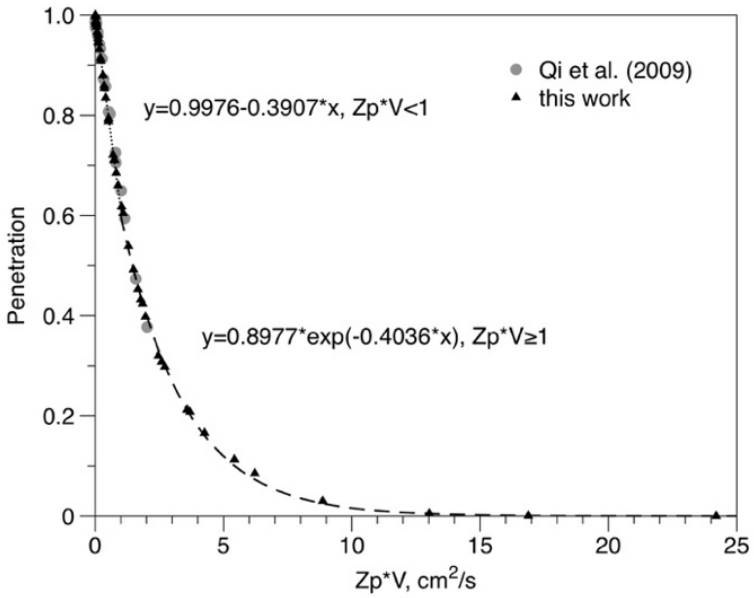

Fig. 4-5. (a) Penetration for singly charged particles with different trap voltages (b) penetration as a function of Z_p*V.

By means of the curves in Fig. 5b, the sensitivities with different voltages were estimated by Eq. 9 and shown in Fig. 4-6.

$$S_e(d,V) = \frac{I(V)}{N} \approx \frac{n_p(d)NP(Z_p,V)Qe}{N} = n_p(d)P\left(Z_p,V\right)Qe \tag{9-1}$$

$$\frac{S_e(d,V)}{S(d,20\text{ V})} = \frac{P(Z_p,V)}{P(Z_p,20\text{ V})} \tag{9-2}$$

therefore

$$S_e(d,V) = S(d,20\ V)\frac{P(Z_p,V)}{P(Z_p,20\text{ V})} \tag{9-3}$$

Where S_e is the estimated sensitivity, $n_p(d)$ is mean charge per particle for the charger at particle size d, P is the penetration that can be estimated by Fig. 5b, and Q is the

volumetric flow rate of the aerosol entering the mixing chamber of the charger. We assume $S(d, 20\ \mathrm{V})$ a known parameter because the fitting curve based on $S(d, 20\ \mathrm{V})$ between the lower and upper size limit serves as the performance curve for every charger and will be always measured beforehand as part of the charger calibration.

It is noted that $I(V) = n_p(d)NP(Z_p, V)Qe$ in Eq. 9-1 only works well for the ideal case where $n_p(d)$ and Z_p are rather monodisperse. Kaminski et al. (2012) proved that, in both experiments and numerical simulations, particles classified by DMA and charged by NSAM had a wide charge distribution, e.g., the 131 *nm* PSL particles carry from 1 to 8 elementary charges where the fraction of 4 charges is the highest and have a multimodal lognormal distribution of electrical mobility (Z_p) range from 5E-5 to 1.5E-3 cm^2/Vs (Fig. 3 in Kaminski et al., 2012). Therefore, in our calculation, both $n_p(d)$ and Z_p that we used for Eq. 9 were both average values, which may cause a discrepancy between measured and estimated sensitivities (section 4.2).

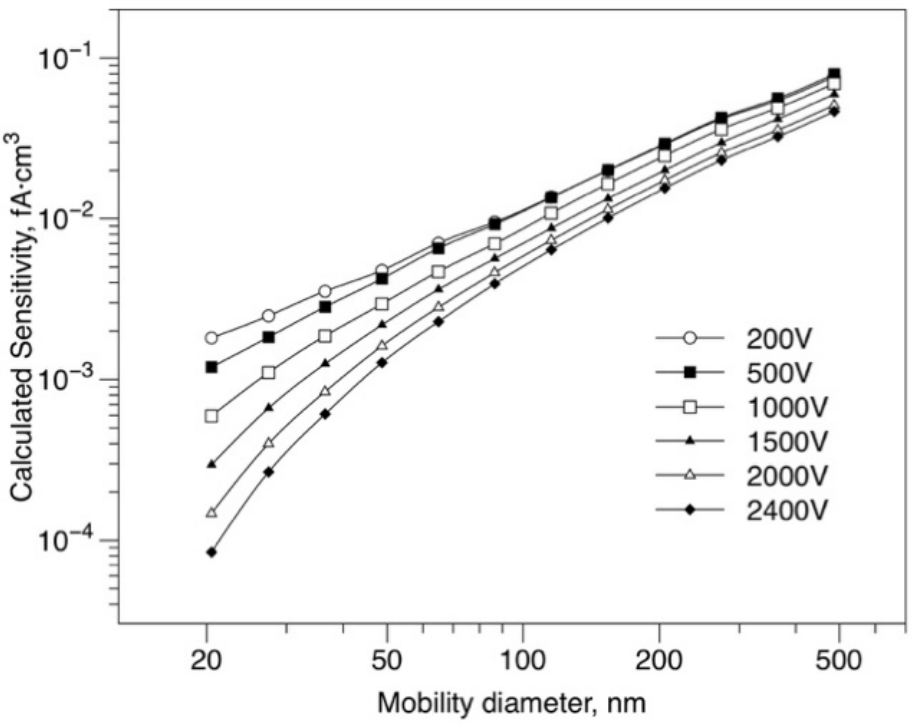

Fig. 4-6. Estimated sensitivities under different voltages using Eq. 9.

In Fig. 4-6, the slopes of the lines (from connecting data points for each voltage) mostly increased with increasing voltages. Although not all results perfectly followed a power law, if fitting into power laws, the power of the relationships increased with increasing voltages as well. Meanwhile, we found that the power at 2400 V was the closest one to 2.0 among the measured ones (although only in a limited size range) and therefore 2400 V was chosen as one of the candidate voltages (section 2.3); 20 V (as the default voltage to only remove excess ions) could serve well as another candidate voltage for the baseline sensitivity since it can cover the whole measuring range of NSAM.

4.4.2. Sensitivity measurement and weighted sum combination

In section 4.4.1, 20 and 2400 V were chosen as the candidate voltages. The sensitivities at these voltages were measured and shown in Fig. 7a. The error bars increased towards the smallest size in the 2400 V case because instrument noise began to significantly affect the electrical current there. Note that the sensitivity at 20 V is proportional to mean charge per particle: $n_p = S(d,\ 20\ \text{V})/(Qe)$; when fitting n_p to a power law as a function of particle diameter, the relationship was $n_p=0.0186d^{1.14}$, which agrees well with other researchers (section 4.2.1).

The measured sensitivities, $S(d,\ 2400\ \text{V})$ and $S(d,\ 20\ \text{V})$ in Fig. 4-7a, were used to conduct the WS combination. According to Eq. 4 and 5, two constants a and b in $d^2 = aS(d,\ 2400\ \text{V}) + bS(d,\ 20\ \text{V})$ that is a transformation of Eq. 5 were fitted using least square fitting and the results are: a=3.324E6, b= 1.302E5, and accordingly the weighting factor $c = a/b$ in Eq. 4 equals 13.52 with a coefficient of determination 0.9974; however, the fitting only performed satisfactorily below 300 and above 20 nm. Applying the weighting factor c into the WS combination in Eq. 4, we had the new WS sensitivity: $S_{WS}(d,\ V_1,\ V_2,\ c) = S(d,\ 20\ \text{V}) + cS(d,\ 2400\ \text{V})$. A power law with a power of 2.0 was fitted for the new WS sensitivity (20<d<300 nm) (Fig. 4-7b):

$$S_{WS}(d,\ V_1,\ V_2,\ c) = 4.47E\text{-}6\ d^{2.0}. \tag{10}$$

a

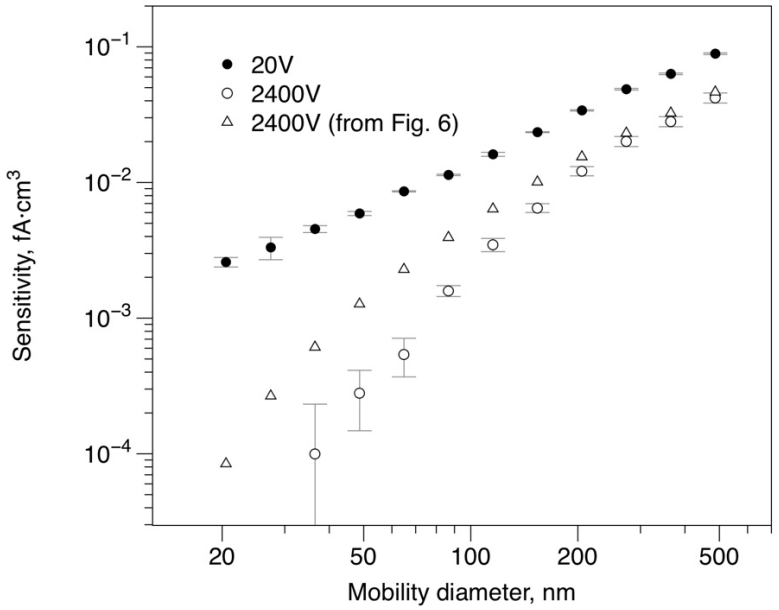

b

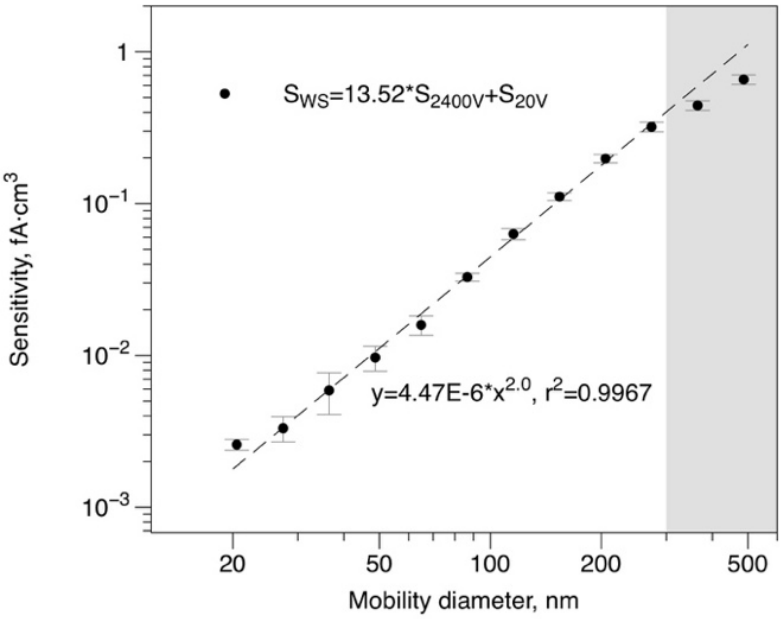

Fig. 4-7. (a) Measured sensitivities and (b) combined sensitivities with the power law fitting.

Due to Eq. 5 and 10, we determined k=0.703 $\mu m^2/(cm^3 fA)$ in Eq. 7, where I_c is in fA and GSA concentration is in $\mu m^2/cm^3$. With this simple form of Eq. 7, the GSA concentration for polydisperse aerosols can be easily measured without any data inversion.

Note that the sensitivities in Eq. 10 are higher than the measured ones when the diameters of the particles are larger than 300 nm (gray zone in Fig. 4-7b). In fact, the measured sensitivities were 74.5% and 62.1% of those calculated from Eq. 10 at 365.2 and 487 nm, respectively. Therefore, with the presence of particles larger than 300 nm, sensitivity predictions from Eq. 10 will have size-dependent overestimation. Consequently, the GSA concentration will be underestimated using Eq. 7 since Eq. 7 and 10 are inverse functions.

4.4.3. Laboratory validation measurement of the weighted sum method

Fig. 4-8a shows the comparison of the GSA concentrations measured by both WS and SMPS where the GSA from SMPS is the result of a calculation that relies on the spherical shape of the particles. In this test, we generated and analyzed five different aerosols whose geometric standard deviation (σ_g) and number concentration were between 1.52 to 1.95 and 1.2E+4 to 5.1E+5 #/cm^3, respectively. The concentration of each aerosol was varied by using different dilution ratio. In general, filled shapes represent aerosols in the working range (20-300 nm) and open shapes symbolize aerosols partially but still mainly in range. Fig. 4-8b shows both number and surface area concentrations of three exemplary distributions: DEHS in range, gold, KCl out of range

(gray zone represents the part of aerosol that is out of range) from left to right. The out of range part of the KCl is presented in the gray zone where the proportion of particles larger than 300 nm is 1.1% in number and 20.7% in GSA concentration. The aerosol generated from gold colloid had an apparent multimodal pattern where the left peak indicates the residual from the surfactant and the right peak represents 50 nm gold particles. Multimodal aerosols are extremely difficult cases and a great challenge for aerosol monitors, especially for those assuming (Fierz et al., 2002; Li et al., 2009; Marra et al., 2010) or only calibrated using unimodal aerosol (McMurry, 2000; Fierz et al., 2008). In Fig. 4-8a, for aerosols in range (even bimodal), the results all fell on the 1:1 line with a Pearson correlation coefficient of 0.9961 and the coefficient of variation for the ratio of GSA by WS to that by SMPS is 7.5%; for aerosols partially out of range, WS moderately underestimated the GSA concentration (65–77% of SMPS).

a

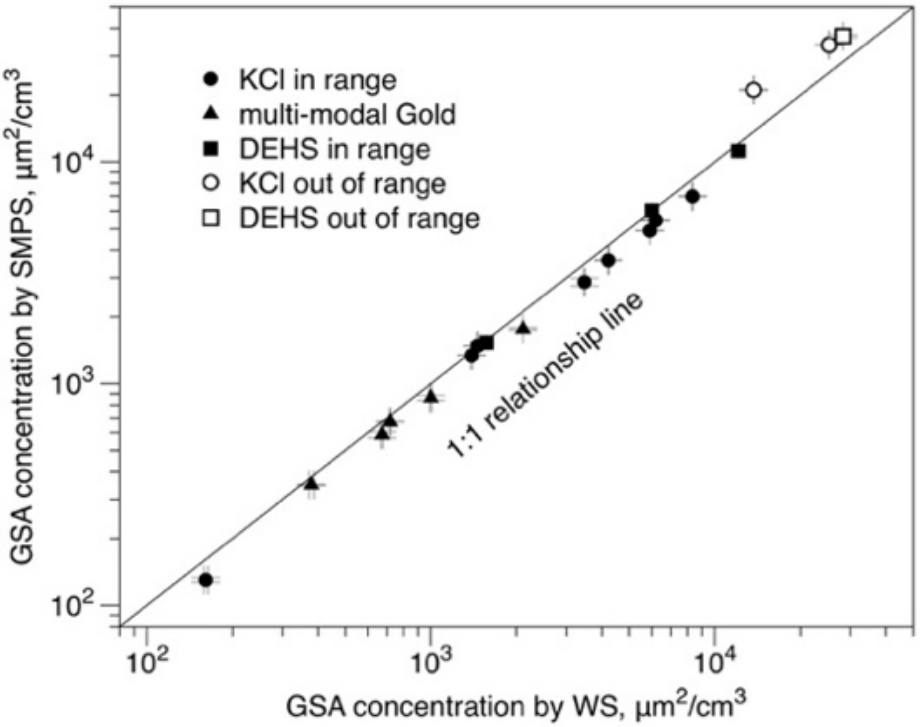
KCl in range
multi-modal Gold
DEHS in range
KCl out of range
DEHS out of range
1:1 relationship line
GSA concentration by SMPS, µm²/cm³
GSA concentration by WS, µm²/cm³
10²
10³
10⁴

b

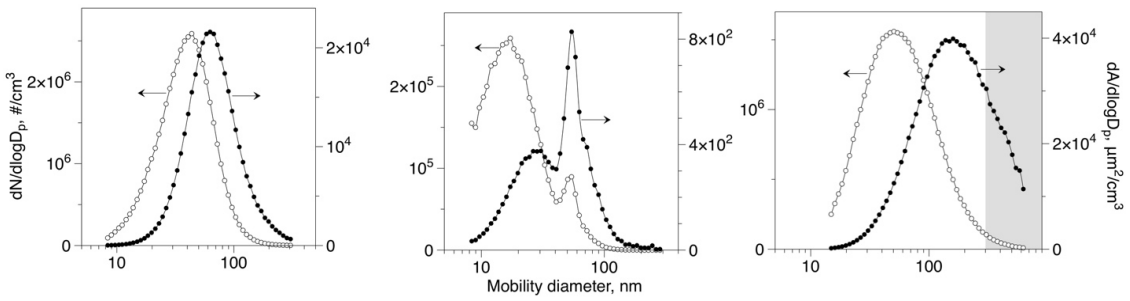

Fig. 4-8. (a) GSA concentration comparison between WS and SMPS (b) exemplary aerosol size distributions for both number (left y-axis) and surface area (right y-axis) concentrations: DEHS in range, gold, and KCl out of range from left to right.

During the GSA measurement, the lung-deposited surface area (LDSA) was also measured in several in-range cases (Fig. 4-9). The LDSA is defined as the total surface area of the aerosol deposited in the human lung where the deposition depends on the particle size as well as the deposition region of the lung (Hinds, 1999). In Fig. 4-9, the concentrations of LDSA for both TB and A regions (measured by NSAM) and GSA (measured by WS) were all normalized by the GSA concentration of each aerosol from SMPS. The normalized LDSA in TB and A regions were respectively in the range of 0.035–0.092 and 0.15–0.35.

The distributions of surface-area-concentration versus diameter were shown to the right of the Fig. 4-9 and aligned at 60 nm. The normalized LDSA for both regions increased with the decreasing modes of the aerosols, because, in the particle diameter range of 20–300 nm, the lung deposition rates for both regions increase with decreasing

particle size (ICRP, 1994). In other words, the ratio of the LDSA to GSA concentration strongly depends on the aerosol distribution. Therefore, without knowing the aerosol information (e.g., the mode and geometric standard deviation), the LDSA is inappropriate to represent other types of particle surface area.

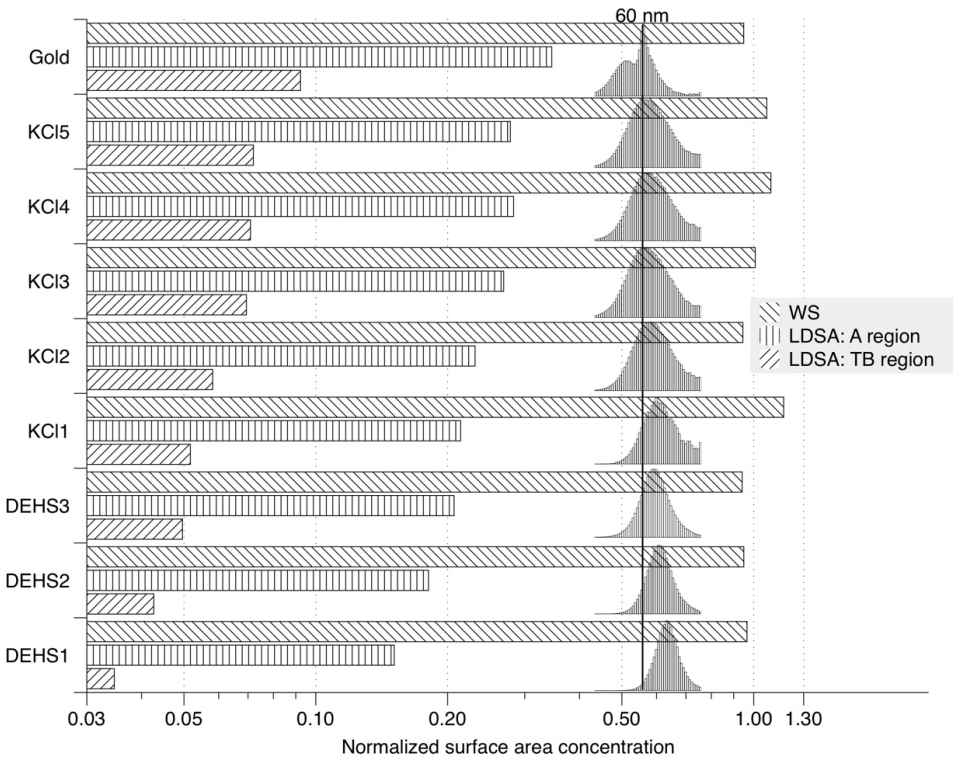

Fig. 4-9. Comparison of the normalized surface area concentrations. The average mode of all the distributions is 60 nm.

4.4.4. Field measurement

GSA concentrations in the field measurements by paralleled WS and SMPS were also compared. Fig. 4-10 shows the GSA concentration of the indoor measurement in the laboratory for 5 h. For the data presentation, SMPS used both 8 and 64 scanning size bins, which respectively represent the lowest and highest size resolution; however, only the highest resolution was used for the data analysis in the following discussion. With a Pearson correlation coefficient of 0.8302, WS agreed well with SMPS on the trend as well as the GSA concentration where the GSA concentrations during the whole measurement by both methods were mostly below 50 $\mu m^2/cm^3$. The indoor concentration was mostly stable because of no source of emission during the measurement except a random particle leak in the laboratory in a short period happened at around 14:15. Again, both methods captured this emission episode and agreed well with each other.

However, SMPS fluctuated much more violently than WS at the low GSA concentration, as can be seen in Fig. 10. In fact, the coefficient of variation of the GSA concentration during the entire sampling (excluding the emission episode) for SMPS was as large as 27%, whereas it was only 10% for WS; while the lowest current (4.8 *fA*) measured by WS was still more than two times of the detection limit of the electrometer (~2 *fA in Kaufman et al., 2002*), the particle number concentration is 900 $\#/cm^3$ in average and the raw count of CPC was as low as 1 $\#/cm^3$ for many size bins of SMPS. Consequently, since SMPS derives the GSA concentration from the integral of particle number concentration *N(d)* that could be miscounted and diameter square d^2 through the whole distribution, the miscounting on raw particle number on every size of particles, especially for large particles, may make a significant impact on the estimation of total

GSA concentration. For instance, 1#/cm^3 raw count of 532.8 nm particles, which may be miscounted, took 24% (after converting the raw count of CPC to the size distribution of SMPS) of the total GSA at 10:55.

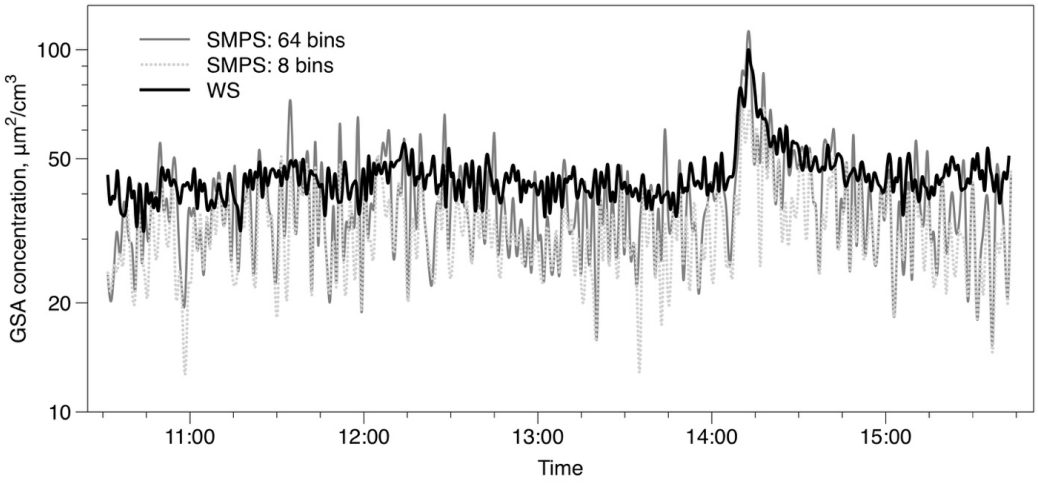

Fig. 4-10. GSA concentration of the indoor air in the laboratory.

Fig. 4-11 shows comparison results of the GSA concentration in the ambient air measurement. All results presented here are the average of data for every 5 min and the overall data showed a pronounced diurnal variation. A building construction happened on Monday (6:00–17:00) and concentrations in a large range (100–700 μm^2/cm^3) were detected. Other than the construction, we also experienced light and heavy rain (thunderstorm) on Monday and Tuesday (gray zone), respectively. As expected, during the rainy period, the concentration decreased dramatically; however, when the rain stopped, the concentration rose immediately.

The results of both methods were consistent with each other with a Pearson correlation coefficient of 0.9585, even though the results from WS were slightly higher (125% of SMPS). The fact that the difference in Fig. 4-11 is more apparent than that in Fig. 4-10 is not surprising because SMPS only measured particles in the range of 17.5-532.8 nm (depending on instrument setting) whereas WS had a wider sampling size range and measured almost everything it samples and, when sampling ambient air with the significant presence of large particles, WS encountered much more GSA concentration than SMPS. Although according to the calibration in section 4.2 WS underestimated the concentration of particles larger than 300 nm, the size-dependent underestimation still made a weaker impact than the wider sampling range of WS over SMPS so that WS measured a higher GSA concentration. It is noted that, during and after the heavy rain, WS agreed with SMPS much better than other periods because the raindrops scavenged the large particles, especially those larger than 1 μm (Slinn, 1984) and thus the effect of size-dependent underestimation and measuring range became marginal.

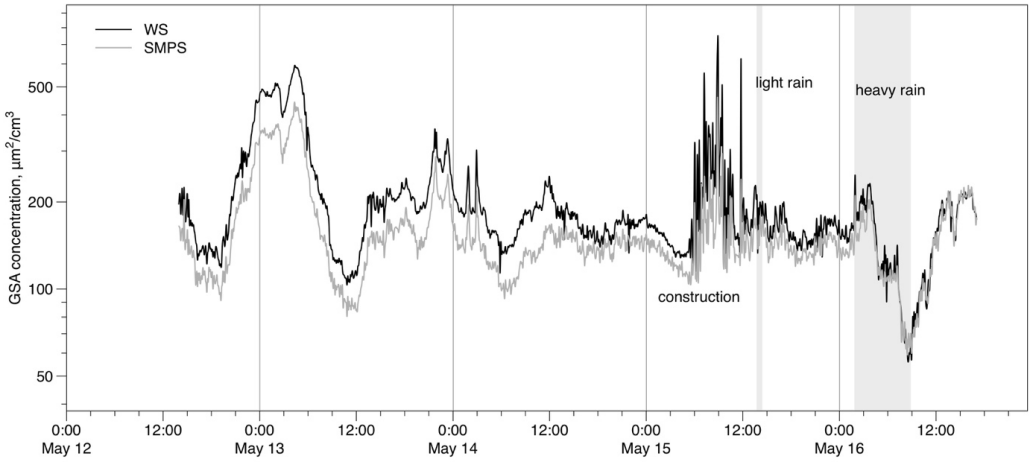

Fig. 4-11. GSA concentration of the continuous outdoor sampling.

4.4.5 Application of the WS method

More measurements were conducted by WS and SMPS in parallel to further prove that the WS method is suitable for real-time environmental measurement of aerosol GSA concentration. The measurements included events of laser printing in the computer laboratory, the candle burning in the general laboratory, different processes in the machine shop, and an outdoor sampling. The results are shown in Figs. 4-12, 4-13, 4-14, and 4-15, respectively. All figures are presented in a concentration-time fashion. Error bars in gray are shown for the WS measurements. In general, both methods agree well each other on the trend as well as the GSA concentrations that are high in emission episodes or low for background noise. When the concentration changed rapidly relative to the sampling time required for WS getting a data point that is 5 s, the measured concentrations had large uncertainty that can be found in nearly all the figures in this section. That is the same case for SMPS and can be checked in the scanned aerosol distributions although not shown in the figures.

Fig. 4-12a shows the GSA concentration over time in the measurement of laser printing. Total 4 printings (A, B, C, D) were conducted during the measurement. Black plaintexts were printed in A, handouts in color were printed in B, pictures in color were

printed C, and pictures in red were printed in D. It was found that printing pictures in color generated more emission than plaintexts with respect to GSA concentration. This finding was consistent with the aerosol distributions shown in Fig. 4-12b. Printing pages in color generated larger particle (peak size at around 70 nm other than the background) than printing plaintexts (peak size at around 30 nm), which leads to a higher GSA concentration. When printing plaintexts, the particle size and concentration were close to the background.

a

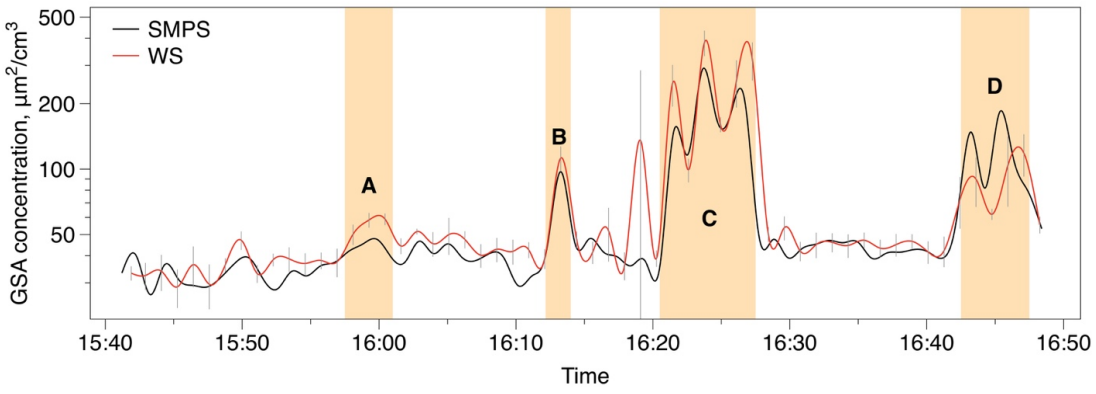

b

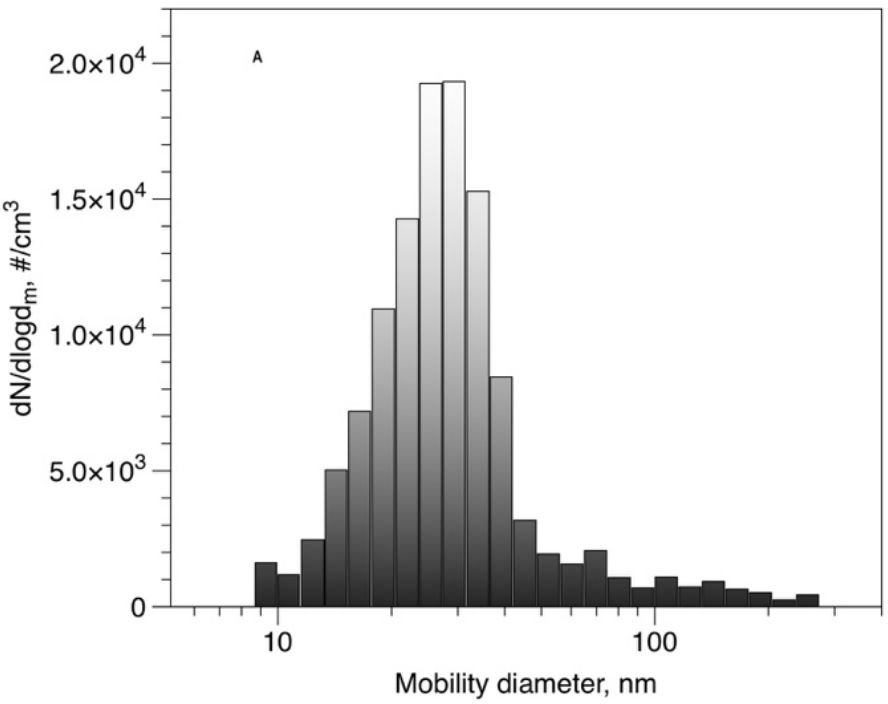
A
2.0×10^4
1.5×10^4
1.0×10^4
5.0×10^3
0
dN/dlogd_m, #/cm^3
10
100
Mobility diameter, nm

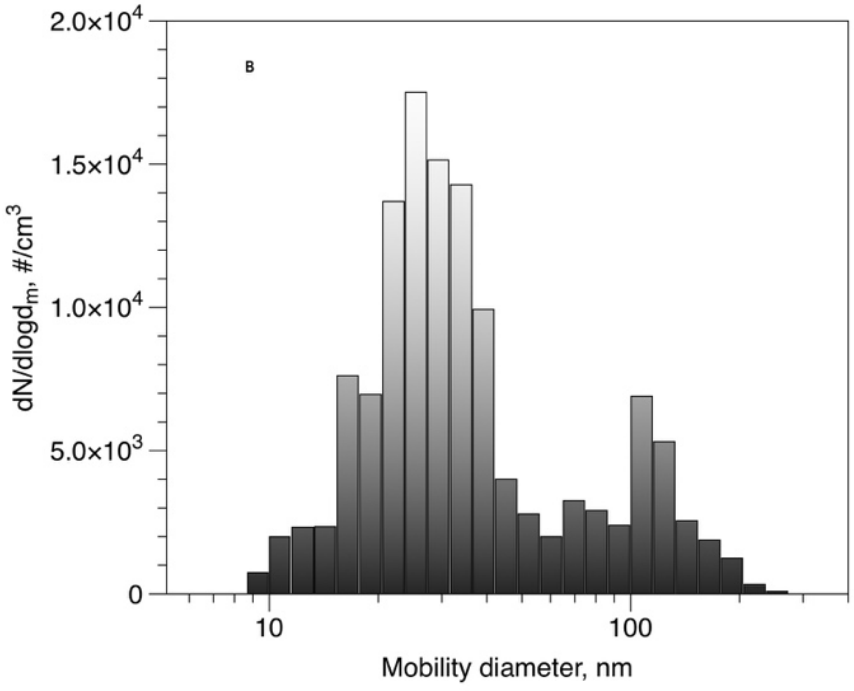
B
2.0×10^4
1.5×10^4
1.0×10^4
5.0×10^3
0
dN/dlogd_m, #/cm^3
10
100
Mobility diameter, nm

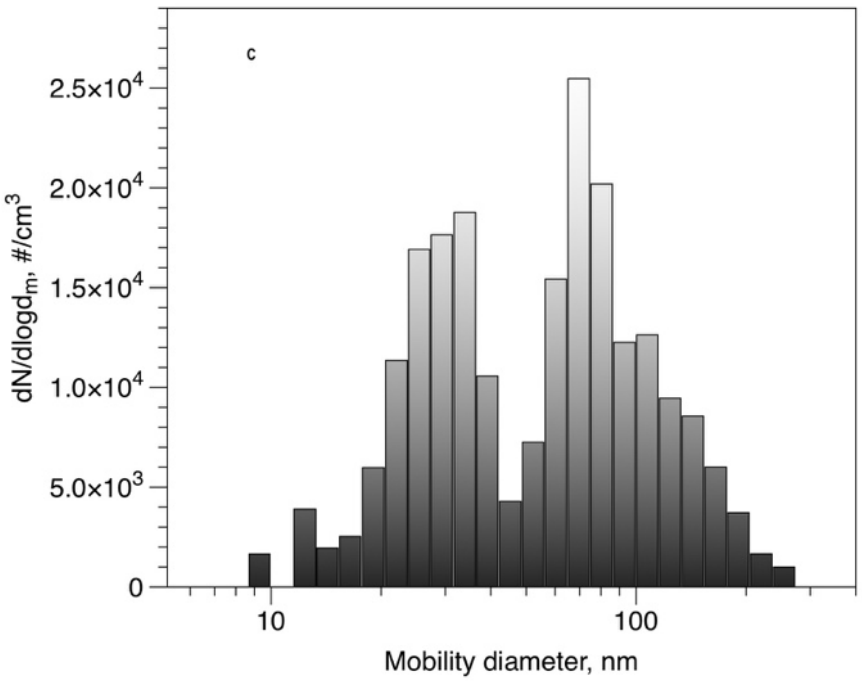
c
2.5×10^4
2.0×10^4
1.5×10^4
1.0×10^4
5.0×10^3
0
dN/dlogd_m, #/cm^3
10
100
Mobility diameter, nm

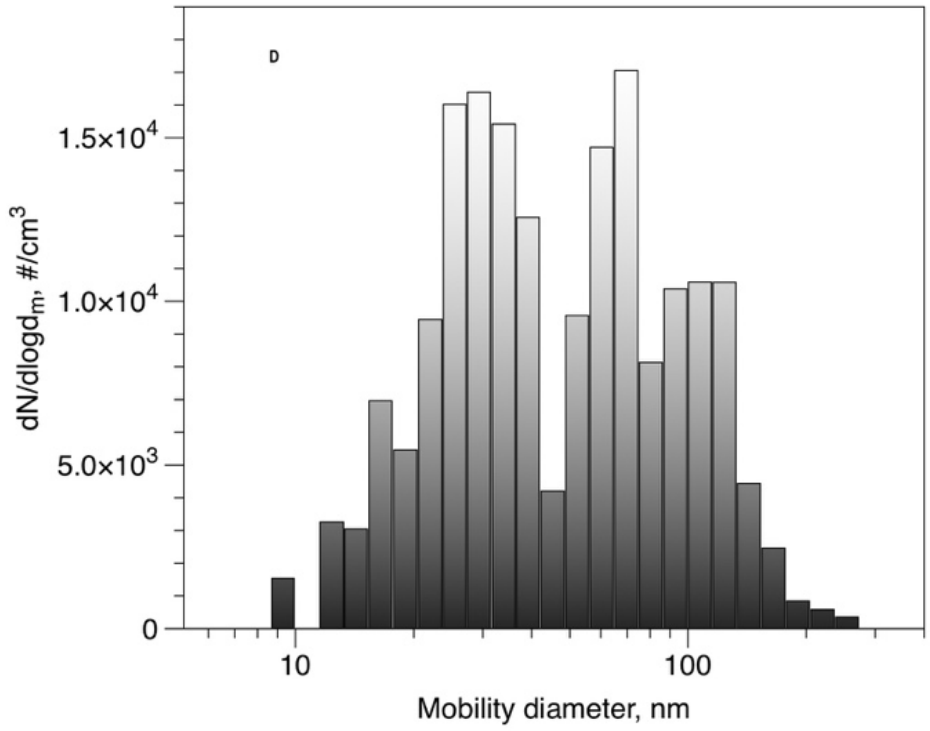
D
1.5×10^4
1.0×10^4
5.0×10^3
0
dN/dlogd_m, #/cm^3
10
100
Mobility diameter, nm

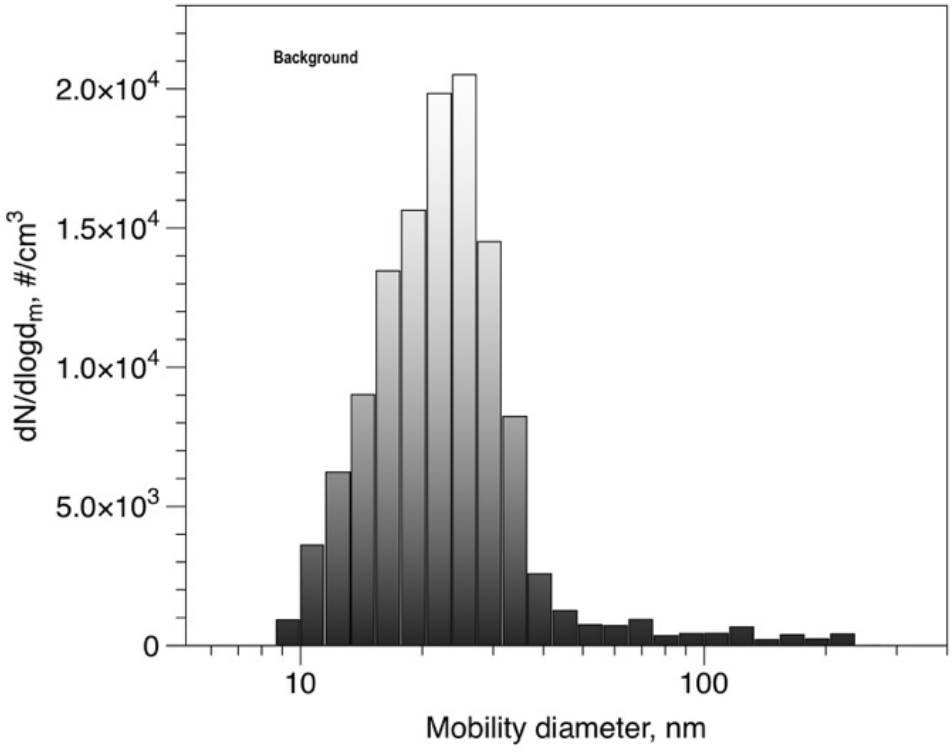
Background
2.0×10^4
1.5×10^4
1.0×10^4
5.0×10^3
0
dN/dlogd_m, #/cm^3
10
100
Mobility diameter, nm

Fig. 4-12. a) GSA concentration from the laser printer b) aerosol size distributions for the printing background and events A, B, C, and D, respectively.

Fig. 4-13. shows particle GSA concentration during the candle burning. The burning started at 11:20 and stopped at 11:37. Both methods agreed well on almost every emission peak and the concentration trend of the aerosol.

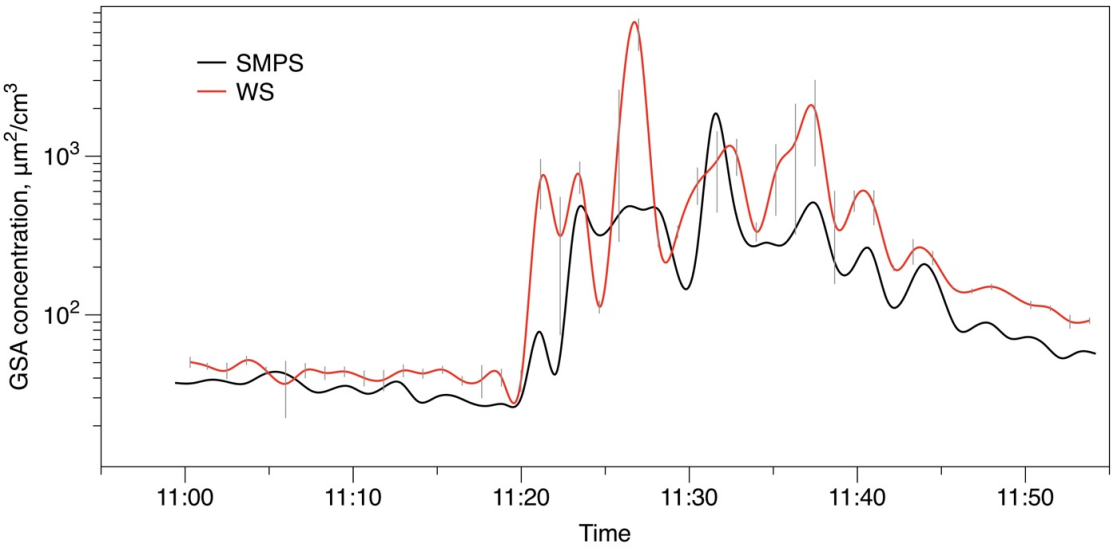

Fig. 4-13. GSA concentration from the burning candle.

In Fig. 4-14, GSA concentration with time were measured in the machine shop in a chronological sequence. From left to right of Fig. 4-14 were the measurements of waterjet cutting, post-welding, sanding, and welding with local exhaust ventilation (LEV). For the last measurement, the welding stopped for a period (15:00-15:30).

Because different processes happened in different locations of the machine shop, background concentrations were different.

The periods of waterjet cutting and sanding were much shorter compared with the welding. Although the periods were short, obvious peaks were observed. For the cases of waterjet cutting, after welding, and sanding, WS and SMPS captured the peak and agreed well with each other on the GSA trend and concentration. However, for the welding case, the discrepancy between WS and SMPS was significant, although both methods agreed well with each other on the trend and correctly captured every peak.

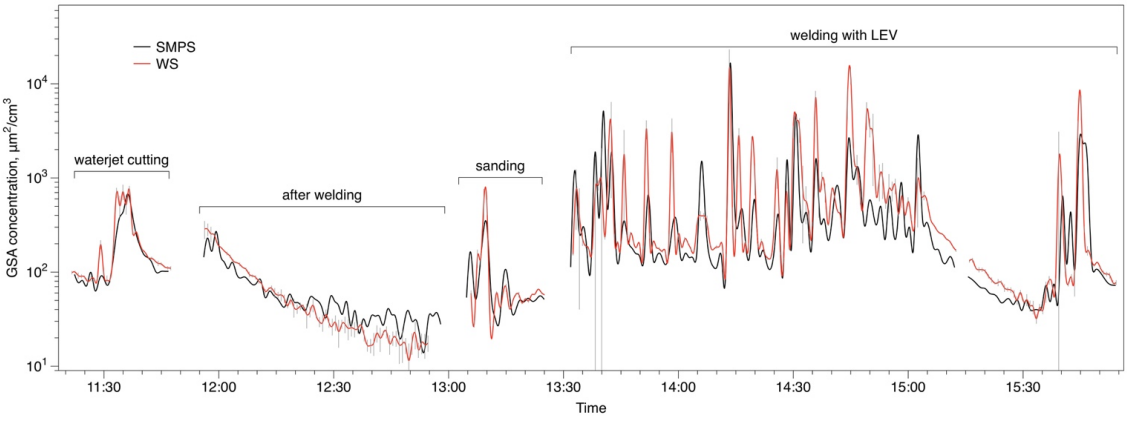

Fig. 4-14. GSA concentration in the machine shop.

The outdoor GSA concentration was also monitored (Fig. 4-15), because the number concentration was very low and changed slowly in this six-hour sampling, SMPS fluctuated more severe than WS that was discussed in the last section. Other than the

fluctuation, SMPS agreed well with WS on both the trend and magnitude of the concentration.

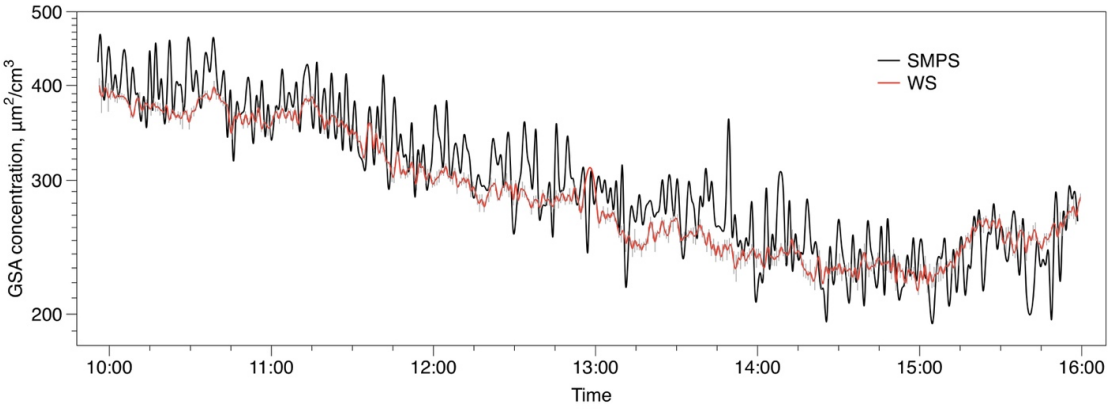

Fig. 4-15. GSA concentration of the outdoor environment.

When interpolating the data, the correlation of results can be studied. The data include candle burning, laser printer, outdoor, welding with LEV, waterjet cutting, and sanding in the machine shop.

Although the concentrations covered several decades from 20 to 10^4 $\mu m^2/cm^3$, that can be observed from previous figures, the results all fall to 1:1 line except the case of welding with extremely transient emission. As discussed previously, for transient emission, the results may not correctly represent the real concentration.

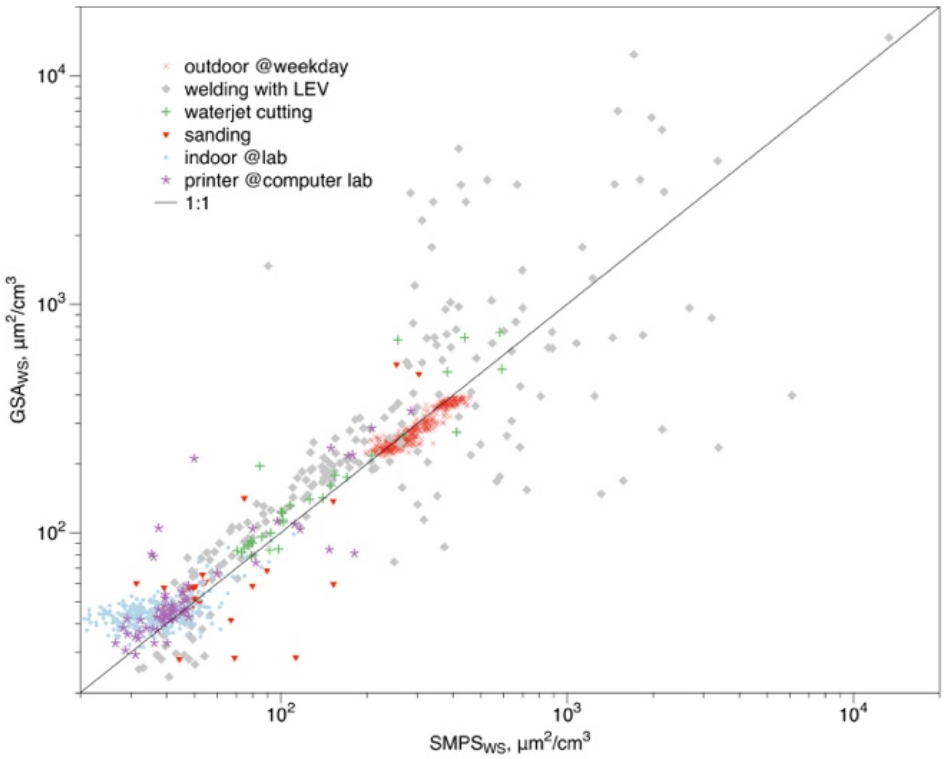

Fig. 4-16. Correlation of GSA concentration between WS and SMPS.

4.4.6. Limitations and universal feasibility of the WS method

Some limitations are worth noting for the WS method: first, the method was merely calibrated using spherical particles. Therefore, whether the method or a modified one based on this method is capable of measuring arbitrarily shaped particles is unclear and more investigations need to be carried out. Furthermore, the fact that WS and SMPS assume spherical particles may cause uncertainty when conducting field measurements (section 4.4) due to the various morphologies of particles in the environment. Shin et al., 2010 stated that ratio of the GSA of loose agglomerates (numerically described in Lall & Friedlander, 2006) to spherical particles at the same mobility diameter decreases with an

increasing mobility diameter, e.g. the ratio is from around 100–70% in the mobility diameter from 70 to 200 nm. Secondly, when aerosols were out of working range, the WS method had the size-dependent underestimation.

On the other hand, the WS method showed great improvement with regards to GSAM in the author's earlier study (Cao et al., 2017) where an extra electrostatic precipitator was used and the GSA measurement needs to be divided into two separate regimes: 20–100 nm and 100–300 nm by an inertial impactor that may cause pressure-drop problem. By applying the WS method, the measuring range was improved greatly, the pressure-drop problem was eliminated, and the operation of the instrument was simplified significantly (automated by LabVIEW 15).

Another concern is that the WS method was only developed based on and validated for the presented unipolar charger and thus was tailored to this one. However, because of the similarity of the power-law charging status from different unipolar diffusion chargers, we assume that the WS method is universally viable for other diffusion chargers (including portable ones) with device-specific characterization and WS weighting factor. To prove this assumption, more analysis should be carried out in the future. Furthermore, the numerical concept of weighted sum combining instrument signals could possibly be extended to other research fields and measurement devices to create unprecedented measurements based on conventional techniques.

4.5 Conclusion

Prior work has documented several methods to measure particle surface area from offline to quasi-real time; SMPS, for example, can derive geometric surface area (GSA) concentration from the particle number concentration over size distribution in minutes. However, an appropriate approach and real-time monitor of the GSA measurement is missing and needed. In this study, we developed the novel weighted sum (WS) method to real-time measure the aerosol GSA concentration.

The principle of the WS method is to linearly combine the electrical currents that are from NSAM with two carefully selected trap voltages and correlate the resulted current with the aerosol GSA concentration. To validate the WS method, we present its results and comparisons with SMPS data in both laboratory testing and field measurement. For the laboratory testing, 16 polydisperse aerosols were challenged by both methods and the two results agreed well with a Pearson correlation coefficient of 0.9961; for the indoor and outdoor field measurements, WS and SMPS agreed well with each other as well with a Pearson correlation coefficient of 0.8302 and 0.9585, respectively. In addition, WS is more stable at the low concentration situation and suitable for outdoor environmental measurements. Most notably, this is the first method and instrument to our knowledge to real-time deliver aerosol GSA concentration with such a wide working range.

To validate the WS method, we present its results from it and comparisons with SMPS data in both laboratory testing and field measurement. For the laboratory testing, 16 polydisperse even multimodal aerosols were challenged by both methods and the two

results agreed well with a Pearson correlation coefficient of 0.9961; for the field measurement, WS and SMPS fitted well with each other as well. In addition, WS is more stable to the low concentration situation and suitable for outdoor environmental measurements. Most notably, this is the first method and instrument to real-time deliver aerosol GSA concentration with such a wide working range.

Chapter 5: Accomplishments and recommendations

5.1 Summary of accomplishments

The ultimate objective of the thesis is to develop an appropriate method to measure the geometric surface area concentration of aerosols in real-time. In the previous study, the unipolar diffusion charging is the most promising method to offer real-time measurement with respect to the geometric surface area measurement. Therefore, this study developed a numerical weighted sum method of combining responses of the electrical sensor to achieve aerosol geometric surface area measurement and validated the method by challenging it with both synthetic and environmental aerosols.

Chapter 2 described the development of a discretization method to model the capacitance of arbitrarily shaped particles such as 3D random agglomerates and aggregates. It was found that elementary charges were mainly distributed in the periphery of particles. From the obtained capacitance, the mean charge per particle in the continuum regime of charging that was modeled agreed well with previous experimental results, which further validates the modelling. In addition, with the discretization method,

the evolution of the capacitance and mean charge for agglomerates undergoing sintering was investigated for the first time.

Chapter 3 described the development of a system (GSAM version I) that can quickly deliver the GSA concentration of particles in a wide particle size range, i.e., 16-300 nm. The approach combines the inertial impaction, unipolar charging, electrostatic precipitation, and current measurement in which all the devices were well calibrated. Based on different assumptions of the particle size range, GSAM applies to both spherical and DLCA-like agglomerate particles with different calibration curves.

Chapter 4 described the development of the novel weighted sum (WS) method to measure the aerosol GSA concentration (GSAM version II) in real-time. The principle of the WS method is to linearly combine the electrical currents so that the resulted current correlated well with the aerosol GSA concentration. The WS method was validated by comparing its results with SMPS data in both laboratory testing and field measurement with a good agreement. With this technique, the working range of the instrument is much wider and the measurements are much more simplified than the author's earlier study (Cao et al., 2017). In addition, because of no hardware change to the commercialized NSAM, the method is friendly to researchers with their own NSAM. In addition, WS is more sensitive to the low concentration situation and suitable for outdoor environmental measurements. Most notably, this is the first appropriate method and instrument to real-time deliver aerosol GSA concentration with such a wide working range.

5.2 Recommendations

This is the first appropriate method to measure aerosol geometric surface area in real-time. More work can be conducted to improve the method.

1. The GSAM using the weighted sum method was calibrated using spherical particles. A specific calibration and setting can be done for other specific shapes of particles, e.g., diesel or carbon nanotubes, and thus the GSAM can be easily switched to the specific mode when the aerosol information is known.
2. The particle morphology is valuable information for GSAM as well as many other instruments; however, it is difficult to determine. In other words, a real-time method for particle morphology determination is lacking. The unipolar charging and electrostatic precipitation have the potential to determine the particle morphology and can be good candidates. However, a systematic and comprehensive approach is needed and tests on the particles in various shapes should be carried out to validate the method.

In addition to the improvement of the method/instrument, it can be also applied and generalized to facilitate the real-time measurement.

3. The concept of combining instrument responses in a weighted sum fashion is not limited to the GSA measurement and other properties (e.g., particle mass) can be also tested; the concept can possibly be extended to other processes (other than charging),

devices and fields to create unprecedented measurements based on conventional techniques.

4. There are many commercialized portable electrical sensors using unipolar diffusion charging. A portable version of GSAM can be also developed based on the commercialized sensors. Therefore, the geometric surface area measurement becomes viable for the mobile and workplace exposure measurements where internet of things (IOT) and big data become prevalent.
5. More evidence indicates that the adverse health effect of nanoparticles correlates more with particle geometric surface area than number and mass. However, the geometric surface area measurements for real-world environments are scarce and very limited conclusion about the correlation can be drawn, due to the lack of methods. Luckily, more comprehensive measurements using the GSAM can be conducted in the future, such as in the occupational and non-occupational environments, data that health research can rely on can be obtained. Moreover, regulations will be issued by the government with the support of real-world data.

Bibliography

Akhtar, M. K., Lipscomb, G. G., & Pratsinis, S. E. (1994). Monte-carlo simulation of particle coagulation and sintering. Aerosol Science and Technology, 21(1), 83-93. doi:10.1080/02786829408959698

Allen, M. D., & Raabe, O. G. (1985). Slip correction measurements of spherical solid aerosol particles in an improved Millikan apparatus. Aerosol Science and Technology, 4(3), 269-286. doi: 10.1080/02786828508959055

Asbach, C., Fissan, H., Kaminski, H., Kuhlbusch, T., Pui, D., Shin, H., Horn, H.G., & Hase, T. (2011). A low pressure drop preseparator for elimination of particles larger than 450 nm. Aerosol and Air Quality Research, 11(5), 487-496.

Asbach, C., Kaminski, H., Lamboy, Y., Schneiderwind, U., Fierz, M., & Todea, A. M. (2016). Silicone sampling tubes can cause drastic artifacts in measurements with aerosol instrumentation based on unipolar diffusion charging. Aerosol Science and Technology, 50(12), 1375-1384. doi: 10.1080/02786826.2016.1241858

Botet, R., Jullien, R., & Kolb, M. (1984). Hierarchical model for irreversible kinetic cluster formation. Journal of Physics A: Mathematical and General, 17(2), L75-L79. doi:10.1088/0305-4470/17/2/009

Brown, R. C., & Hemingway, M. A. (1995). Electric charge distribution and capacitance of agglomerates of spherical particles: Theory and experimental simulation. Journal of Aerosol Science, 26(8), 1197-1206. doi:10.1016/0021-8502(95)00524-2

Brunauer, S., Emmett, P. H., & Teller, E. (1938). Adsorption of gases in multimolecular layers. Journal of the American Chemical Society, 60(2), 309-319.

Cao, L. N. Y., Wang, J., Fissan, H., Pratsinis, S. E., Eggersdorfer, M. L., & Pui, D. Y. H. (2015). The capacitance and charge of agglomerated nanoparticles during sintering. Journal of Aerosol Science, 83(0), 1-11. doi: http://dx.doi.org/10.1016/j.jaerosci.2015.01.002

Cao, L. N. Y., Chen, S.-C., Fissan, H., Asbach, C., & Pui, D. Y. H. (2017). Development of a geometric surface area monitor (GSAM) for aerosol nanoparticles. Journal of Aerosol Science, 114, 118-129. doi: https://doi.org/10.1016/j.jaerosci.2017.09.013

Cao, L. N. Y., & Pui, D. Y. H. (2018). A novel weighted sum method to measure particle geometric surface area in real-time. *Journal of Aerosol Science*, 117, 11-23. doi:https://doi.org/10.1016/j.jaerosci.2017.12.007

Chang, J. S. (1981). Theory of diffusion charging of arbitrarily shaped conductive aerosol-particles by unipolar ions. Journal of Aerosol Science, 12(1), 19-26. doi:10.1016/0021-8502(81)90006-9

Eggersdorfer, M. L., Kadau, D., Herrmann, H. J., & Pratsinis, S. E. (2011). Multiparticle Sintering Dynamics: From Fractal-Like Aggregates to Compact Structures. Langmuir, 27(10), 6358-6367. doi: 10.1021/la200546g

Eggersdorfer, M. L., Kadau, D., Herrmann, H. J., & Pratsinis, S. E. (2012). Aggregate morphology evolution by sintering: Number and diameter of primary particles. Journal of Aerosol Science, 46, 7-19. doi: http://dx.doi.org/10.1016/j.jaerosci.2011.11.005

Fierz, M., Scherrer, L., & Burtscher, H. (2002). Real-time measurement of aerosol size distributions with an electrical diffusion battery. Journal of Aerosol Science, 33(7), 1049-1060.

Fierz, M., Burtscher, H., Steigmeier, P., & Kasper, M. (2008). Field measurement of

particle size and number concentration with the Diffusion Size Classifier (DiSC): SAE Technical Paper.

Fierz, M., Houle, C., Steigmeier, P., & Burtscher, H. (2011). Design, calibration, and field performance of a miniature diffusion size classifier. Aerosol Science and Technology, 45(1), 1-10.

Fierz, M., Meier, D., Steigmeier, P., & Burtscher, H. (2013). Aerosol Measurement by Induced Currents. Aerosol Science and Technology, 48(4), 350-357. doi: 10.1080/02786826.2013.875981

Filippov, A. V. (1994). Charge distribution among non-spherical particles in a bipolar ion environment. Journal of Aerosol Science, 25, 611–615. doi:10.1016/0021-8502(94)90002-7

Fissan, H., Neumann, S., Trampe, A., Pui, D. Y. H., & Shin, W. G. (2007). Rationale and principle of an instrument measuring lung deposited nanoparticle surface area. Journal of Nanoparticle Research, 9(1), 53-59. doi: 10.1007/s11051-006-9156-8

Fissan, H., Asbach, C., Kaminski, H., & Kuhlbusch, T. A. J. (2012). Total surface area concentration measurements of nanoparticles in gases with an electrical

sensor. Chemie Ingenieur Technik, 84(3), 365-372.

Forsyth, B., Liu, B. Y. H., & Romay, F. J. (1998). Particle charge distribution measurement for commonly generated laboratory aerosols. Aerosol Science and Technology, 28(6), 489-501. doi: 10.1080/02786829808965540

Fuchs, N. A. (1963). On the stationary charge distribution on aerosol particles in a bipolar ionic atmosphere. Geofisica pura e applicata, 56(1), 185-193. doi: 10.1007/BF01993343.

Gentry, J. W. (1972). Charging of aerosol by unipolar diffusion of ions. Journal of Aerosol Science, 3, 65–76. doi:10.1016/0021-8502(72)90142-5

Gopalakrishnan, R., Thajudeen, T., Ouyang, H., & Hogan, C.J. (2013). The unipolar diffusion charging of arbitrary shaped aerosol particles. Journal of Aerosol Science, 64, 60-80. doi: 10.1016/j.jaerosci.2013.06.002

Greason, W.D. (1992). Electrostatic discharge in electronics. Research Studies Press. p. 48. ISBN 978-0-86380-136-5.

Hagendorfer, H., Lorenz, C., Kaegi, R., Sinnet, B., Gehrig, R., Goetz, N. V., . . . Ulrich, A. (2010). Size-fractionated characterization and quantification of

nanoparticle release rates from a consumer spray product containing engineered nanoparticles. Journal of Nanoparticle Research, 12(7), 2481-2494. doi:10.1007/s11051-009-9816-6

Hinds, W. C. (1999). Aerosol technology: properties, behavior, and measurement of airborne particles. Wiley-Interscience, New York.

Hogan, C. J., & Biswas, P. (2008). Porous film deposition by electrohydrodynamic atomization of nanoparticle sols. Aerosol Science and Technology, 42(1), 75-85. doi:10.1080/02786820701787951

Hood, E. (2004). Nanotechnology: looking as we leap. Environmental Health Perspectives, 112(13), A740-A749.

ICRP. (1994). Human respiratory tract model for radiological protection. Annals of the ICRP, 24(1-3).

Järvinen, A., Kuuluvainen, H., Niemi, J. V., Saari, S., Dal Maso, M., Pirjola, L., . . . Rönkkö, T. (2015). Monitoring urban air quality with a diffusion charger based electrical particle sensor. Urban Climate, 14, Part 3, 441-456. doi: http://dx.doi.org/10.1016/j.uclim.2014.10.002

Jung, H. J., & Kittelson, D. B. (2005). Characterization of aerosol surface instruments in transition regime. Aerosol Science and Technology, 39(9), 902-911. doi: 10.1080/02786820500295701

Kaminski, H., Kuhlbusch, T. A. J., Fissan, H., Ravi, L., Horn, H.-G., Han, H.-S., & Asbach, C. (2012). Mathematical description of experimentally determined charge distributions of a unipolar diffusion charger. Aerosol Science and Technology, 46(6), 708-716. doi: 10.1080/02786826.2012.659360

Kammler, H. K., Jossen, R., Morrison, P. W., Pratsinis, S. E., & Beaucage, G. (2003). The effect of external electric fields during flame synthesis of titania. Powder Technology, 135, 310-320. doi:10.1016/j.powtec.2003.08.023

Kaufman S.L., Medved A., Pöcher A., Hill N., Caldow R., and Quant F.R. 2002. An electrical aerosol detector based on the corona-jet charger. Twenty-First AAAR conference, October 7–11, Paper no. P12-07, Charlotte, NC.

Kim, S. C., Wang, J., Emery, M. S., Shin, W. G., Mulholland, G. W., & Pui, D. Y. H. (2009). Structural property effect of nanoparticle agglomerates on particle penetration through fibrous filter. Aerosol Science and Technology, 43(4), 344-355.

Kirsch, A. A., & Zagnit'ko, A. V. (1981). Diffusion charging of submicrometer aerosol particles by unipolar ions. Journal of Colloid and Interface Science, 80, 111–117. doi:10.1016/0021-9797(81)90165-X

Knutson, E. O., & Whitby, K. T. (1975). Aerosol classification by electric mobility: apparatus, theory, and applications. Journal of Aerosol Science, 6(6), 443-451. doi:http://dx.doi.org/10.1016/0021-8502(75)90060-9

Ku, B. K., & Maynard, A. D. (2005). Comparing aerosol surface-area measurements of monodisperse ultrafine silver agglomerates by mobility analysis, transmission electron microscopy and diffusion charging. Journal of Aerosol Science, 36(9), 1108-1124. doi: 10.1016/j.jaerosci.2004.12.003

Laframboise, J. G., & Chang, J. (1977). Theory of charge deposition on charged aerosol particles of arbitrary shape. Journal of Aerosol Science, 8, 331–338. doi:10.1016/0021-8502(77)90020-9

Lall, A. A., & Friedlander, S. K. (2006). On-line measurement of ultrafine aggregate surface area and volume distributions by electrical mobility analysis: 1. Theoretical analysis. Journal of Aerosol Science, 37(3), 260-271. doi:10.1016/j.jaerosci.2005.05.021

Lebouf, R. F., Stefaniak, A. B., Chen, B. T., Frazer, D. G., & Virji, M. A. (2011). Measurement of airborne nanoparticle surface area using a filter-based gas adsorption method for inhalation toxicology experiments. Nanotoxicology, 5(4), 687-699. doi: 10.3109/17435390.2010.546951

Li, L., Chen, D.R., & Tsai, P.J. (2009a). Use of an electrical aerosol detector (EAD) for nanoparticle size distribution measurement. Journal of Nanoparticle Research, 11(1), 111-120. doi: 10.1007/s11051-008-9418-8

Li, L., Chen, D. R., & Tsai, P. J. (2009b). Evaluation of an electrical aerosol detector (EAD) for the aerosol integral parameter measurement. Journal of Electrostatics, 67(5), 765-773. doi: 10.1016/j.elstat.2009.05.001

Marra, J., Voetz, M., & Kiesling, H.-J. (2010). Monitor for detecting and assessing exposure to airborne nanoparticles. Journal of Nanoparticle Research, 12(1), 21-37. doi:10.1007/s11051-009-9695-x

McMurry, P. H. (2000). A review of atmospheric aerosol measurements. Atmospheric Environment, 34(12), 1959-1999. doi: http://dx.doi.org/10.1016/S1352-2310(99)00455-0

Oberdörster, G. (2000). Pulmonary effects of inhaled ultrafine particles. International

Archives of Occupational and Environmental Health, 74(1), 1-8.

Oberdörster, G., Maynard, A., Donaldson, K., Castranova, V., Fitzpatrick, J., Ausman, K., . . . Yang, H. (2005). Principles for characterizing the potential human health effects from exposure to nanomaterials: elements of a screening strategy. Particle and Fibre Toxicology, 2(1), 8. doi: 10.1186/1743-8977-2-8

Oh, H., Park, H., & Kim, S. (2004). Effects of particle shape on the unipolar diffusion charging of nonspherical particles. Aerosol Science and Technology, 38(11), 1045-1053. doi: 10.1080/027868290883324

Pandis, S. N., Baltensperger, U., Wolfenbarger, J. K., & Seinfeld, J. H. (1991). INVERSION OF AEROSOL DATA FROM THE EPIPHANIOMETER. Journal of Aerosol Science, 22(4), 417-428. doi: 10.1016/0021-8502(91)90002-y

Pratsinis, S. E. (1998). Flame aerosol synthesis of ceramic powders. Progress in Energy and Combustion Science, 24(3), 197-219. doi: 10.1016/s0360-1285(97)00028-2

Preining, O. (1998). The physical nature of very, very small particles and its impact on their behaviour. Journal of Aerosol Science, 29(5), 481-495. doi:https://doi.org/10.1016/S0021-8502(97)10046-5

Liu, B. Y. H., & Pui, D. Y. H. (1977). On unipolar diffusion charging of aerosols in the continuum regime. Journal of Colloid and Interface Science, 58(1), 142-149. doi:http://dx.doi.org/10.1016/0021-9797(77)90377-0

Pui, D. Y.H., Fruin, S., & McMurry, P. H. (1988). Unipolar diffusion charging of ultrafine aerosols. Aerosol Science and Technology, 8, 173–187. doi:10.1080/02786828808959180

Qi, C., Asbach, C., Shin, W. G., Fissan, H., & Pui, D. Y. H. (2009). The effect of particle pre-existing charge on unipolar charging and its implication on electrical aerosol measurements. Aerosol Science and Technology, 43(3), 232-240. doi: 10.1080/02786820802587912

Ranjan, M., & Dhaniyala, S. (2009). A novel electrical-mobility-based instrument for total number concentration measurements of ultrafine particles. Journal of Aerosol Science, 40(5), 439-450.

Redhead, H. M., Davis, S. S., & Illum, L. (2001). Drug delivery in poly(lactide-co-glycolide) nanoparticles surface modified with poloxamer 407 and poloxamine 908: in vitro characterisation and in vivo evaluation. Journal of Controlled Release, 70(3), 353-363. doi: http://dx.doi.org/10.1016/S0168-3659(00)00367-9

Reischl, G. P., Makela, J. M., Karch, R., & Necid, J. (1996). Bipolar charging of ultrafine particles in the size range below 10 nm. Journal of Aerosol Science, 27, 931–949. doi:10.1016/0021-8502(96)00026-2

Rogak, S. N., & Flagan, R. C. (1992). Bipolar diffusion charging of spheres and agglomerate aerosol particles. Journal of Aerosol Science, 23(7), 693–710. doi:10.1016/0021-8502(92)90037-V

Schmid, O., & Stoeger, T. (2016). Surface area is the biologically most effective dose metric for acute nanoparticle toxicity in the lung. Journal of Aerosol Science, 99, 133-143. doi: http://dx.doi.org/10.1016/j.jaerosci.2015.12.006

Serway, R., & Jewett, J. (2009). Physics for scientists and engineers with modern physics. Boston, MA: Cengage Learning.

Shin, W. G., Pui, D. Y. H., Fissan, H., Neumann, S., & Trampe, A. (2007). Calibration and numerical simulation of nanoparticle surface area monitor (TSI model 3550 NSAM). Journal of Nanoparticle Research, 9(1), 61-69. doi: 10.1007/s11051-006-9153-y

Shin, W. G., Wang, J., Mertler, M., Sachweh, B., Fissan, H., & Pui, D. Y. H. (2009a).

Structural properties of silver nanoparticle agglomerates based on transmission electron microscopy: relationship to particle mobility analysis. Journal of Nanoparticle Research, 11(1), 163–173. doi:10.1007/s11051-008-9468-y

Shin, W. G., Qi, C., Wang, J., Fissan, H., & Pui, D. Y. H. (2009b). The effect of dielectric constant of materials on unipolar diffusion charging of nanoparticles. Journal of Aerosol Science, 40, 463–468. doi:10.1016/j.jaerosci.2009.01.003

Shin, W. G., Wang, J., Mertler, M., Sachweh, B., Fissan, H., & Pui, D. Y. H. (2010). The effect of particle morphology on unipolar diffusion charging of nanoparticle agglomerates in the transition regime. Journal of Aerosol Science, 41(11), 975-986. doi: 10.1016/j.jaerosci.2010.07.004

Slinn, W. (1984). Precipitation scavenging. Atmospheric Science and Power Production, 466-532.

Sorensen, C. M. (2011). The mobility of fractal aggregates: a review. Aerosol Science and Technology, 45(7), 765-779. doi:10.1080/02786826.2011.560909

Thajudeen, T., Gopalakrishnan, R., & Hogan, C.J. (2012). The collision rate of nonspherical particles and aggregates for all diffusive knudsen numbers. Aerosol Science and Technology, 46(11), 1174-1186. doi:

10.1080/02786826.2012.701353

Tsai, C.J., Liu, C.N., Hung, S.-M., Chen, S.C., Uang, S.N., Cheng, Y.S., & Zhou, Y. (2012). Novel active personal nanoparticle sampler for the exposure assessment of nanoparticles in workplaces. Environmental science & technology, 46(8), 4546-4552.

TSI Model 3070A Electrical Aerosol Detector Data Sheet, Available online at http://www.tsi.com/uploadedFiles/Product_Information/Literature/Spec_Sheets/3070A.pdf

Vemury, S., & Pratsinis, S. E. (1995). Corona-assisted flame synthesis of ultrafine titania particles. Applied Physics Letters, 66(24), 3275-3277. doi:10.1063/1.113402

Wang, J., Shin, W. G., Mertler, M., Sachweh, B., Fissan, H., & Pui, D. Y. H. (2010). Measurement of nanoparticle agglomerates by combined measurement of electrical mobility and unipolar charging properties. Aerosol Science and Technology, 44(2), 97-108. doi:10.1080/02786820903401427

Wang, S. C., & Flagan, R. C. (1990). Scanning electrical mobility spectrometer. Aerosol Science and Technology, 13(2), 230-240.

Wei, J.M. (2007). Development of a method for measuring surface area concentration of ultrafine particles. Ph.D. thesis, University Duisburg-Essen, Germany.

Wei, J.M., Kruis, F.E., & Fissan, H. (2007). A method for measuring surface area concentration of ultrafine particles. European Aerosol Conference 2007. Abstract retrieved from abstracts in European Aerosol Conference database. (Accession No. T02A043)

Wentzel, M., Gorzawski, H., Naumann, K. H., Saathoff, H., & Weinbruch, S. (2003). Transmission electron microscopical and aerosol dynamical characterization of soot aerosols. Journal of Aerosol Science. 34:1347–1370. doi:10.1016/S0021-8502(03)00360-4

White, H. J. (1951). Particle charging in electrostatic precipitation. Transactions of American Institute of Electrical Engineers, 70, 1186–1191.

Witten, T. A., & Sander, L. M. (1981). Diffusion-limited aggregation, a kinetic critical phenomenon. Physical Review Letters, 47(19), 1400-1403. doi:10.1103/PhysRevLett.47.1400

Yook, S.-J., Fissan, H., Engelke, T., Asbach, C., van der Zwaag, T., Kim, J. H., . . .

Pui, D. Y. H. (2008). Classification of highly monodisperse nanoparticles of NIST-traceable sizes by TDMA and control of deposition spot size on a surface by electrophoresis. Journal of Aerosol Science, 39(6), 537-548. doi: http://dx.doi.org/10.1016/j.jaerosci.2008.03.001

Zhou, H. X., Szabo, A., Douglas, J. F., & Hubbard, J. B. (1994). A brownian dynamics algorithm for calculating the hydrodynamic friction and the electrostatic capacitance of an arbitrarily-shaped object. Journal of Chemical Physics, 100(5), 3821-3826. doi:10.1063/1.466371

Appendix

This Appendix contains copies of copyright permissions granted by the owners of the journals when the work is published.

Title: The capacitance and charge of agglomerated nanoparticles during sintering

Author: Leo N.Y. Cao,Jing Wang,Heinz Fissan,Sotiris E. Pratsinis,Max L. Eggersdorfer,David Y.H. Pui

Publication: Journal of Aerosol Science

Publisher: Elsevier

Date: May 2015